A VALIDATION AND VERIFICATION APPROACH FOR COMPUTATIONAL WIND ENGINEERING SIMULATIONS USING AN EXPERIMENTAL DESIGN TECHNIQUE

by
Réamonn Mac Réamoinn

A thesis submitted to Johns Hopkins University in conformity with the requirements for the degree of Master of Science in Engineering

Baltimore, Maryland

August, 2015

Abstract

The aerodynamic data obtained from Computational Wind Engineering (CWE), which is a subset of computational fluid dynamics (CFD), is not trusted as the results from different simulations of the same problem can vary widely. If CWE should be used in conjunction with or in place of wind tunnel testing to inform the design of special structures, such as tall buildings or long span bridges, it is necessary to improve the credibility of these simulations.

A robust approach to verification and validation (V & V) can help improve confidence of the CWE solutions. Common V & V approaches in other fields are not necessarily appropriate to CWE due to the complexity of the problems. This study proposes an alternative method for the evaluation of errors and uncertainties in CWE simulations based on the experimental design technique, which is modified from the factorial design approach.

Initially, the study examines high Reynolds number flow around a 2D square cylinder using the open source CFD package, OpenFOAM. It considers a range of values for different experimental design parameters as part of a modified fractional factorial design approach. The purpose of this study is to verify the optimal parameters for achieving a parameter-independent solution, where numerical errors are minimized. The final stage of the study seeks to validate a simulation high Reynolds number flow around a 3D square cylinder with a finite spanwise length, in which the optimal experimental parameters determined from the 2D simulations are utilized, through comparison with previous experimental results.

This study concludes that the results support the premise that an experimental design technique, such as the modified fractional factorial approach, can be used to provide a robust and reliable method for the verification and validation of CWE simulations.

287 words

Keywords: URANS, CFD, CWE, OpenFOAM, Experimental Design, Fractional Factorial Design, Verification and Validation.

Advisors:	Dr. DongHun Yeo, National Institute of Standards and Technology
	Dr. Rachel Sangree, The Johns Hopkins University
Reader:	Prof. James Guest, The Johns Hopkins University

Preface

The thesis is the culmination of work carried out as part of a two-year research masters at the Department of Civil Engineering, Johns Hopkins University, Baltimore, Maryland.

I would like to thank my advisors, Dr. DongHun Yeo of the National Institute of Standards and Technology (NIST) and Dr. Rachel Sangree of the Johns Hopkins University for all their indispensable advice and assistance.

In addition, I would like to recognize the efforts of Dr. Emil Simiu of NIST and Prof. Ben Schafer of the Johns Hopkins University in facilitating my research on this topic.

I would like to thank Prof. James Guest and Prof. Ben Schafer for allowing me access to their Linux cluster and enabling me to perform the simulations necessary to undertake my research.

I would like to acknowledge all the help and support I received from my friends and family while conducting this research. In particular, I would like to thank my wife, Suzanne, for her patience, kindness and understanding through it all.

Réamonn Mac Réamoinn

Réamonn Mac Réamoinn

14th August 2015

Baltimore, Maryland

Table of Contents

List of Tables

List of Figures

Chapter 1

Introduction

1.1 Background

The design of special structures, such as tall buildings and long span bridges, requires the use of aerodynamic data obtained from wind tunnel tests (Simiu, 2011). However, wind tunnel tests do not necessarily ensure that the model experiences wind conditions similar to those encountered by the full-scale structure. This disparity can be caused by a variety of reasons including Reynolds number similarity violation and difficulties in generating a fully developed turbulent flow boundary layer. Although the deficiencies can be mitigated to some degree, subjective interpretation based on experience is relied above to resolve the difference between the model and the prototype. However, in spite of all the shortcomings of wind tunnel testing, it is still a trusted approach to evaluate the performance of real-world structures due to wind loading based on interpretation and experience.

Computational wind engineering (CWE), which is a subset of computational fluid dynamics (CFD), does not suffer from the same shortcomings as wind tunnel testing. For instance, it accommodates complete similitude between the model and the prototype and therefore, does not suffer from Reynolds number violation. In addition, as the design of structures becomes more and more dependent on computers, CWE is better suited for the transfer of data and knowledge between models. CWE is not without its own shortcomings and it is even difficult to develop a representative fully developed turbulent boundary layer in CWE. Other challenges include replicating flows near and / or around a structure. This is particularly problematic when flow separation occurs. The consequence of this is that results of different simulations can range widely.

If CWE should be used in conjunction with or in place of wind tunnel testing to obtain aerodynamic data for the purposes of the design of special structures, it is necessary to improve credibility in the approach. According to Oberkampf and Trucano (2007), verification and validation (V & V) has a key role to play in increasing the confidence in codes. Therefore, it is essential to develop reliable methods for the V & V of CWE simulations.

Many previous studies have examined both 2D and 3D flows around bluff bodies using CFD. Some studies even considered bluff bodies with complex geometries. However, few of these studies adopted a reliable and robust approach to V & V of the CWE model.

1.2 Outline of Thesis

The objective of this thesis is to develop a reliable and robust method for the V & V of CWE simulations. The method is based on the premise of experimental design such that the ultimate solution provides a highly accurate solution with the minimal amount of computational effort.

Initially, this study examines different experimental parameters over a range of values using an experimental design approach, known as the fractional factorial design approach, for flow around a 2D square cylinder. The purpose of this is to identify the sensitivity of the CWE simulation to changes in experimental parameters. The intention is to verify the optimal parameters for achieving a parameter independent solution, where numerical errors are minimized. The square cylinder is chosen as a simple representation of a bridge deck or building cross-section.

Following the identification of the optimal experimental parameters in the verification stage, a further simulation is carried out to validate the CWE model of flow passing a 3D square cylinder against past experimental result. The third dimension is important for the comparison with the experimental results, as both vorticity and turbulence are 3D phenomena.

Chapter 2 gives an overview of the basic concepts of fluid dynamics including a discussion of bluff body aerodynamics

Chapter 3 provides a brief description of CWE and it explains how it is utilized to solve fluid dynamic problems.

Chapter 4 focuses on the V & V of CWE simulations. In particular, it explains the meaning of experimental design and how experimental design technique can be used in the V&V of CWE simulations.

The numerical set-up of the problem, which is considered in this study, is addressed in the Chapter 5.

The results of the CWE simulations and the subsequent analysis are presented in Chapter 6.

Chapter 7 consists of a discussion of results of the present study and a comparison with previous studies both experimental and numerical.

The final chapter, Chapter 8, the conclusions and recommendations of the study are presented.

Chapter 2

Theory

2.1 Basic Concepts of Fluid Flow

Fluids are continuous substances that offer no resistance to externally applied shear forces, such as liquids or gases. When subject to external forces fluids deform and therefore, fluids can change shape or even flow from point to another. Common forces that influence the behavior of fluids includes pressure differences, shear forces, gravity and surface tension.

Adopting a Eulerian description of flow, the velocity field can be defined in terms of position and time.

$$V = V(s, t)$$

A flow is considered *uniform* if the velocity remains constant in magnitude and direction at every point along a streamline for a given time instant (Crowe et al, 2013). However, if the velocity changes along a streamline in either magnitude or direction or both, the flow is *non-uniform*. Uniform and non-uniform flow can be represented using the following expressions, respectively:

$$\frac{\partial V}{\partial s} = 0 \qquad \frac{\partial V}{\partial s} \neq 0$$

A flow is considered *steady* if the velocity at a particular location remains constant in time (Crowe et al, 2013). If the velocity fluctuates, either periodically or randomly, at any point within the flow field, the flow is considered *unsteady*. Steady and non-steady flow can be represented using the expressions below:

$$\frac{\partial V}{\partial t} = 0 \qquad \frac{\partial V}{\partial t} \neq 0$$

2.2 Equations of Fluid Motion

Consider a volume of fluid in a steady uniform flow. The principle of the conservation of momentum (Newton's second law of motion) states that the rate of change of momentum equals the sum of the external forces, $\sum F = ma$. However, for steady uniform flow the fluid does not experience any acceleration and therefore, the sum of external forces must equal zero, $\sum F = 0$.

Figure 2.1: Forces acting on a volume of fluid in a steady uniform flow

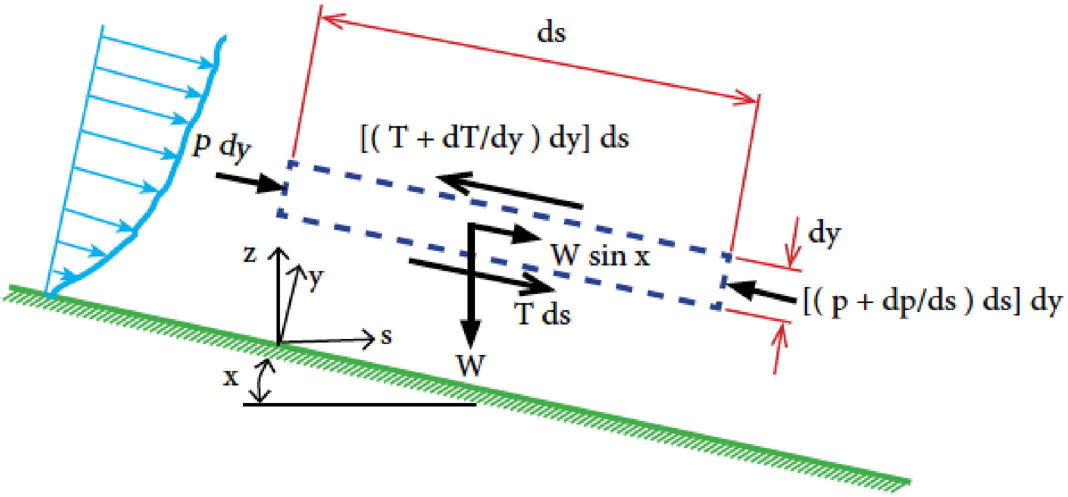

The forces acting on the fluid volume are due to pressure, shear stress and gravity. The pressure force is given by the expression:

$$p\Delta y - \left(p + \frac{dp}{ds}\Delta s\right)\Delta y = -\frac{dp}{ds}\Delta s\Delta y$$

The net force due to shear stress can be expressed as:

$$\left(\tau + \frac{d\tau}{dy}\Delta y\right)\Delta s - \tau\Delta s = \frac{d\tau}{dy}\Delta y\Delta s$$

The force acting on the fluid body due to gravity is given by the expression:

$$\rho g\Delta s\Delta y \sin\theta = -\rho g\Delta y\Delta s\frac{dz}{ds}$$

Therefore, the sum of the external forces leads to the following expression:

$$\sum F = \frac{d\tau}{dy}\Delta y\Delta s - \frac{dp}{ds}\Delta s\Delta y - \rho g\Delta y\Delta s\frac{dz}{ds} = 0$$

Steady uniform incompressible one-dimensional flow can be represented as:

$$\frac{d\tau}{dy} = \frac{d}{ds}(p + \rho gz)$$

Given that the Eulerian description of the acceleration of a parcel of fluid is dependent on position as well as time, the acceleration of a parcel of fluid can be written as follows:

$$a = \frac{dV(s,t)}{dt} = \frac{\partial V}{\partial s}\frac{ds}{dt} + \frac{\partial V}{\partial t} = V\frac{\partial V}{\partial s} + \frac{\partial V}{\partial t}$$

The first term in the final expression is called convective acceleration while the final term is known as the local acceleration.

For unsteady non-uniform incompressible (i.e. constant density) flow, the momentum equation can be written as:

$$\sum F = ma = \rho Va = \rho\left(V\frac{\partial V}{\partial s} + \frac{\partial V}{\partial t}\right)$$

The resistance of a fluid to deformation or motion is known as *viscosity*, μ, (Crowe et al, 2013) and it is the ratio of shear stress to the rate of shear strain. For instance, more effort is required to push a spoon through honey than water as the former has a higher viscosity than the latter. If within the fluid the shear stresses are linearly proportional to the local strain rate, it is considered a *Newtonian fluid*. The constitutive relationship for a Newtonian fluid is given by the following expression:

$$\tau_{ij} = \mu\left(\frac{\partial u_i}{\partial x_j} + \frac{\partial u_j}{\partial x_i}\right)$$

Therefore, the momentum equation for an unsteady non-uniform incompressible Newtonian flow in three dimensions can be expressed, using Einstein notation, as follows:

$$\rho g_i - \frac{\partial p}{\partial x_i} + \mu\left(\frac{\partial u_i}{\partial x_j} + \frac{\partial u_j}{\partial x_i}\right) = \rho\left(\frac{\partial u_i}{\partial t} + u_j\frac{\partial u_i}{\partial x_j}\right)$$

The law of conservation mass states that for any closed system the mass of the system must remain constant over time (Crowe et al, 2013), (Ferzinger & Peric, 2002). In continuum mechanics, this equation is known as the continuity equation and it can be written as follows:

$$\frac{\partial \rho}{\partial t} + \frac{\partial \rho u_i}{\partial x_i} = 0$$

The combination of the conservation of momentum equation and the continuity equation are commonly referred to as the Navier-Stokes equations. These equations are second-order, non-linear, coupled, partial differential equations that can be extremely difficult to solve. Therefore, numerical methods are relied upon to provide approximate solutions to these equations.

It can be instructive to consider the non-dimensional form of the Navier-Stokes equation. It can be non-dimensionalized using the following length scale, l_o, and velocity scale, u_o, which gives the following time scale relationship, l_o / u_o, and permits the pressure to be scaled against the dynamic pressure, ρu_o^2. This gives the following non-dimensional form of the equation.

$$\frac{g_i l_o}{u_o^2} - \frac{\partial P}{\partial X_i} + \frac{\mu}{\rho u_o l_o}\left(\frac{\partial^2 U_i}{\partial X_j^2}\right) = \left(\frac{\partial U_i}{\partial T} + U_j\frac{\partial U_i}{\partial X_j}\right)$$

The first term in this equation known as the Froude number (Fr), which is a measure of the relationship between inertial forces and gravitational forces (Crowe et al, 2012). The expression in advance of the diffusive term (third term) is known as the Reynolds number (Re). It measures the ratio of inertial to viscous forces (Simiu, 2006) and it can provide important information about the flow.

In *laminar* flows, the fluid particles follow a smooth trajectory (Crowe et al, 2013) and they are considered travel in different layers or lamina. Viscous forces are more prominent in laminar flows and therefore, they are associated with low Re values.

On the other hand, turbulent flows involve random and chaotic fluctuations in the fluid. Inertial forces are far more dominant then viscous forces and therefore, turbulence is found to occur at higher Re values. Turbulence causes interaction between fluid parcels with low and high momentum. The turbulence may already exist within the approaching flow (i.e. free-stream turbulence) or it might be generated through the interaction between the body and the fluid (i.e. signature turbulence).

Figure 2.2: Turbulent fluctuations

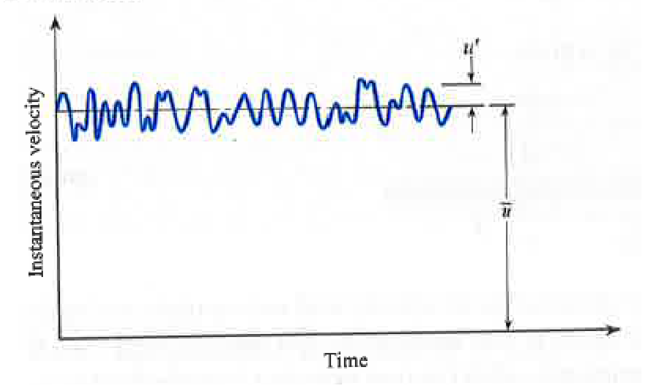

However, the definition of a low or high Re number is dependent on the chosen length scale and therefore, the exact value of a low or high Re number is problem dependent.

2.3 Boundary Layer Flow

A flow is known as *inviscid* if the viscosity effects are negligible and can be ignored. Typically, viscosity effects are only important in proximity to surfaces or boundaries (Crowe et al, 2013). When a flow encounters a flat plate or surface, it is assumed that the velocity of the flow is stationary relative to the surface due to the effects of friction, which is known as the *no slip condition*. The flow velocity increases with distance from the surface due to the interaction between the closer lower velocity and the outer higher velocity fluid particles.

The region where this transition in velocity occurs is known as the *boundary layer*. A laminar boundary layer is classified by smooth steady flow with a parabolic velocity distribution. Typically, boundary layers are laminar initially before thickening gradually downstream until a point when the thickness is such that the boundary layer becomes unstable. The laminar boundary layer contributes little to the drag force on a body, as it exists for only a relatively short distance before transitioning into a turbulent boundary layer. A turbulent boundary layer is associated with eddies and intense cross-stream mixing that brings higher velocity fluid particles closer to the surface. This leads to a much more uniform velocity distribution. In this study, the boundary layer is considered fully turbulent throughout. A turbulent boundary layer consists of three different zones: the viscous sublayer, the logarithmic region and velocity defect region.

Figure 2.3: Turbulent boundary layer velocity profile

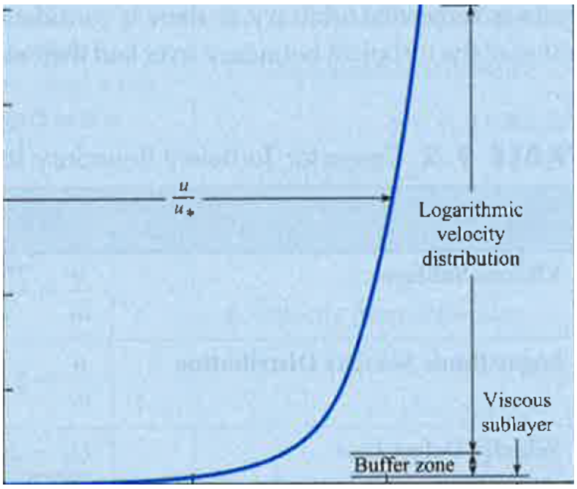

The flow regime is essentially laminar within the *viscous sublayer* as the proximity of the boundary surface acts to inhibit cross-stream mixing and dampen out turbulent fluctuations. Moreover, the shear stress across this thin layer remains constant. The relative distance from the boundary, y+, is given by the following expression:

$$y^{+} = \frac{yu_{*}}{\nu}$$

where y is the distance to the surface, ν is the kinematic viscosity and u_* is the friction velocity or shear velocity given by $u_{*} = \sqrt{\tau_{0}/\rho}$, where τ_0 is the shear stress at the surface. Is it estimated from experimental results that a y+ value of 5 defines the extent of the viscous sublayer. The relative velocity distribution within this layer is given by the expression:

$$\frac{u}{u_{*}} = \frac{u_{*}y}{\nu}$$

The *logarithmic region* is a turbulent layer situated outside the viscous sublayer. The cross-stream mixing that occurs within this layer facilitates interaction between the low speed fluid near the boundary and the higher speed fluid nearer the free-stream. Although the process consists of momentum transfer within the fluid, it affects the flow in a similar manner to applied shear stresses. These effective stresses arising from the turbulent mixing, which are determined from the fluctuating components in the flow, are termed *Reynolds stresses*. An expression for the velocity distribution assuming the following:

- velocity fluctuations are proportional size of the turbulent eddies or 'mixing length' as proposed by Prandtl;
- the 'mixing length' was proportional to the distance from the boundary;
- velocity fluctuations in the transverse direction will similar in magnitude to those in the principal flow direction.

Based on these assumptions, the relative velocity distribution in the logarithmic region is described using the following expression:

$$\frac{u}{u_*} = \frac{1}{\kappa} ln \frac{u_* y}{\nu} + 5.56$$

where κ is Karman's constant and is approximately 0.41 in the zone adjacent the viscous sublayer. This expression is valid for y+ values between 30 and 500. The combination of the profiles for the viscous sublayer and the logarithmic region using the above expressions to describe the velocity profile for y+ values from 0 to 500 is known as the *law of the wall*.

The *velocity defect region* is a zone at the outer extent of the boundary layer where the logarithmic velocity distribution no longer adequately reflects the actual velocity profile. Instead, the relative velocity is expressed as a function of the distance from the boundary, which known as the *velocity defect law*.

$$\frac{U_0 - u}{u_*} = f\left(\frac{y}{\delta}\right)$$

where U_0 is the free-stream velocity and δ is the thickness of the total thickness of the boundary layer.

2.4 Aerodynamics

When a body is immersed in a flow, the fluid in the vicinity of the body is retarded due to the effect of friction. The fluid encountering the front of the body stagnates at a point referred to as the *stagnation point*. The approaching flow decelerates to a relative flow velocity that is effectively zero at this point. A region of high pressure develops upstream of the body. The maximum pressure or stagnation pressure occurs at the stagnation point. Beyond the stagnation point, the flow must accelerate around the body in accordance with continuity. The shape of the body and the nature of the flow dictate the behavior of the flow around the body.

2.4.1 Streamlined Bodies

For a streamlined body, a boundary layer forms around the body between the high speed free-stream flow and the lower speed fluid near the body surfaces. The flow accelerates to maximum value downstream resulting in the formation of a low pressure on the side of the body. Beyond this point, however, the pressure increases. The initial favorable external pressure gradient present at the front of the streamlined body gives way to an adverse gradient further downstream.

Figure 2.4: Flow around streamlined body

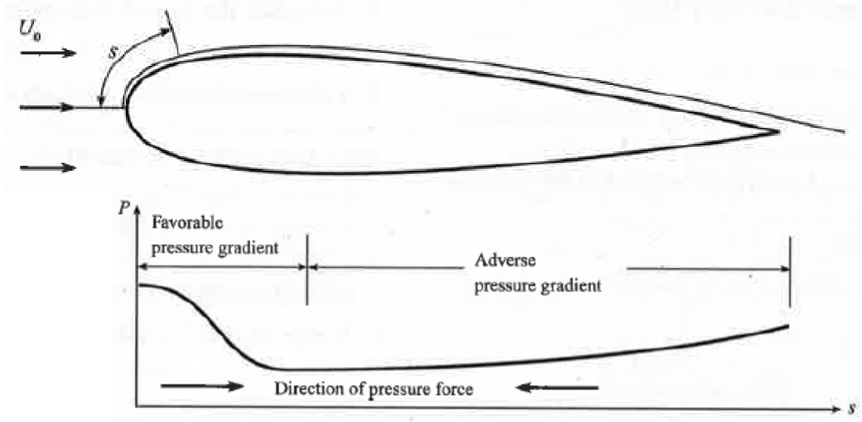

The external pressure gradients influence the behavior of the boundary layer. The favorable pressure gradient, which causes the fluid to accelerate, limits the boundary growth and ensures that the shear layer remains attached. Therefore, the onset of the turbulent boundary layer is delayed. On the other hand, the adverse gradient acts to decelerate the flow, and if the adverse gradient persists, this can eventually lead to reversal the flow direction near the body surface. This results to the formation of a circulation or an eddy within the flow. The point where the flow reversal occurs is known as the *separation point.* At this point, the boundary layer detaches from the surface becoming a free shear layer. It is not uncommon for a free shear layer to reattach, however, it does depend on the flow and the shape of body.

Reattachment is much more likely for longer a body that extends downstream of the separation point.

2.4.2 *Smooth Bluff Bodies*

Similar to streamlined bodies, the favorable pressure gradients that develop upstream of a smooth bluff body, such as a circular cylinder; ensure that a thin laminar boundary layer develops on the upstream side of the cylinder. However, the behavior of the fluid further downstream depends on viscous effects and therefore, is Reynolds Number (Re) dependent.

At extremely low flow velocities (i.e. $Re < 5$), the flow around the circular cylinder is laminar and there is little or no flow separation. The flow is symmetric about the center of the cylinder and therefore, there is no resultant lift force. A drag force acts on the cylinder but this is largely due to skin friction.

At low flow velocities (i.e. $5 < Re < 40$), the curvature of the body is too severe and the laminar boundary layer separates from the boundary surface. The point of separation is located midway between the front and back of the cylinder. A pair of symmetric vortices forms towards the rear of the body. Due to the symmetry in the flow, there is no resultant lift force acting on the body and the drag force is as a result of a combination of skin friction and form drag.

Figure 2.5: Flow around a smooth bluff body

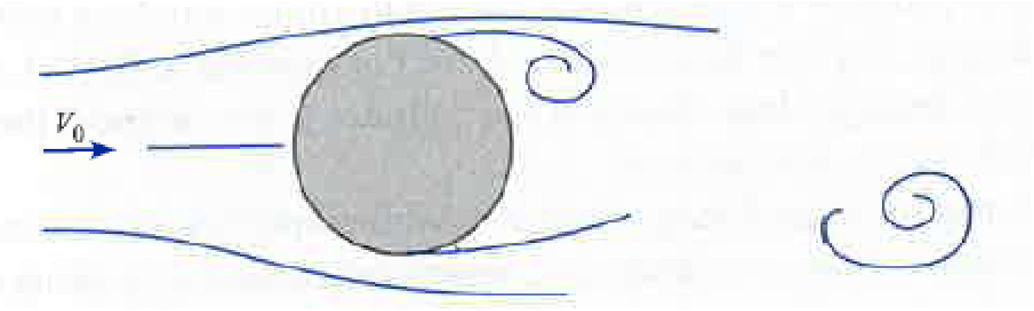

As the flow velocity increases further (i.e. $40 < Re < 1e5$), the shear layer remains laminar but the vortices behind the body become evermore unstable. This instability causes the vortices to develop on alternate sides of the cylinder. The formation of a vortex on one side causes the previous vortex on the opposite side to be shed into the wake. A large wake forms behind the rear of the cylinder generating a region of low pressure. The strength of the vortices shed from the body depends on the base pressure and the shedding frequency depends on the width of the wake. The Strouhal number, St, is a non-dimensional parameter related to the vortex shedding frequency. Due to the periodic shedding of vortices from the rear of the cylinder, there are fluctuations in the magnitude of the drag force, which is mostly due to form drag. In addition, the cylinder experiences a fluctuating lift force due to the shedding of vortices from opposite sides.

The cylinder experiences the ‘drag crisis’ with further increases in velocity (i.e. $1 \times 10^5 < Re < 5 \times 10^5$). The attached boundary layer is no longer laminar when it separates. The turbulent boundary layer entrains faster moving fluid into the slower moving fluid near the body surface. The boundary layer is better able to resist the influence of the adverse pressure gradient. As a result, the separation point is shifted further downstream and the wake narrows. The magnitude of the low pressure at the rear of the cylinder reduces and therefore, results in weaker vortices being shed. Therefore, there is a dramatic reduction in both fluctuating drag and lift forces. Further increases in velocity result in subsequent increases in drag and lift.

2.4.3 Angular Bluff Bodies

The pressure approaching an angular bluff body, such as a square cylinder, is retarded and therefore, the fluid applies a pressure to the windward face. This allows a favorable pressure gradient to develop upstream of a square body. Lyn and Rodi (2004) found that the velocity profile was affected by the presence of the square cylinder even at a distance of 2.5H upstream from the face of the cylinder, where H is the characteristic dimension of the cylinder.

Figure 2.6: Flow around an angular bluff body

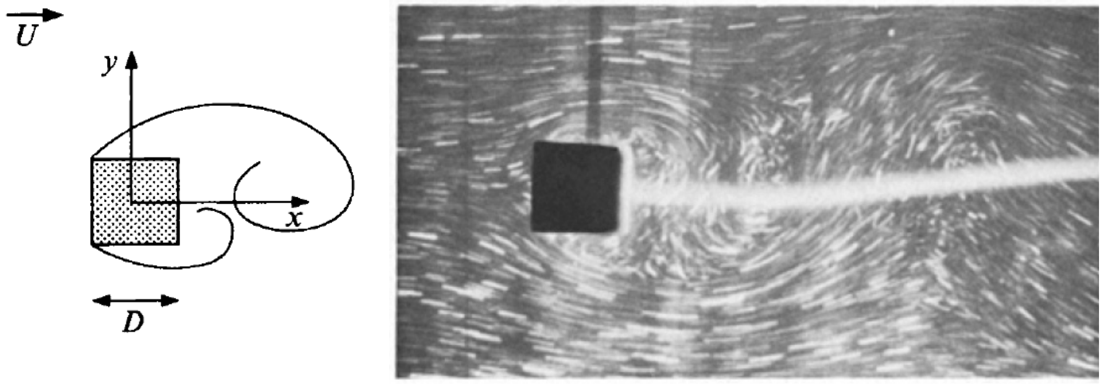

Unlike smooth bodies, the extreme change in geometry at the corners of the square forces the flow accelerated around the body to separate. Therefore, the separation point is fixed at the front corner of the body (Lyn and Rodi, 1994). The favorable pressure gradient upstream of the prism ensures that a thin jet-like shear layer forms around the bluff body. A recirculation zone forms in the separation zone between the shear layer and cylinder wall. The velocity of the flow within the recirculation zone is extremely small (Simiu, 2012). The velocity of the flow within the shear layer is larger than the flow further upstream creating a region of low pressure. The pressure in the recirculation zone is effectively the same as the pressure in the shear layer and the result is that the cylinder sides experience suction.

It is insightful to examine flow parameters in terms of phase-averages, which are based on the vortex shedding cycle, rather than in terms of time-averages alone. The shear layer undergoes its own cycle that includes accelerating and deceleration phases (Lyn and Rodi, 1994). According to Lyn and Rodi (1994), the shear layer is steady for much of the cycle; however, it does shift rapidly when vortices are shed. During the accelerating phase, the streamlines are situated near the cylinder face and the recirculation is located approximately coincident with the center of the cylinder.

During the deceleration phase, the streamlines shift further from the wall and the recirculation moves downstream. The location of the center of the recirculation zone fluctuates through the cycle. The greatest variation in flow velocity occurs in the shear layer and the largest Reynolds stresses occur between the acceleration and deceleration phases.

Due to the flow separation that occurs at the upstream corner of the cylinder, a large wake forms behind the rear of the cylinder generating a region of low pressure. Lyn et al (1995), estimated that the size of the recirculation zone was approximating 1.40H from rear face for high Re number (i.e. Re = 20,000) while Durao et al determined the stagnation point was situated further from the rear face (i.e. 1.83H) for a lower Re number flow (i.e. Re = 14,000).

Alternating vortices are shed from the rear of the cylinder. According to Bearman and Trueman (1972), vortex shedding is the result of the interaction between two shear layers. The shear layers interact and roll into vortices. The vortices draw fluid from the base region maintaining a low pressure. Vortex continues to grow fed by the circulation from the attached shear layer (Durao et al, 1988) until it is sufficiently strong to draw across the opposite shear layer across the near wake, which cuts of the flow to the vortex and the vortex is shed (Bearman and Trueman, 1972).

The strength of the vortices shed from the body depends on the base pressure. Bearman and Trueman (1972) found that the base pressure, C_{pb}, was approximately equal to 1.40. The higher base pressure causes vortices to form later (Lee, 1975) and the greater distance to the formation of the vortex, the weaker the vortex strength (Bearman and Trueman, 1972).

According to Bearman and Trueman (1972), the shedding frequencies are influenced by distance to vortex formation as well as the distance between the shear layers or the width of the wake. A narrow vortex street increases the vortex frequency (Lee, 1975). The Strouhal number, which is equivalent to the non-dimensional vortex shedding frequency, was found for a square cylinder to be in the range 0.125 and 0.134 by a range of experimental studies (Bearman and Trueman, 1972), (Bearman and Obasaju, 1982), (Durao et al, 1988) (Lyn and Rodi, 1994).

The spacing between vortices at a distance greater than 3H from the rear of the prism was 5.9H, Bearman and Trueman (1972), and the velocity of the vortices was 0.76U, where U is the freestream velocity.

Similar to the circular cylinder, the magnitude of the drag force fluctuates due to the periodic shedding of vortices from the rear of the cylinder. Bearman and Trueman (1972) found that the drag coefficient, C_d, for a square prism normal to the flow direction is approximately equal to 2.20. Furthermore, it was found that the variation in stagnation pressure is negligible when compared with the base pressure and therefore, the variation in drag coefficient due to variation in base pressure (Bearman and Obasaju, 1982).

Similarly, the cylinder experiences a fluctuating lift force due to the shedding of vortices from opposite sides. Bearman and Obasaju (1982) estimated the fluctuating lift coefficient at 1.20.

Durao et al (1988) examined the kinetic energy of the turbulent fluctuations and they found that at the location of maximum time-averaged velocity that the turbulent fluctuations account for approximately 40% of the total kinetic energy. In addition, they found that the kinetic energy rises near prism reaching a maximum near the stagnation point. In addition, the peaks in kinetic energy were found to be greater for periodic wakes (Durao et al, 1988). Furthermore, filtering the measurements can have an adverse effect on the results as it can inadvertently reduce kinetic energy peaks (Durao et al, 1988).

Finally, Bearman and Obasaju (1982) examined the flow in three dimensions and they found that the spanwise correlation reduces, as the flow velocity and Re increases.

The main aerodynamic parameters from previous experimental studies carried out examining high Re flow around a square cylinder are summarized in the table below.

Figure 2.1: Summary of previous experimental studies

Study	Bearman[1]	Bearman[2]	Durao[3]	Lee[4]	Lyn[5]	Lyn[6]
	(1975)	(1981)	(1988)	(1975)	(1994)	(1995)
Reynolds number, Re	20,000 – 70,000	5,800 – 32,000	14,000	176,000	21,400	21,400
Turbulence (%)	0.3 %	0.04 %	6 %	0 – 12.5 %	2 %	2 %
Blockage (%)	6 %	5.5 %	12.8%	3.6 %	7 %	7 %
Measurement method	PT & HW	PT	LDV	PT	LDV	LDV
Base Pressure, C_{pb}	1.4	1.6	-	0.8 -1.4	-	-
Drag Coefficient, C_d	2.2	-	-	1.5 - 2.2	-	-
Lift Coefficient, C_l	-	1.2	-	-	-	-
Strouhal Number, St	0.125	0.130	0.133	0.120 – 0.126	0.134	0.132

Superscript Notes:

1. Bearman and Trueman (1975): Time-averaged results from pressure tappings (PT) and flying-hot-wire anemometry (HW)
2. Bearman and Obasaju (1981): Time-averaged results from pressure tappings (PT)
3. Durao et al. (1988): Time-averaged results from Laser Doppler Velocimetery (LDV)
4. Lee (1975): Time-averaged results from pressure tappings (PT)
5. Lyn and Rodi (1994): Time-averaged and phase-averaged results from Laser Doppler Velocimetery (LDV)
6. Lyn et al. (1995): Time-averaged and phase-averaged results from Laser Doppler Velocimetery (LDV)

Chapter 3

Computational Fluid Dynamics

3.1 Introduction

Computational fluid dynamics (CFD) is a method for solving partial differential equations (PDE) in continuum mechanics using numerical techniques (Ferzinger and Peric, 2002). It involves breaking the problem down into a discrete number of elements that can be solved more easily. Combining the solutions from these smaller elements permits the generation of the complete solution.

Computational fluid dynamics covers a broad range of topics. This study is concerned with computational wind engineering (CWE), which is a subset of computational fluid dynamics, and it is concerned with the interaction between wind and real-life structures such a buildings and bridges.

Traditionally, the interaction between wind and structures would have been carried out through experimentation using a wind tunnel. Typically, non-dimensional parameters (e.g. Reynolds Number) are used to relate the wind tunnel experiments to the real-structure or prototype. However, due to the limitations of experimentation, it is rarely possible to ensure that these non-dimensional parameters are equivalent, particularly when there are multiple parameters being considered (Ferzinger and Peric, 2002). Unlike wind tunnel testing, CWE can match the non-dimensional parameters between the model and the prototype exactly. In addition, the instrumentation used in the wind tunnel can disturb the flow, which can influence the result in due course (Ferzinger and Peric, 2002). An advantage of CWE is that it calculates the flow fields across the entire domain in arriving at a solution and, therefore, it is possible to investigate the flow at any location without influencing the result. It should be noted that results of different CWE simulations tackling the same problem can vary (Yeo, 2013?) and often wind tunnel experiments are used to V & V CWE solutions.

It is necessary to define key components of the problem before determining a numerical solution. These key components include the following:

- mathematical model;
- discretization method;
- solution form;
- numerical grid;
- turbulence;
- convergence criteria.

3.2 Mathematical Model

It is possible to develop the equations of motion of an incompressible fluid from the principles of conservation.

3.2.1 Conservation Principles

The measurable characteristics of a system are known as properties. Extensive properties, such as mass or momentum, depend on the amount of matter in the system while intensive properties, such density (ρ) or velocity (υ), are independent of this (Crowe et al, 2013). The conservation laws were developed for a given quantity of matter or *control mass* (CM), and therefore, these laws were derived in relation to extensive properties. It is difficult to examine a parcel of matter in fluid flows and therefore, it is more convenient to consider the flow in terms of a defined spatial region or *control volume* (CV). As a result, it is necessary to define the system in terms of intensive properties rather than extensive properties.

3.2.2 Reynolds Transport Theorem

The Reynolds Transport Theorem is an equation that relates the extensive properties of a closed system such as a control mass with the intensive properties associated with a control volume (Crowe et al, 2013), (Ferzinger & Peric, 2002). It indicates that the rate of change of an extensive property in a closed system is equal to the rate of change of the equivalent intensive property within the control volume and its flux through the surfaces of the control surfaces.

$$\frac{d}{dt}\int_{\Omega_{CM}} \rho\phi \, d\Omega = \frac{d}{dt}\int_{\Omega_{CV}} \rho\phi \, d\Omega + \int_{S_{CV}} \rho\phi(\boldsymbol{v} - \boldsymbol{v}_b)\cdot \boldsymbol{n} \, dS$$

where υ_b is the velocity at which the control volume is moving, φ is the property under consideration, Ω is the control mass or volume, as appropriate, and S represents the control surfaces.

The term of the left side of this expression relates to the rate of change of the property with the control mass. The rate of change of the property within the control volume and its flux through the control surfaces are expressed by the first and second terms on the right hand side, respectively.

3.2.3 Mass Conservation

The principle of mass conservation or law of conservation mass state that for any closed system the mass of the system must remain constant over time (Crowe et al, 2013), (Ferzinger & Peric, 2002). The application of this law of conservation mass to a control volume is known as the continuity equation and it can be derived directly from the Reynolds Transport Theorem by setting the conserved intensive property, $\varphi = 1$. Therefore, assuming that the control volume is fixed, the conservation of mass can be described with the following expression:

$$\frac{\partial}{\partial t}\int_{\Omega} \rho \, d\Omega + \int_{S} \rho \boldsymbol{v} \cdot \boldsymbol{n} \, dS = 0$$

The accumulation term is the first term in the above equation and it describes how the quantity of mass changes within the control volume with respect to time. The convective term is the second term in the above expression and it describes the mass flow rate through the control surfaces.

3.2.4 Momentum conservation

The law of momentum conservation is given by Newton's 2nd Law of Motion, which states that the time rate of change of momentum in a closed system is equal to the sum of external forces applied to that system (Crowe et al, 2013), (Ferzinger & Peric, 2002). Once more, this law can be applied to a control volume through the Reynolds Transport Theorem with the exception on this occasion the conserved intensive property, φ, is assigned as υ, which is the velocity or the momentum per unit mass. This gives the following expression:

$$\frac{\partial}{\partial t}\int_{\Omega} \rho \boldsymbol{v} \, d\Omega + \int_{S} \rho \boldsymbol{v}\boldsymbol{v} \cdot \boldsymbol{n} \, dS = \sum f$$

Similar to the conservation of mass, the first term relates to the rate of momentum change within the control volume while the second term describes the exchange of momentum through the control surfaces. In order to express the right hand side of this expression in terms of intensive properties, it is necessary to consider the various forces that act on the fluid.

Forces arising from pressures or shear stresses with the flow or at boundaries can be treated as surface forces (Ferzinger & Peric, 2002). The system of equation is closed if these fluxes can be written in terms of properties, namely density and velocity, governed by the conservation equations. For incompressible Newtonian fluids, the molecular rate of transfer of momentum is given by:

$$\mathrm{T} = -p\mathrm{I} + \mu[grad\,\boldsymbol{v} + (grad\,\boldsymbol{v})^{\mathrm{T}}]$$

where I is the unit tensor and μ is dynamic viscosity.

Body forces, such as gravity or centrifugal forces, do not act with the control surfaces but instead, act on the control volume itself. The body forces can be written in the following form where the variable, b, represents the force per unit mass (Ferzinger & Peric, 2002).

$$\int_{\Omega} \rho\boldsymbol{b}\,d\Omega$$

Therefore, combining all these together gives the following expression for the conservation of momentum:

$$\frac{\partial}{\partial t}\int_{\Omega} \rho\boldsymbol{v}\,d\Omega + \int_{S} \rho\boldsymbol{v}\boldsymbol{v}\cdot\boldsymbol{n}\,dS = \int_{S} \mathrm{T}\cdot\boldsymbol{n}\,dS + \int_{\Omega} \rho\boldsymbol{b}\,d\Omega$$

3.2.5 Navier-Stokes Equations

The conservation of momentum equation and the continuity equation are commonly referred to as the Navier-Stokes equations. They represent Newton's Second Law of Motion as applied to the laminar viscous flow of a Newtonian Fluid.

$$\frac{\partial}{\partial t}\int_{\Omega} \rho\boldsymbol{v}\,d\Omega + \int_{S} \rho\boldsymbol{v}\boldsymbol{v}\cdot\boldsymbol{n}\,dS = \int_{S} \mathrm{T}\cdot\boldsymbol{n}\,dS + \int_{\Omega} \rho\boldsymbol{b}\,d\Omega$$

$$\frac{\partial}{\partial t}\int_{\Omega} \rho\,d\Omega + \int_{S} \rho\boldsymbol{v}\cdot\boldsymbol{n}\,dS = 0$$

Even though the above equations make no allowance for turbulence, these equations are second-order, non-linear, coupled, partial differential equations that can be extremely difficult to solve. Therefore, numerical methods are relied upon to provide approximate solutions to these equations.

3.3 Discretization

The mathematical model defines the problem. However, to solve the problem it is necessary to evaluate the system of equations in discrete sub-divisions of the domain in both space and time (Ferzinger and Peric, 2002).

The *finite difference method* (FDM) solves the differential form of the governing PDE using on Taylor series expansion. This method is not well suited to complicated geometries in multiple dimensions.

The *finite element method* (FEM) considers the integral form of the governing PDE and it can accommodate complex geometries. A basis function is specified to represent the variable variation across the element and a piecewise solution is derived through minimizing an appropriate error function.

The *finite volume method* (FVM) utilizes the form of governing PDE and it can also accommodate complex geometries. The computational domain divided into a finite number of contiguous cells. The method seeks to conserve mass; momentum and energy in each cell and therefore, the laws of conservation are maintained across the entire domain. This method does require all three methods of approximation: interpolation (center and faces), integration and differentiation, which makes it challenging to develop methods that are higher than second order accuracy.

3.4 Solution Form

3.4.1 Algorithms

It can be difficult to derive a solution to the Navier-Stokes equations, as the pressure and velocity fields are coupled (Ferzinger & Peric, 2002). The momentum equation dictates the velocity field. However, it is not possible to solve for the pressure using the continuity equation, as it contains no pressure term. Moreover, there is no dominant term in the continuity equation for incompressible flows and therefore, as Ferzinger and Peric (2002) suggest it acts more as “a kinematic constraint rather than a dynamic equation”. The solution is to re-write the continuity in terms of pressure through taking the divergence of the momentum equation and substituting it into the continuity equation. This equation is referred to as the *pressure equation* and it ensures that continuity is satisfied. Due to the coupling between the pressure and velocity fields, it is necessary to solve the Navier-Stokes equation sequentially. Solvers that adopt this approach are referred to as *implicit pressure-corrector methods*. There are a variety of algorithms available for solving incompressible flow problems, however, this study to focuses on three: the SIMPLE, PISO and PIMPLE algorithms.

3.4.1.1 SIMPLE Algorithm

The semi-implicit method for pressure-linked equations (SIMPLE) algorithm is used for solving steady state problems (OpenFOAM SIMPLE, 2014) and it contains no time advancing mechanism. This algorithm arrives at a solution sequentially and therefore, it assumes that only one variable is unknown.

This method evaluates the velocity field first using the momentum equation. It uses this intermediate velocity field to calculate the pressure. It does this using under-relaxation. The under-relaxation method limits the amount the flux can change to preserve stability (Ferzinger and Peric, 2002). The selection of the appropriate factor is largely empirical and problem dependent. Once the pressure has been estimated, the intermediate velocity field re-calculated. The SIMPLE algorithm makes only a single correction before advancing to the next iteration.

It is possible to make additional corrections for orthogonal meshes with this algorithm. On highly non-orthogonal meshes this can require as much as 20 additional iterations, however, no additional iterations are necessary if the mesh is orthogonal.

The greatest advantage of the SIMPLE algorithm is that it is fast at converging to a steady state.

3.4.1.2 PISO Algorithm

The pressure-implicit split-operator (PISO) algorithm is used for transient problems (OpenFOAM PISO, 2013). Similar to the SIMPLE algorithm, it arrives at a solution sequentially and therefore, it assumes that only one variable is unknown. However, unlike the SIMPLE algorithm, no under-relaxation is applied in this method. Instead, the PISO algorithm typically requires the momentum corrector step to be carried out more than once, although more than 4 iterations are necessary, and the pressure field is updated on each occasion. The more iterations carried out, the more stable the solution becomes and therefore, the better likely solution.

Similar to the SIMPLE algorithm, it is possible to make additional corrections for non-orthogonal meshes using this algorithm.

The PISO algorithm has a strict requirement for stability. It requires that the maximum Courant-Freidrichs-Lewy (CFL) number is less than 1 (i.e. CFL < 1). In other words, a parcel of fluid may not travel further than the smallest mesh dimension in a single time-step. This requirement results in extremely small time steps for problems containing high Reynolds number flows or complex geometries or both.

3.4.1.3 PIMPLE Algorithm

The merged PISO-SIMPLE (PIMPLE) algorithm combines the transient PISO solver with the fast converging steady state SIMPLE solver. It aims to take advantage of the properties of both PISO and SIMPLE algorithms (OpenFOAM PIMPLE, 2014). The combination allows for a transient PISO solver to take account of under-relaxation of the SIMPLE solver. Similar to the other algorithms discussed, it arrives at a solution sequentially. Moreover, it calculates an intermediate velocity field initially using momentum equation, which is used to update the pressure. This pressure field is used to re-evaluate the velocity field, which is used to estimate the pressure once more. However, the pressure is calculated using under-relaxation, which facilitate smooth convergence. This significantly increases the stability of the solver at larger time-steps. The speed of the SIMPLE algorithm at converging ensures that although additional iterations are necessary, the overall speed of the transient solver is increased significantly.

It is possible to evaluate the turbulent effects using the PIMPLE algorithm, however, it is typically carried out during the final iteration. The author's experience indicates considering turbulent effects every iteration had little benefit. The increased computational effort only had a very minor influence on the final result.

3.4.2 Solution Methods

3.4.2.1 Finite Approximations

The algebraic from of the mathematical model is obtained through approximating the surface and volume integrals using quadrature formulae (Ferzinger and Peric, 2002). Common approximations are made using the mid-point rule, the trapezoid rule or Simpson's rule. The accuracy is dependent on the approximations used.

In addition, the value of variables may be required at other points other than at the computational nodes. For instance, in the case of FVM, the variables are stored at the center of the cells but their values on the faces are required for certain calculations. Therefore, it is necessary to interpolate these values. Common interpolation schemes include upwind differencing schemes, Gauss linear schemes and liner upwind differencing schemes.

The *upwind differencing* scheme is a first order accurate interpolation scheme that utilizes an additional computational node upwind of the primary node based on the direction of the flow. This is a numerically diffusive scheme and therefore, it prohibits oscillatory solutions.

The *Gauss linear* scheme, or also called a *central difference scheme*, is a second order accurate interpolation scheme that considers computational nodes either side of the location of interest. It is the simplest and most widely used second order scheme. The *linear upwind scheme* is another second order interpolation scheme.

3.4.2.2 Temporal Solution Methods

It is necessary to consider changes in time for unsteady flows (Ferzinger and Peric, 2002). The time domain is discretized in terms of time-steps. However, time can only advance and therefore, the present conditions can only influence the flow into the future. There two primary categories of time-marching methods: explicit and implicit methods.

In *explicit methods*, such as the explicit Euler method, the value at the node under consideration for the next time-step is evaluated using the fluxes and sources from the previous time-step (Ferzinger and Peric, 2002). Therefore, there is only one unknown, the future value at the node

The method is unconditionally unstable, if the flow is exclusively controlled by convection and there is no diffusion. On the other hand, if there is no convection, the method is conditionally stable. For flows will negligible diffusion, stability is assured if the following conditions are satisfied.

$$\frac{\mathrm{u}\,\Delta t}{\Delta x} < 1 \qquad \frac{\rho u\,\Delta x}{\Gamma} < 2$$

where u is velocity, t is time, x is size of the mesh, ρ is the density of the fluid and Γ is the diffusion parameter (i.e. dynamic viscosity). The first condition is that the maximum Courant-Freidrichs-Lewy (CFL) number should not exceed 1. In other words, a parcel of fluid may not travel further than the smallest mesh dimension in a single time-step. The second condition is known as the Peclet number and it is a sufficient condition for boundedness of convective fluxes when central differencing methods are used. For problems dominated by convection, the second condition can be avoided if an upwind differencing method is used for the approximation.

In *implicit methods*, such as the implicit Euler method, the value of the node at the next time-step is evaluated using fluxes and sources from a future unknown time-step (Ferzinger and Peric, 2002). This method requires a large number of simultaneous equations to be solved at the same time and as a result, this method requires much more storage than explicit methods. The benefit of this approach is that it is results more stable solutions and therefore, it allows for much large time-steps, provided the Peclet number is not too large on coarse grids.

The *Crank-Nicolson method* is a blend between the explicit and implicit Euler methods. In other terms, it is the trapezoid rule applied to time. A benefit of this method is that it is second order accurate if it is blended evenly between the explicit and implicit Euler methods and the appropriate approximations are used. Moreover, it is energy conservative given that the scalar product of velocity and momentum equals the average change in kinetic energy between the time-steps. Furthermore it is unconditionally stable, although it can give oscillatory solutions at large time-steps. Stability is guaranteed if the following condition is satisfied:

$$\Delta t < \frac{\rho\,(\Delta x)^2}{\Gamma}$$

which is twice the time-step permitted by the explicit Euler method.

3.4.2.3 Spatial Solution Methods

The spatial discretization of the computational domain leads to a system of finite equations that must be solved at each time step. Due to the non-linear nature of the Navier-Stokes equations, these equations must be solved using iterative methods where the solution is initially guessed before it is systematically improved through iteration. An effective method should be computationally cheap and converge rapidly. The Gauss-Seidel method, which is iterative method that solves a lower triangular matrix, is one such method.

3.5 Numerical Grid

The grid consists of the division of the computational domain into smaller discrete subdomains. It is each of these subdomains that the variables are calculated. As stated by Dahl (2014), "the grid has a significant impact on the rate of convergence, the accuracy of the solution and the CPU-time of the simulation. Therefore, a poor grid can require a significant amount of computational effort and yet, it can result in an inaccurate solution. There are variety feasible grid arrangements.

3.5.1 Grid Arrangements

Structured grids are the easiest grids to solve and implement (Ferzinger and Peric, 2002). It is consists of regular members that encompass the entire domain but do not overlap. According to Ferzinger and Peric (2002), this mesh has the disadvantage that a concentration of points for the purposes of accuracy at one location requires an unnecessarily fine mesh at other locations in the computational domain.

Block-structured grids are similar to structured grids; however, different degrees of subdivision may be applied to various members (Ferzinger and Peric, 2002). Therefore, the computational domain may contain both coarse and fine elements.

Unstructured grids contain elements of any shape or size, although they typically consist of triangles or quadrilaterals in two dimensions and tetrahedral and hexahedra in three dimensions (Ferzinger and Peric, 2002). However, there is no limit on the number of interfaces with other elements. They may even overlap with each other. This is a highly flexible arrangement and it is particularly useful when modeling complex geometries. However, it may not be possible to implement some of the numerical techniques on unstructured grids.

3.5.2 Variable Arrangements on a Grid

Colocated grids, which may be structured, block-structured or unstructured grids, store all variables at the same set of grid points. For instance, all the variables are stored at the center of the cell in FVM. They are beneficial since they simplify the programming through minimizing number of coefficients to be calculated and stored (Ferzinger and Peric, 2002). In addition, they are suitable for multi-grids as it is easy to transfer information from one grid to the other (Ferzinger and Peric, 2002). However, it does complicate the numerical solver due to the coupling that exists between pressure and velocity (Ferzinger and Peric, 2002). It requires the values of the variables on the faces to be interpolated form the cell centers. This results in an inconsistent approach to the treatment of the pressure gradient in the momentum and continuity equations. This can lead to a potential instability in the solution, as it is not assured that energy in the system is conserved. Adopting the Crank-Nicolson method for the time integration can help overcome this problem, as the scalar product of the momentum and velocity flux using this method equals the average change in kinetic energy between the two relevant time-steps (Ferzinger and Peric, 2002).

The variables are not stored at the same location on *staggered grids*. It is possible with this approach if the grid is arranged correctly (i.e. pressure variables at cell centers and velocity variables on the cell faces) to avoid interpolating variables and therefore, allowing for straightforward evaluation of fluxes. It can facilitate a strong coupling between pressure and velocity fields, which can help to avoid convergence errors.

3.6 Turbulence

Turbulence is the random motion of a fluid (Ferzinger and Peric, 2002). The chaotic motions cause intense mixing to occur in all three dimensions over a broad range of length and time scales and thus, it brings fluids of differing momentum into contact with each other. Turbulence may or may not contain coherent structures, such as vortices, but is always characterized by large amounts of vorticity. Vorticity is a common way to describe rotation in the flow and it is equal to twice the rate-of-rotation vector. Alternatively, vortices can be described using the Q-criterion, which represents the local balance between shear strain rate and vorticity magnitude. This characterization defines areas where the vorticity magnitude is greater than the magnitude of rate-of-strain as vortices. The characteristics of turbulence make it very difficult to simulate numerically. The following section discusses a range of alternatives for incorporating turbulence into CFD simulations.

3.6.1 Turbulent Simulations

3.6.1.1 Direct Numerical Simulation

Direct Numerical Simulation (DNS) solves Navier-Stokes equation for fluid motion directly (Ferzinger and Peric, 2002). The aim is to calculate the mean flow and the turbulent fluctuations together (Xu, 2013). This demands evaluating turbulence with extremely small length scales in order to capture energy dissipation taking place, and this requires that the numerical grids are exceptionally fine. Furthermore, it is also necessary to consider the highest frequency flow fluctuations and therefore, incredibly small time-steps need to be considered. The benefit of this approach is that it provides precise details of turbulence and instantaneous results; however, it does require an extremely large computational effort.

3.6.1.2 Large Eddy Simulation

Large Eddy Simulation (LES) involves solving the larger more energetic eddies directly while using a turbulence model for the smaller eddies (Ferzinger and Peric, 2002) (Xu, 2013). According to Ferzinger and Peric (2002), "large eddy simulations are three dimensional, time dependent and expensive but less costly than DNS of the same flow". Therefore, it is suggested that DNS is more preferable once it is not too onerous to apply because of it accuracy. However, LES is justified for problems with high Reynolds Number flow or complex geometries or both.

3.6.1.3 Reynolds Averaged Navier-Stokes

The *Reynolds Averaged Navier-Stokes* (RANS) equations use a time-averaged representation of the Navier-Stokes equations and therefore, the unsteadiness in the flow is averaged out (Ferzinger and Peric, 2002). The *Unsteady Reynolds Averaged Navier-Stokes* (URANS) uses ensemble-averages that are not constant in time for the duration of the simulation but are constant for only a short time period (Dahl). The averaging of the equations leads to additional unknown terms in the Navier-Stokes equations due to the presence of turbulence in the flow (Ferzinger and Peric, 2002). The system of equations is not closed and therefore, it is necessary to model turbulent effects. These turbulence models should be considered as engineering approximations rather than scientific representations. Previous studies of URANS flow past a square cylinder have indicated that turbulence models should be used when considering Reynolds Number flows exceeding 300, (Franke et al, 1990). There is a significant reduction in computational cost using RANS or URANS instead of LES or DNS (Dahl, 2014). According to Ferzinger and Peric (2002), using DNS or LES simulations to evaluate problems where only a few quantitative properties of turbulent flow (e.g. average forces) would be excessive.

3.6.1.4 Detached Eddy Simulation

Detached Eddy Simulation (DES) is a compromise method between the RANS and LES approaches. Near boundaries where the turbulence length scale is less than the grid size, the turbulence is modeled using the RANS approach. In regions where the turbulence length scale exceeds the grid size, the LES approach is adopted. The grid generation is more complicated with DES, as it needs to allow for the switching between RANS and LES solutions for turbulence.

3.6.2 Turbulence Models

Turbulence acts to mix fluids of low and high momentum together (Wilcox, 1998). The effect is to retard the higher speed flow while increasing the momentum of the lower speed flow. Therefore, turbulence has a similar effect to viscosity except it is a property of the flow rather than the fluid. In the simplest model, the turbulence viscosity or the kinematic eddy viscosity, as it is also known, can be described using two parameters: a velocity scale and a length scale (Ferzinger and Peric, 2002). A variety of turbulence models have been developed including two equation models. In two-equation turbulence models the kinetic energy of the velocity fluctuation, k, defines the velocity scale and the size of the energy carrying turbulent eddies characterizes the length scale, and therefore, these models are considered complete.

Although the models are complete, it does necessarily mean they are accurate. As indicated by Ferzinger and Peric (2002) “there is no fundamental reason that [turbulent viscosity] should depend only on turbulence parameters”. Common two-equation turbulence models include the k-epsilon and the k-omega models.

3.6.2.1 k-epsilon Turbulence Model

The *k-epsilon model*, which was initiated by Prandtl, adopts a closure approximation for each one of the unknown turbulence correlations in the Navier-Stokes equation (Wilcox, 1998). This model attempts to accurately account for the rate of energy dissipation, ε. However, the time and length scales are related to the larger energy carrying eddies rather than the smaller dissipative eddies and, as such, the closure approximations are more closely related to energy transport rather than energy dissipation. Therefore, their derivation based on physical reasoning and dimensional analysis rather than on the underlying physics as intended. The accuracy of this model is not assured. In fact, the k-epsilon model does not respond to flows with adverse gradients present. This leads to an erratic prediction free shear flows and therefore, inaccurate prediction separated flows. In addition, the k-epsilon model is problematic near boundaries and can require correction. It may be necessary to calibrate such a model. The model is k-epsilon model is described by the following equations (Wilcox, 1998):

Kinematic Eddy Viscosity

$$\nu_T = {C_\mu k^2}/{\epsilon}$$

Turbulence Kinetic Energy

$$\frac{\partial k}{\partial t} + U_j \frac{\partial k}{\partial x_j} = \tau_{ij} \frac{\partial U_i}{\partial x_j} - \epsilon + \frac{\partial}{\partial x_j}\left[(\nu + \sigma^* \nu_T)\frac{\partial k}{\partial x_j}\right]$$

Dissipation Rate

$$\frac{\partial \epsilon}{\partial t} + U_j \frac{\partial \epsilon}{\partial x_j} = C_{\epsilon 1} \frac{\epsilon}{k} \tau_{ij} \frac{\partial U_i}{\partial x_j} - C_{\epsilon 2} \frac{\epsilon^2}{k} + \frac{\partial}{\partial x_j} \left[(\nu + \nu_T / \sigma_\epsilon) \frac{\partial \epsilon}{\partial x_j} \right]$$

Closure Coefficients and Auxiliary Relations

$$C_{\epsilon 1} = 1.44 \quad C_{\epsilon 2} = 1.92 \quad C_\mu = 0.09 \quad \sigma_k = 1.0 \quad \sigma_\epsilon = 1.3$$

$$\omega = \epsilon / (C_\mu k) \quad \ell = C_\mu k^{3/2} / \epsilon$$

3.6.2.1 k-omega Turbulence Model

The *k-omega* model, which was originally proposed by Kolmogorov and independently developed by Saffman, is analytically simpler than the k-epsilon model (Wilcox, 1998). Unlike the k-epsilon model, it does not approximate each turbulence correlation. Instead, it approximates the physical processes associated with turbulence such turbulence production, dissipation, molecular diffusion and turbulent transport. This model relates the rate of dissipation to the energy transport from the larger eddies to the smaller eddies through the dissipation per unit kinetic energy of turbulence, ω. The model is k-omega model takes the following form (Wilcox, 1998):

Kinematic Eddy Viscosity

$$\nu_T = {}^{k}\!/_{w}$$

Turbulence Kinetic Energy

$$\frac{\partial k}{\partial t} + U_j \frac{\partial k}{\partial x_j} = \tau_{ij} \frac{\partial U_i}{\partial x_j} - \beta^* k \omega + \frac{\partial}{\partial x_j} \left[(\nu + \sigma^* \nu_T) \frac{\partial k}{\partial x_j} \right]$$

Specific Dissipation Rate

$$\frac{\partial \omega}{\partial t} + U_j \frac{\partial \omega}{\partial x_j} = \alpha \frac{\omega}{k} \tau_{ij} \frac{\partial U_i}{\partial x_j} - \beta \omega^2 + \frac{\partial}{\partial x_j} \left[(\nu + \sigma \nu_T) \frac{\partial \omega}{\partial x_j} \right]$$

Closure Coefficients and Auxiliary Relations

$$\alpha = \frac{13}{25} \quad \beta = \beta_o f_\beta \quad \beta^* = \beta_o^* f_{\beta^*} \quad \sigma = \frac{1}{2} \quad \sigma^* = \frac{1}{2}$$

$$\beta_o = \frac{9}{125} \quad f_\beta = \frac{1+70\chi_\omega}{1+80\chi_\omega} \quad \chi_\omega \equiv \left|\frac{\Omega_{ij}\Omega_{jk}S_{ki}}{(\beta_o^*\omega)^3}\right|$$

$$\beta_o^* = \frac{9}{10} \quad f_{\beta^*} = \begin{cases} 1 & \chi_k < 0 \\ \dfrac{1+680\chi_k^2}{1+400\chi_k^2} & \chi_k > 0 \end{cases} \quad \chi_\omega \equiv \frac{1}{\omega^3}\frac{\partial k}{\partial x_j}\frac{\partial \omega}{\partial x_j}$$

$$\epsilon = \beta^* k\omega \quad \ell = {k^{1/2}}/{\omega}$$

The k-omega model has the following benefits in comparison with the k-epsilon model:

1. more accurate for two dimensional boundary layers for both favorable and adverse gradients;
2. more accurate predicting the spreading rates of free shear flows;
3. better at reproducing the turbulent kinetic energy close to solid boundaries;
4. does not require any special corrections to take the viscous sublayer into account.

3.6.3 Wall Functions

As states by Ferzinger and Peric (2002), “at high Reynolds number, the viscous sublayer of a boundary layer is so thin that it is difficult to use a enough grid points to resolve it”. The resolution of this problem is to develop a constitutive relationship between the velocity at the first grid point and the shear stress at the surface based on the law of the wall (Wilcox, 1998) (Ferzinger and Peric, 2002). It should be noted that this boundary condition is only valid when the dimensionless distance to the first grid point, y+, is outside the viscous sublayer and in the logarithmic region (i.e. y+ > 30).

Wall functions are sensitive to the first calculation point above the boundary (Wilcox, 1998). The pressure gradient should be included if solutions independent of the matching point are sought. Wall functions do not hold for flow near solid boundaries and for separated flows, in particular.

The turbulence kinetic energy, k, wall function, kqRWallFunction, and the specific dissipation rate, ω, wall function, omegaWallFunction, are defined by the following expressions:

$$k = \frac{u_\tau^2}{\sqrt{\beta_o^*}} \qquad \omega = \frac{k^{1/2}}{(\beta_o^*)^{1/4}\kappa y}$$

3.6.4 Complications with Turbulence Models

The solutions to two-equation turbulence models are sensitive to free-stream boundary condition values of the turbulence parameters even if the turbulence values are selected such that they are very small on the boundaries (Wilcox, 1998). For instance, if the free-stream value of the specific dissipation rate, ω, is small and is less than 0.1% of the peak value, the effect is negligible. However, if free-stream value of ω is larger, even as little as 1%, it is likely to relate to a physically unrealistic value.

There is a dependency between the dissipation rate, the specific dissipation rate and the turbulence kinetic energy (Wilcox, 1998). In free shear flows where the free-stream turbulent kinetic energy, k, and specific dissipation rate, ω, are small, this dependency can act to enhance the production of ω, which reduced the net production of k in turn. This dependency, which is proportional to the gradient of k and ω, is known as *cross diffusion*.

3.7 Errors and Convergence

3.7.1 Error

The solutions given by CWE simulations are only approximate (Ferzinger and Peric, 2002). There are a number of different sources that contribute to the error of CWE simulations.

Modeling errors arise from the mathematical models simplification of the mathematical model and reflect the difference between the actual flow and the flow predicted by the mathematical model.

Discretization errors relate to the differences between the solution of the algebraic equations evaluated on the discretized domain and the exact solution of the mathematical model. While *iterative errors* relate to those the differences in solving the solution in an iterative fashion rather than solving a series of simultaneous equations.

Other sources of error include, *computer round-off errors* are the result of low precision in the calculation of variable and *computer-programming errors* arising from mistakes made by the programmer in coding the algorithm.

Ideally, we wish to establish the modeling error when we compare the numerical solution with the actual result. A solution where the discretization and iterative errors are minimized is sought. A solution where further temporal and spatial discretization does not alter the solution is known as a grid independent solution. The convergence of the algorithm must be assessed to evaluate grid independence.

3.7.2 Convergence

For a numerical solution to be convergent, it must be both consistent and stable (Ferzinger and Peric, 2002). A numerical solution is considered *consistent* if the solution becomes exact as the grid spacing and time step tend to zero. It is *stable* if it does not magnify errors. If a problem is evaluated on finer grids and smaller time-steps, the solution should tend to grid independence if it is stable and consistent.

A common procedure for determining if a solution has converged is based on difference between iterations (Ferzinger & Peric, 2002). The iteration is stopped when the difference is small when compared with norm. Normalization is necessary as without it, the difference may be small but the error may not. Typically, the error is normalized with respect to the largest eigenvalue (i.e. spectral radius). However, if the eigenvalues are complex, this can lead to a poor estimate of convergence.

An alternative approach is to use the residual as the stopping criteria. Although the residual and error are not necessarily equivalent at the start of the iterative process but a reduction in the residual is equivalent to a reduction in error.

3.8 OpenFOAM

Open Source Field Operation and Manipulation (OpenFOAM) is an open source C++ Library of applications used for solving problems in continuum mechanics (OpenFOAM Guide, 2014).

The main advantage of OpenFOAM is that it is an open source package that contains a wide variety of applications for solving a broad range of continuum mechanics problems. Given that it is an open source package, it is possible to access the underlying code and make modifications to it as necessary. Moreover, it has been designed such that it is easily parallelized with only the minimal amount of effort. This is evermore powerful given that it can accommodate both structured and unstructured polyhedral grids. Furthermore, it utilizes a friendly syntax for the implementation of PDEs, which allows for easy checking of the underlying algorithm.

OpenFOAM is not without disadvantages and these largely emanate from it being open source. The documentation and support available to those using OpenFOAM is limited. It consists of online guides and fora, although it is possible to receive training in the use of OpenFOAM.

There are two kinds of applications in OpenFOAM: solvers and utilities. Solvers are developed to tackle specific continuum mechanics problems while utilities are used for tasks that involve data manipulation. Typically, utilities are primarily used in the pre-processing and post-processing stages of a simulation while a standard solver is used to develop the solution to the specific problem. However, it is possible to generate user-defined applications or alter existing standard applications provided the developer has sufficient knowledge of the underlying physics, the solution method and the programming techniques.

Although OpenFOAM can be used to solve a wide variety of problems in continuum mechanics, the file structure used in each of these cases is consistent. Each case must contain three key directories: *system*, *constant* and *time* directories.

Figure 3.1: OpenFOAM case directory structure

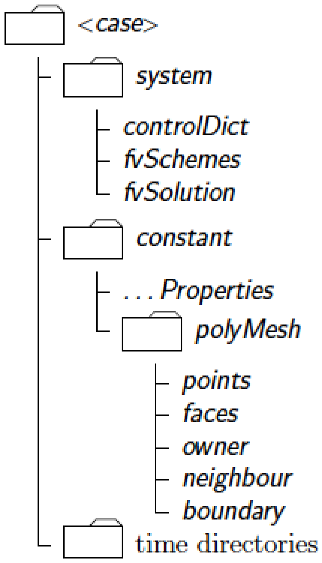

The files in the *system* directory sets out the solution procedure such as run time controls, discretization schemes, solution methods and convergence parameters. In addition, any pre-processing or post-processing utilities undertaken as part of the simulation will be contained within this directory also.

The *constant* directory contains a full description of the numerical mesh as well as the physical properties of the medium (e.g. material or fluid) relevant to the problem under consideration. If the simulation requires the use of a turbulence model, the description of the model will be contained in this directory.

The *time* directories are whether the initial and boundary conditions are defined. It contains data files for each field at each time step. The fields in OpenFOAM must always be initialized for the application to run even if the solver or utility does not strictly require it. Therefore, there must be at least one time step in this directory for any simulation to run.

Chapter 4

Experimental Design Technique

4.1 Introduction

As revealed in the previous chapter, there are many sources of error in CWE simulations. It is essential that CWE models undergo V & V procedures to enhance credibility in the solution.

Verification is the process of identifying; quantifying and reducing errors caused transforming the mathematical model into computer code (Oberkampf and Trucano, 2007). In other words, verification seeks to resolve the question: is it solving the equations right.

Validation is the process of establishing if the mathematical model gives an accurate solution to the problem, assuming the computational model is implemented correctly (Oberkampf and Trucano, 2007). In other words, validation to answer the question: is it solving the right equations.

Oberkampf and Trucano (2007) recommend the development of benchmark experiments for code verification and validation. They suggest that these cases are ideally independent and that validation is a blind test to avoid the risk calibrating the model. In developing benchmark model for verification and validation, the solution to these problems must be known and therefore, the types of solutions can only be developed for simple cases. The problems investigated using CWE are generally considerably more complex than those developed as benchmark cases. This raises the question: can benchmark testing assess the adequacy of a certain CWE model for a certain application? This study investigates the use of an alternative V & V method for the evaluation of errors and uncertainties in CWE simulations based on experimental design.

4.2 Experimental Design Approaches

Experimentation is carried out to get a greater understanding of a particular process. A process can be considered an operation that transforms input parameters into output responses as illustrated in schematic below. Each experimental result can help characterize the relationship between the inputs and the responses. The purpose of experimental design is to direct how this experimentation is undertaken such that the objectives are achieved with the minimal amount of effort (Yeo, 2013). The evaluation of the influence of one or more input parameters on one or more output responses is achieved in an efficient manner through the use of statistics.

Figure 4.1: Schematic of Block Box Process Model (Yeo, 2013?)

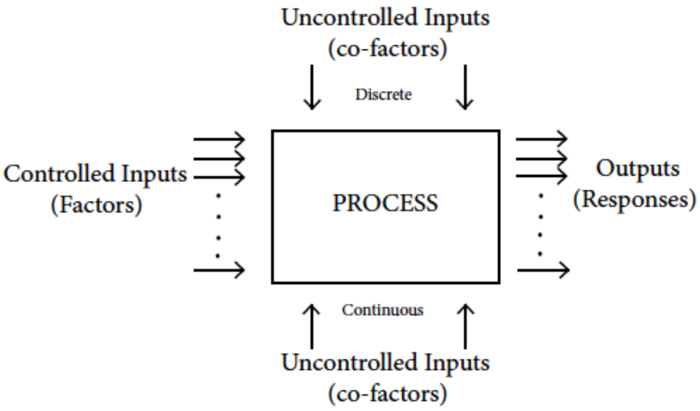

4.3 Traditional Approach

A traditional approach to experimental design involves only changing a single input parameter between runs, which is known as the *one factor-at-a-time* (1FAT) design (Box, 1978) (Yeo, 2013). As noted by Box et al (1978), “the method provides an estimate of the effect of a single variable at selected *fixed* conditions of the other variables”. It assumes the effect would be the same irrespective of the condition of the other variables and therefore, it neglects any interaction between variables. Given that

1FAT design approach ignores interactions, its estimates are biased and lack precision if the interaction between any variables is significant.

4.4 Factorial Design Approach

4.4.1 Orthogonality

It is possible to design experiments such that the interaction between parameters can be taken into account. This can be achieved by ensuring orthogonality between experiments (Yeo, 2013). In other words, the input parameters for each experiment are specified such that the inputs cannot be replicated from the linear combination of any other experiments. In the analysis of the responses, it is possible to isolate the effects associated with any input parameter or interaction through the appropriate combination of experiments. Therefore, this property facilitates the adjustment of multiple input parameters between experiments, which takes interactions between factors into account, while, at the same time, permitting the independent estimation of the effect associated with any parameter or interaction. Moreover, the interpretation of the results is relatively straightforward, as it only requires the use of common sense and elementary arithmetic.

4.4.2 Full Factorial Design

In a factorial design, each input parameter is evaluated at two or more values or levels. *Full factorial design* considers all possible combinations of the input parameters (Yeo, 2013). However, it makes use of orthogonality, which results in a reduction in the number of experiments when compared with 1FAT (Box et al, 1978). In addition, this approach takes interaction into account due to the use of orthogonality and therefore, has the added advantage of providing a more accurate evaluation of the responses. However, the number of experiments associated with full factorial designs that include assessment of 5 input parameters over more than 2 levels becomes increasing large. This can be become unmanageable depending on the resources available.

4.4.3 Fractional Factorial Design

It should be noted when considering a large number of factors that some factors are more influential than others (Box et al, 1978). In certain cases, an input parameter may have no distinguishable effects at all. Furthermore, all the interactions between input parameters are considered in a full factorial design. However, the influence of the interactions on the response tends to decrease as the order increases. In light of this, it is possible to determine the effects of the various input parameters and their interactions without considering all the combinations. According to Box et al (1978), the *"fractional factorial design exploits this redundancy"* inherent within the full fractional design to reduce the number of experiments required without compromising the accuracy of the estimates. Instead of using all possible combinations of the input parameters, this approach uses only a subset (Yeo, 2013). In some cases, this can reduce effort significantly when compared to the traditional or the full factorial design approaches. A fractional factorial design approach was adopted as the experimental technique in this study.

4.4.4 Construction of Fractional Factorial Design

In order to perform a general factorial design, it is first necessary to determine the number of factors to be investigated and to select the number of levels at which each factor is evaluated (Box et al, 1978). A full factorial design contains all the combinations of these variables at all the different levels. For instance, consider a full factorial design where there are four factors under investigation with each factor evaluated at two different levels. Under these circumstances, the design would require 2 x 2 x 2 x 2 = 16 different runs. The table below outlines the various combinations of parameters giving the 16 experimental cases where the maximum and minimum levels of each parameter are represented by the plus (+) and minus (-) signs, respectively.

Table 4.1: Tabular Representation of Full Factorial Design (4 Factors)

Case	Factor				Case	Factor			
	1	2	3	4		1	2	3	4
1	-	-	-	-	9	-	-	-	+
2	+	-	-	-	10	+	-	-	+
3	-	+	-	-	11	-	+	-	+
4	+	+	-	-	12	+	+	-	+
5	-	-	+	-	13	-	-	+	+
6	+	-	+	-	14	+	-	+	+
7	-	+	+	-	15	-	+	+	+
8	+	+	+	-	16	+	+	+	+

The relationships among the factors can also be represented using the following visual representation. Each axis represents a different factor and the vertices represent the relationship between the factors for each individual run. When the number of factors under consideration exceeds 3, the subsequent factors are represented through the provision of additional blocks.

Figure 4.2: Visual Representation of Full Factorial Design (4 Factors)

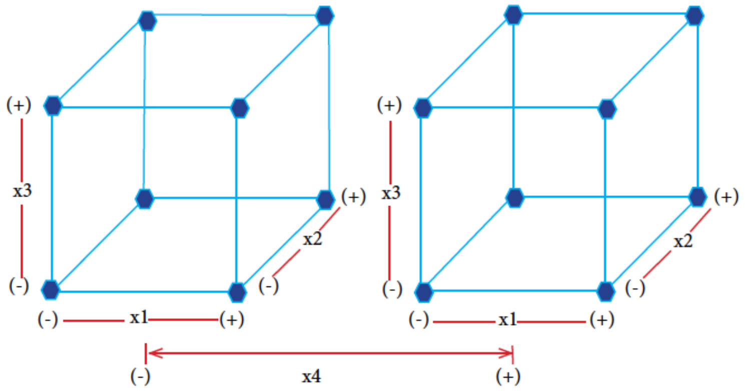

The fractional factorial design is constructed in a similar manner except some of the experiments are omitted (Box et al, 1978). In order to determine the experiments omitted or retained in the fractional factorial design, a relation known as the *generator* is defined between the various factors being investigated. The experiments are retained or omitted based on the generator. For instance, a half fractional factorial design for the above table can be developed using the generator, **123** = **4** (note: the interaction **123** indicates the elements of columns **1**, **2** and **3** are multiplied together). In this instance, the half fractional factorial requires only 8 experiments to be carried out instead of 16 as outlined in the table below.

Table 4.2: Tabular Representation of Half Fractional Factorial Design (4 Factors)

Case	**Factor**				**Case**	**Factor**			
	1	**2**	**3**	**4**		**1**	**2**	**3**	**4**
1	-	-	-	-	5	-	-	+	+
2	+	-	-	+	6	+	-	+	-
3	-	+	-	+	7	-	+	+	-
4	+	+	-	-	8	+	+	+	+

As is the case with a full factorial design, a fractional factorial design can be represented visually as shown below.

Figure 4.3: Visual Representation of Half Fractional Factorial Design (4 Factors)

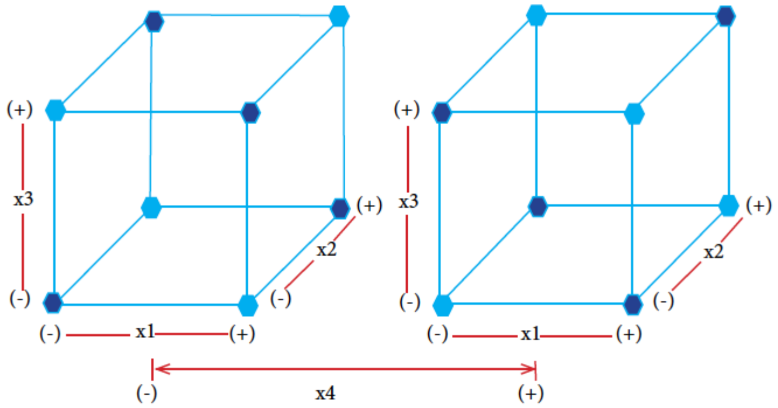

It should be noted that the reduction in the total number experiments requires has not come without cost. Due to the relationship defined by the generator, the responses of the variables described in this relationship become intertwined (i.e., **12** and **3**) and further experiments are necessary to extract the different responses.

4.4.5 Calculation of Effects

Using factorial design, it is possible to evaluate the *effect* of a factor or interaction on the response, where an effect is defined as a change in the response as the factor proceeds from one level to another (Box et al, 1978).

The *main effect* of a factor is the average change measured over all the conditions of the other variables. It can be calculated by contrasting the average response when the factor is at a high level with the average response when the factor is at a low level. For example, the main effect of the first factor in Table 4.2 is calculated as follows:

$$E_M = \frac{r_2 + r_4 + r_6 + r_8}{4} - \frac{r_1 + r_3 + r_5 + r_7}{4}$$

where E_M is the main effect and r_n is the response of experiment n.

Figure 4.4: Visual Representation of Calculation of Main Effects

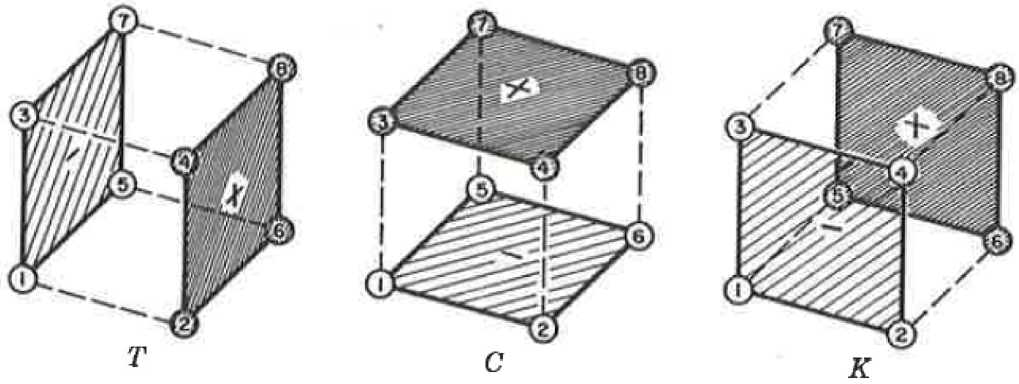

An interaction effect is considered to have occurred when the combined effect of two factors or more acting together is different from the effect of the individual factors combined. Similar to main effects, *interaction effects* are calculated as the difference between averages, however, the averages relate to multiple rather than individual factors. For example, the interaction effect of the first factor and the third factor in Table 4.2 is calculated as follows:

$$E_I = \frac{r_1 + r_3 + r_6 + r_8}{4} - \frac{r_2 + r_4 + r_5 + r_7}{4}$$

where E_I is the interaction effect and r_n is the response of experiment n.

Figure 4.4: Visual Representation of Calculation of Two Factor Interactions

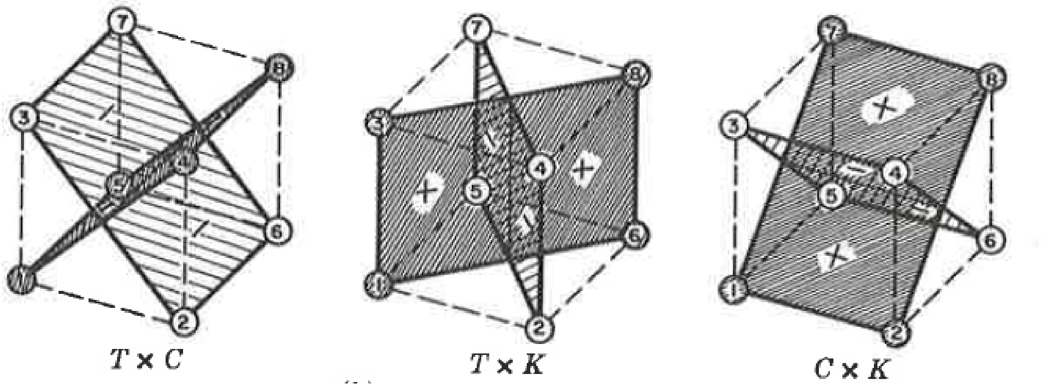

Figure 4.5: Visual Representation of Calculation of Three Factor Interactions

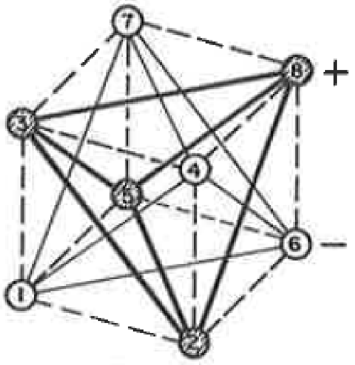

Quicker methods for calculating main and interaction effects include *table of contrast coefficients* or the *Yate's algorithm* (Box et al, 1978).

4.4.6 Interpretation of Results

A factor is considered to have a significant effect if the deviation it causes is in excess of that attributable to standard errors (Box et al, 1978). If higher order interactions (i.e. greater than 2) are supposed negligible then the differences in these interactions can be largely attributed to experimental error. This can then provide an appropriate reference for determining if a certain effect is significant or not. The main effect associated with a single variable should only warrant consideration if there is no evidence of interaction with other variables. Otherwise if interaction effects have been identified, the interacting factors should be considered jointly.

In addition to carrying out simulations in accordance with the factorial or fractional factorial approach, an additional simulation will be undertaken, which is called the *target case,* where all the experimental parameters are assigned intermediate values. Plots will be prepared for each variable considered in the experimental design, comparing the estimated mean values given the various levels (including the intermediate level) of the relevant experimental parameters, as shown in the sample plot below. In addition, the plot will contain the maximum and minimum values of the variable for a given level of the experimental parameter. The intention is that this will give some indication as to the variation in the value of the variable given for a particular parameter level.

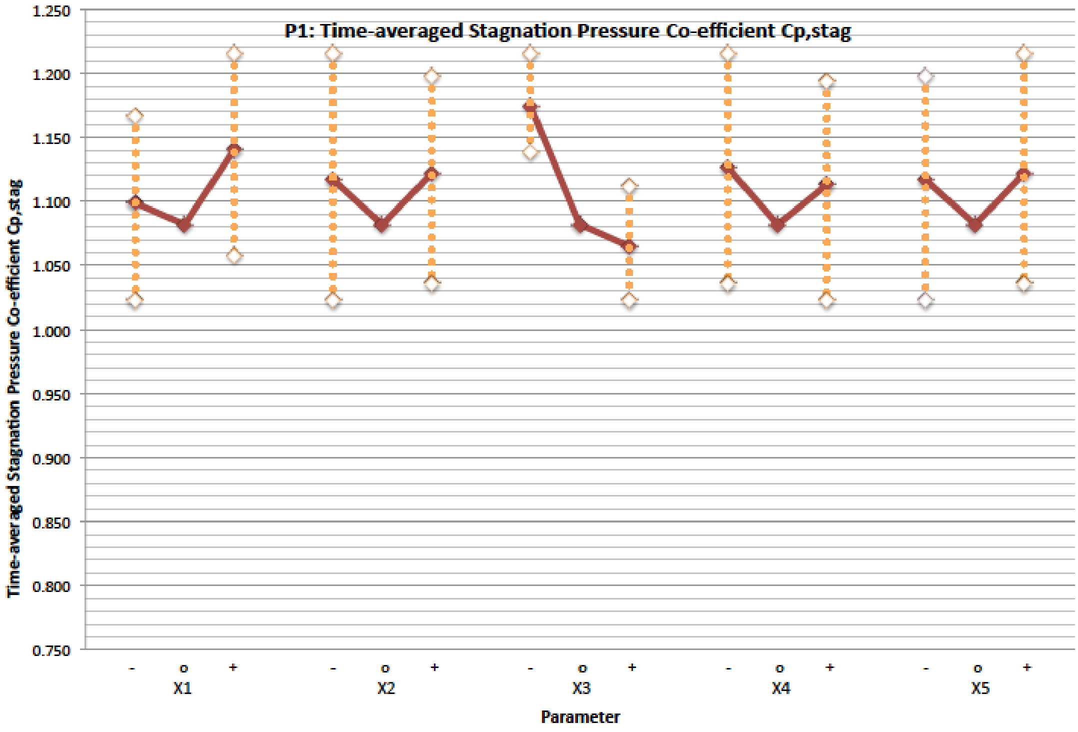

The main effects of a factor on a variable can be determined through visual inspection of this plot. In addition, it is possible to evaluate the main effect of certain factors over others for a particular variable. However, the plots will not assist with identifying interaction effects.

4.5 Verification and Validation

It should be noted that OpenFOAM is written using the C++ programming language, which was developed over 30 years ago. Although there may be concerns regarding the implementation of the CWE code, the fundamental underlying software is known to be reliable and repeatable. Therefore, the primary concerns of the verification step relate to algorithm verification and numerical error evaluation.

It is proposed to carry out a series of simulations based on the factorial or fractional factorial design approach for the verification stage. This approach allows evaluation of the sensitivity of the CWE simulation to changes in experimental parameters such as grid mesh size, time-step size, computational domain dimensions or other conditions of the simulations. The ultimate goal would be to identify the suitable experimental parameters that provide a parameter independent solution such that errors are minimized. This is a similar approach to Richardson extrapolation seeking convergence through spatial and temporal refinement (Roache, 2009).

Once the appropriate experimental parameters for a parameter independent solution are known, a final simulation based on these parameters can be run. A comparison of the results on this simulation with pre-existing experimental results allows for the validation of the CWE model.

Chapter 5

Numerical Set-up

5.1 Introduction

This study is concerned with developing a robust and reliable approach to the V & V of a CWE (OpenFOAM) simulation of flow around a square body, which is a simple but crude representation of a building or bridge cross-section.

The verification stage consists of examining different simulation parameters over a range of values for flow around a 2D square cylinder using the fractional factorial design approach. The intention of this sensitivity analysis is to understand the influence of each of the parameters on the solution and therefore, identify the optimal arrangement of experimental parameters to achieve a grid independent solution, where numerical errors are minimized.

The validation stage consists of comparing a CWE solution for flow around a square body with experimental results from past wind tunnel test studies. The configuration of validation model is strongly influenced by the findings of the verification stage; however, the model extends into the third dimension due to the 3D nature of both vorticity and turbulence.

Both V & V stages make use of the same numerical solvers in developing a solution. In addition, all simulations are performed on the same Linux cluster. Due to time constraints regarding the completion of this study, the total duration of each simulation was 15 seconds and 6 seconds for the verification and validation stages, respectively. However, only the final 3 seconds was considered for the analysis for both stages.

The computational domain, spatial discretization (mesh), temporal discretization (time-step) and boundary conditions used in each of the OpenFOAM simulations are discussed below.

5.1.1 Cluster

The simulations are run a Linux-based Penguin cluster. The following are some details regarding the cluster:

- Number of nodes: 24
- Processors per node: 2 eight-core processors
- Memory: 128 GB RAM per node (64 GB RAM per core)
- Storage: 1 TB scratch memory per node

5.1.2 Solvers

OpenFOAM is used for the running of the CWE simulations. A steady state simulation is required to determine the initial pressure and velocity fields throughout the computational domain. The simpleFoam application, which is an implementation of the SIMPLE algorithm in OpenFOAM, enables a steady state solution to be determined. After these fields are initialized, it is possible to evaluate the transient solution. This is achieved using the pimpleFoam application, which is an implementation of the PIMPLE algorithm in OpenFOAM. Both the steady state and transient simulations consider turbulence. The turbulent effects are approximated using the k-omega turbulence model and wall functions (kqRWallFunction and omegaWallFunction) are specified on the boundary surfaces of the square box.

The solutions to both the steady state and transient simulations are derived in the same fashion with only a few notable exceptions. For instance, the time integration scheme for the steady state simulation utilizes a steady state method, as might be expected, while the Crank-Nicolson method, using a beta value of 1, is adopted for the transient simulation. Another difference is found in the approximation of divergence of the turbulent kinetic energy, k, and the specific dissipative rate, ω. The k and ω fields are approximated using a bounded upwind scheme in the steady state simulations and a Gauss linear limited scheme in the transient case. This modification is required to ensure that the oscillations in the solution are not restricted in the transient case due the approximation method used. Otherwise, all other approximations are the same.

The gradient scheme utilizes a Gauss linear approximation for all fields. A bounded Gauss linear upwind scheme and a Gauss linear scheme are adopted to approximate the divergence of velocity and turbulent transport in the k-omega turbulence model, respectively. A Gauss linear limited corrected scheme is utilized to approximate the Laplacian terms.

The discretized algebraic equations are solved using a generalized generic-algebraic multi-grid solver (GAMG) that utilizes a Gauss Seidel smoother. GAMG involves deriving a solution on a small coarse grid and applying that solution to a finer mesh, as an initial guess, before obtaining a more accurate solution on the finer mesh.

The simulations were run in parallel using the ‘simple’ decomposition method in OpenFOAM. The computational domain is divided in a prescribed number of sub-domains in each direction.

5.2 Stage I: Verification

In the verification stage, the two-dimensional flow around a square cylinder is examined. The free-stream velocity, U_∞, is taken as 8.2 m/s. The square box has a characteristic dimension, H, of 0.04 m. The flow medium is air, which has a density, ρ, of 1.20 kg/m^3 and a kinematic viscosity, ν, of 1.51 x 10^{-5} m^2/s. This gives a

Reynolds number, Re, for the flow of 20,000. The turbulence intensity, I, is assumed at 2%.

The investigation is carried out using the fractional factorial design approach. The following five experimental parameters are investigated for their influence on the solution:

- x1: grid refinement
- x2: time-step
- x3: upstream length
- x4: downstream length
- x5: cross-stream half-width

Each of the experimental parameters is investigated at three levels: a low level, a high level and an intermediate value, which is referred to as the target value. The orthogonal fractional factorial design for 5 factors is summarized in the table below.

Figure 5.1: Computational domain and experimental parameters for Stage I

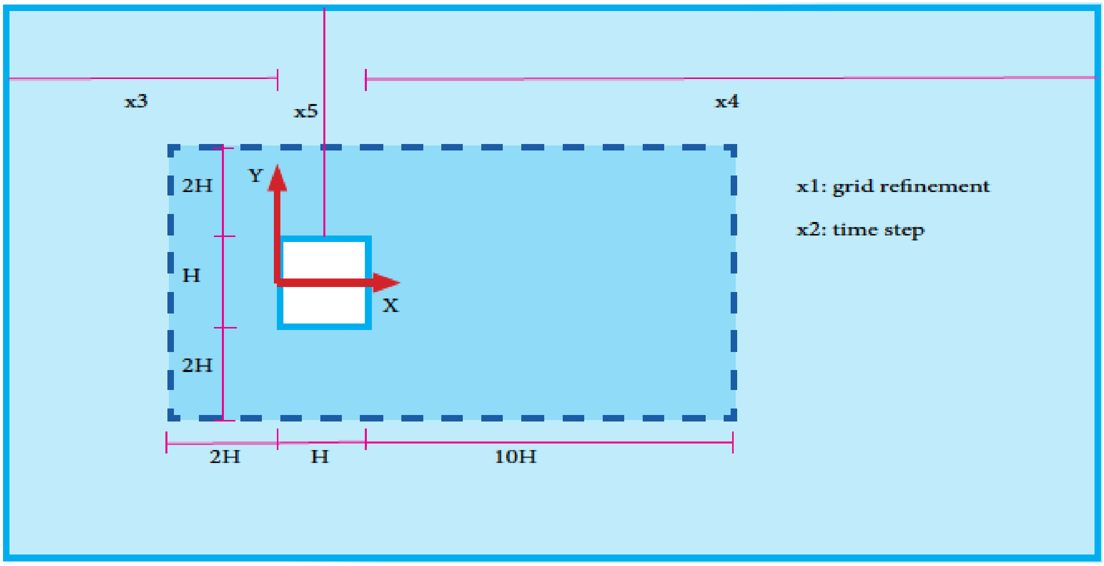

Table 5.1: Simulation cases for Stage I: Verification

Simulation Parameter	Grid Mesh	Time-step	Domain Size		
			Upstream	Downstream	X-stream
increase (+)	H/24	0.000125	15H	30H	20H
neutral (o)	H/16	0.000250	10H	20H	15H
decrease (-)	H/8	0.000500	5H	10H	10H
Case Ref					
1	-	-	-	-	+
2	+	-	-	-	-
3	-	+	-	-	-
4	+	+	-	-	+
5	-	-	+	-	-
6	+	-	+	-	+
7	-	+	+	-	+
8	+	+	+	-	-
9	-	-	-	+	-
10	+	-	-	+	+
11	-	+	-	+	+
12	+	+	-	+	-
13	-	-	+	+	+
14	+	-	+	+	-
15	-	+	+	+	-
16	+	+	+	+	+
17	o	o	o	o	o

5.2.1 Mesh

The numerical solution can be sensitive to mesh configurations. It can influence the stability of the numerical method and therefore, it impacts whether the solution converges or not. The selection of the mesh refinement (x1) attempts to bound the influence of the mesh on the solution. Therefore, the objective is to specify a coarse mesh size (i.e., H/8) that will result in a poor approximation of the solution and a fine mesh size that will provide a good approximation of the solution.

In the interest of simplicity, a uniform orthogonal hexagonal mesh (i.e., H/8) is used across much of the computational domain. The mesh is refined in the vicinity of the square obstruction. The refinement zone is a rectangular zone that extends 2H upstream of the square box, 10H downstream of the rear of the body and 2H in the cross-stream direction. The mesh is uniform across this region. Depending on the simulation case, the mesh size is H/8, H/16 or H/24, as appropriate. The mesh in the refinement zone consists largely of orthogonal hexagonal cells, except in the buffer layers between meshes of different sizes, where some cells are prismatic in shape. It should be noted that for cases when the mesh in the refinement zone is H/24, the mesh in the rest of the domain was reduced to H/6 to facilitate buffering between layers of different sizes.

5.2.2 Time-step

For transient solvers such as the PISO algorithm, the time-step, Δt, is critical in ensuring the stability of the method depending on the mesh size, and therefore, influences convergence of the solution. Typically, stability is assured if the Courant-Freidrichs-Lewy number (CFL) is less than 1. However, the PIMPLE algorithm does not have the same strict stability requirement as it takes advantage of under-relaxation to converge to a stable solution. Therefore, relatively large time-steps are considered in this study. The minimum and maximum time-steps are 0.000125 seconds and 0.0005 seconds, respectively, with 0.00025 seconds as the target time-step. Therefore, the non-dimensional time-step, Δt^*, has a range between 0.0256 and 0.1052.

5.2.3 Domain

The extent of the computational domain is important. If the domain is too small, the conditions specified on the boundaries can influence the result, On the other hand if the domain is too large, it can require a significant amount of computational effort to arrive at a solution. The selection of different domain sizes in the upstream, downstream and cross-stream directions seeks to identify the limits of their influence on the solution. This selection is informed by the domain sizes used in previous numerical studies. On this basis, the upstream length (x3) is specified as 5H and 15H for the low and high levels, respectively, with target value given as 10H. The minimum and maximum downstream lengths (x4) are given as 10H and 30H, respectively, with a target value of 20H. Finally, the cross-section half-width varies between a minimum of 10H and a maximum of 20H. The target value is given as 15H.

5.2.4 Boundary Conditions

The initial and boundary conditions are specified on the boundaries of the domain. In the present study, the domain has the following boundaries: *inlet*, *outlet*, *top*, and *bottom* of the computational domain and surfaces of the *squareBox*.

The conditions applied on these boundaries are consistent with the recommendations of Ferzinger and Peric (2002) and is similar to those applied by Tian et al (2012).

A uniform flow condition, $u_1 = U_\infty, u_2 = 0,$ is set on the inlet boundary. The pressure is specified as a zero normal gradient. The turbulent kinetic energy, k_{inlet}, and the specific dissipative rate, ω_{inlet}, are calculated using the following equations:

$$k_{inlet} = 1.5(U_\infty I)^2 \quad \omega_{inlet} = \frac{k_{inlet}^{1/2}}{\left(C_\mu^{1/4}\ell\right)}$$

where $C_\mu \approx 0.09$ and the turbulence length scale is taken as l = 0.07H.

The velocities (u_1 and u_2), the turbulent kinetic energy, k, and specific dissipative rate, ω, are specified as zero normal gradients on the outlet boundary. The pressure on this boundary is also set to zero, which is consistent with Shimada and Isihara (2002).

A k-omega wall function is specified on the surface of the square cylinder, (i.e., squareBox). The velocity condition is applied as $u_1 = 0$ and $u_2 = 0$ and the pressure condition is given as zero normal gradient. The turbulence kinetic energy, k, is specified as zero while the specific dissipative rate, ω, is calculated using the following formula:

$$\omega_{body} = 10 \times \frac{6\nu}{\beta_1 (y)^2}$$

where is the distance from the surface to the nearest computational node.

The 'slip' condition is applied to the top and bottom boundaries, which ensures that there is no flow through the boundary but only flow parallel to the boundary only. In OpenFOAM, the spatial discretization is achieved using 3D cells, however, the domain consists of a single plane of cells and therefore, the width of the domain is extremely small (e.g. H/8) in comparison to the width of the domain in the other two dimensions (e.g. 21H). The front and back patches are specified as 'empty', which ensures the simulation is 2D.

5.3 Stage II: Validation

In the validation stage, the flow around a 3D square cylinder is examined. The major difference is that the square cylinder is no longer planar but extends 2H in the spanwise direction (z-direction). The same flow conditions used for the 2D simulation are specified for the 3D simulation. Ideally, there would be a 3D verification stage preceding the validation stage, however due to time constraints, it was not possible to conduct the stage before progressing to validation of the model.

Figure 5.2: Computational domain for Stage II

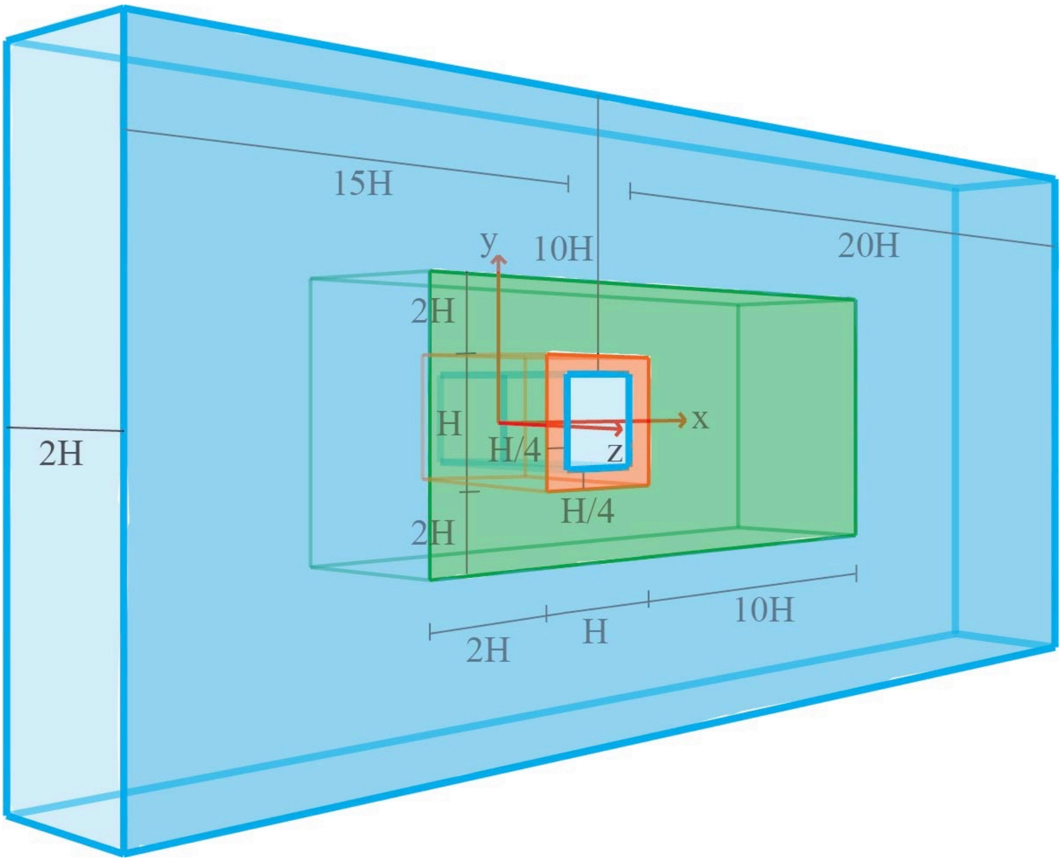

5.3.1 *Mesh*

A similar mesh is adopted in the validation stage to the mesh used for the verification stage. The domain mostly consists of a uniform orthogonal hexagonal mesh (i.e., H/6). The mesh is refined (i.e. H/12) surrounding the square prism for a distance 2H upstream and in the cross-stream dierctions,10H downstream and for the entire spanwise width of the computational domain. The mesh immediately surrounding the square prism (i.e., within a distance of H/4 from the body) is refined further (i.e., H/24). As before, the orthogonal hexagonal mesh is maintained throughout for the most part, except in the buffer layers, where some cells are prismatic in shape.

5.3.2 Time-step

As stated above, the PIMPLE algorithm does not have the same strict stability requirement as it takes advantage of under-relaxation to converge to a stable solution. However, if the time-step is too large, the solution can become unstable. Although no the two-dimensional problems do not suffer from numerical instability, the three-dimensional simulation is not as stable. Therefore, the time-step of 0.000125 seconds or 0.0256 in non-dimensional time is taken as the time-step for the validation of the CWE model.

5.3.3 Domain

For the validation case, the upstream length is specified as 15H, the downstream length is 20H and the cross-section half-width is assigned the value 10H. The cross-stream width is taken as 2H. Therefore, the computational domain has an overall size of 26H x 21H x 2H.

Table 5.2: Simulation case for Stage II: Validation

Simulation Parameter	**Grid Mesh**	**Time-step**	**Domain Size**		
			Upstream	**Downstream**	**X-stream**
Case Ref					
1	H/6 to H/24	0.000125	15H	10H	20H

5.3.4 Boundary Conditions

The conditions specified on the boundaries are essentially the same as those specified for the verification stage. The only exception is the front and back patches are defined a periodic (cyclic) boundaries. According to the OpenFOAM User Guide (2014), this designation “enables the patches to be treated as if they are physically connected". Therefore, the periodic condition on the front and back boundaries gives the square prism an infinite effective length.

Chapter 6

Stage I: Verification

6.1 Overview

A robust approach to V & V can help improve confidence in CWE solutions. Common V & V approaches adopted in other fields are not necessarily appropriate to CWE due to the complexity of the problems. This study proposes an alternative method for the evaluation of errors and uncertainties in CWE simulations based on the experimental design technique, which is modified from the factorial approach.

This chapter is concerned with the verification of the CWE model. The verification stage involves examining different simulation parameters over a range of values using the fractional factorial design approach for flow around a 2D square cylinder. The purpose is to identify the sensitivity of the CWE simulation to changes in simulation parameters. The intention is to verify the optimal parameters for achieving a parameter-independent solution, where numerical errors are minimized or reduced to an acceptable level.

6.2 Flow Visualization

Paraview, which is an open-source, multi-platform data-analysis and visualization application, enables the visualization of any calculated flow field (e.g., velocity, pressure, turbulent kinetic energy etc.) at any instant in time as shown in Figure 6.1 below.

In Figure 6.1, the color map shows the variation in the magnitude of velocity, where blue and red regions identify regions of low or high velocity flows respectively. The contour lines indicate regions of vorticity. The greater the number of contours the higher the magnitude of vorticity present.

Figure 6.1: case 16 velocity field with vorticity contours at time, t = 14.065s

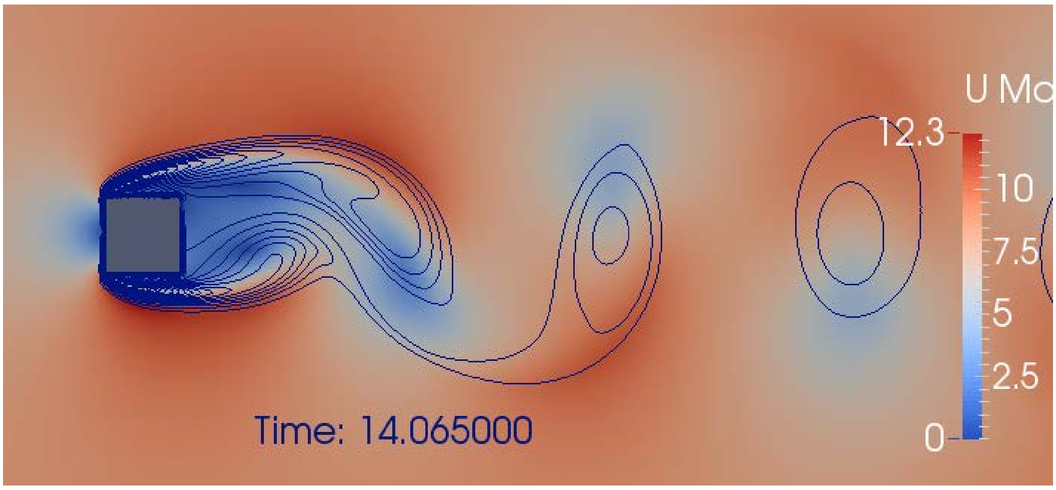

It is clear that the flow accelerated around the body separates at the front corner and forms a free shear layer. An arc of the highest velocity fluid in the domain is found immediately downstream of the front corner separated from the cylinder surface by a region of significantly lower speed recirculating flow. In addition, the vorticity contours form a thin jet-like layer in this region, which is consistent with the presence of a shear layer.

Figure 6.2: case 16 pressure field with vorticity contours at time, t = 14.065s

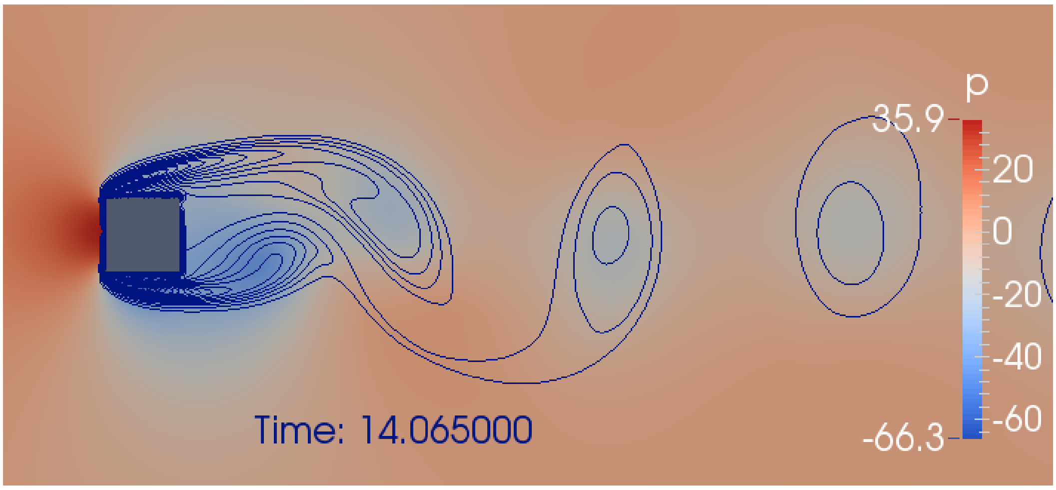

It is apparent that another region of relatively low speed flow exists at the rear of the cylinder. This is coincident with a low-pressure region as shown in Figure 6.2

above, where the variation in pressure is given by the color map. This would indicate the existence of a wake region behind the body.

In addition, the vorticity contours indicate discrete vortical structures present downstream of the body. The low and high velocity fluid on opposite sides of these coherent structures in the cross-stream direction indicate flows travelling in different directions once the translation of the structure downstream is taken into account. In addition, the centers of these contours are associated with areas of low pressure. This indicates the shedding of vortices in the wake of the body.

Furthermore, Paraview permits the evolution of flow field through time to be visualized. The variation of the velocity field with time for a single vortex shedding cycle is shown in Figure 6.3.

Figure 6.3 (a) shows the state of the flow field immediately after a vortex has been shed from the upper face of the cylinder. The upper shear layer is curved and showing significant separation from the boundary surface, while the lower shear layer is closer to the lower face and almost parallel to the surface. This suggests that the upper and lower shear layers are undergoing deceleration and acceleration phases in accordance with Lyn and Rodi (1994). The shear layers transition between (a) and (b) to a more balanced configuration, which is consistent with the assertion of Lyn and Rodi (1994) that the shear shifts rapidly when vortices are shed. The shape and size of the shear layers remains steady between (b) and (c). However, the upper shear layer is drawn across the near wake from (c) to (d) in accordance with the description by Bearman and Trueman (1972) until the lower vortex is shed in (d).

From visual inspection, it appears that the CWE model is consistent with theory. However, this is only a qualitative assessment of the accuracy of the model. It is difficult to quantify the performance of a simulation not to mention distinguish between different simulations. Therefore, it is necessary to analyze the simulations in more objective fashion.

Figure 6.3 case 16 velocity field and vorticity contours varying with time

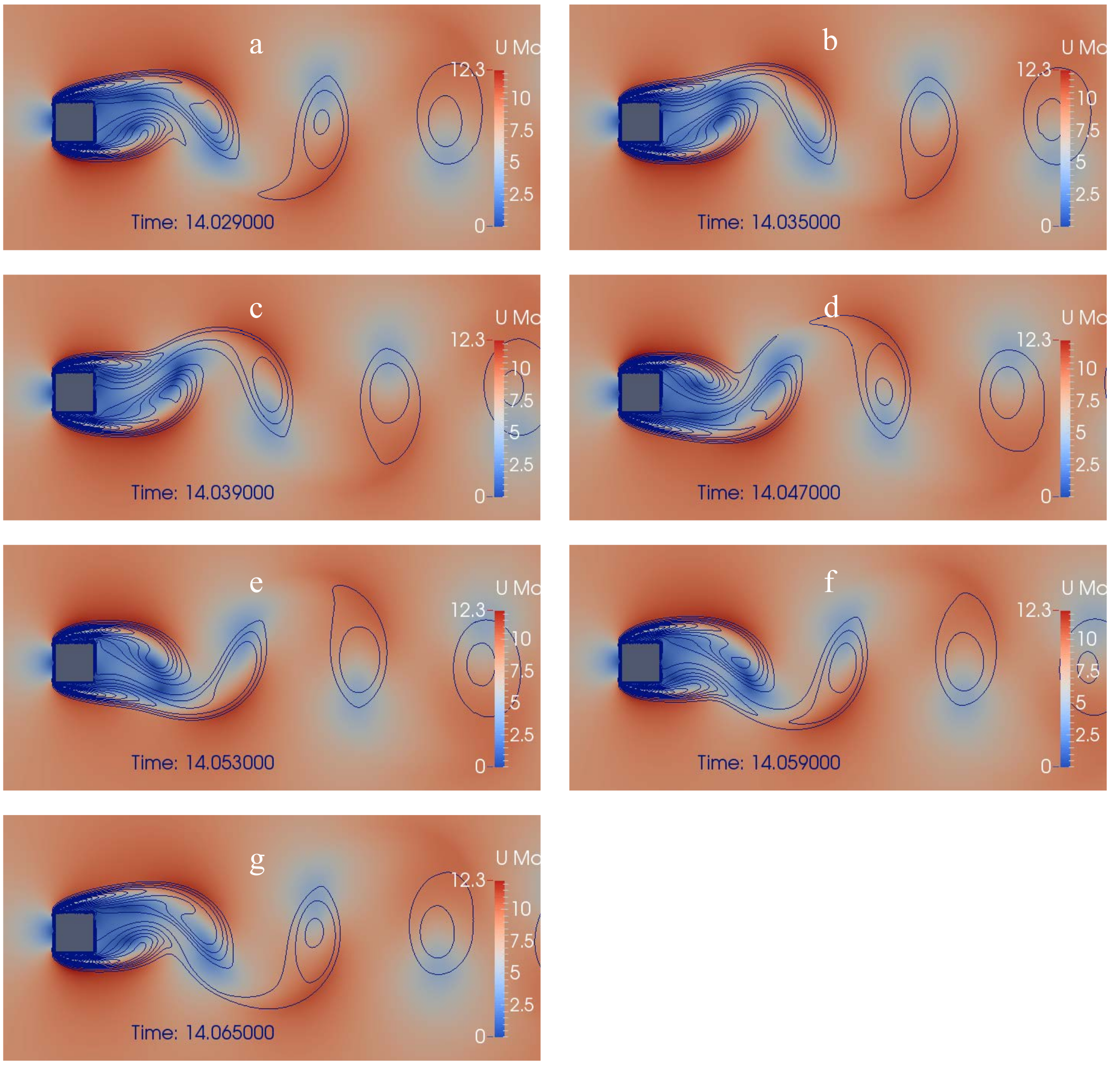

6.3 Velocity and Kinetic Energy

6.3.1 Time-averaged Variables

This section compares the velocity and residual kinetic energy profiles of cases 01, 16 and 17. Case 01 (the coarsest case) is the CWE simulation with the coarsest grid, the largest time step and amongst the smallest computational domain size. On the other hand, case 16 (the finest case) is the opposite, having the finest grid, smallest time-step and largest computational domain size. The intermediate configuration is defined in case 17 (the target case). These cases were chosen for configuration is defined in case 17 (the target case). These cases were chosen for comparative purposes.

Although it may be necessary to use a large computational domain to develop an accurate CWE solution, the entire domain is not necessarily of interest. Instead, the analysis focuses on a few critical locations. For flow around a 2D square cylinder, the area of interest is in the vicinity of the cylinder. This study examines the velocity and residual kinetic energy profiles at the locations indicated in Figure 6.4.

Figure 6.4: Velocity and Kinetic Energy Plot Locations

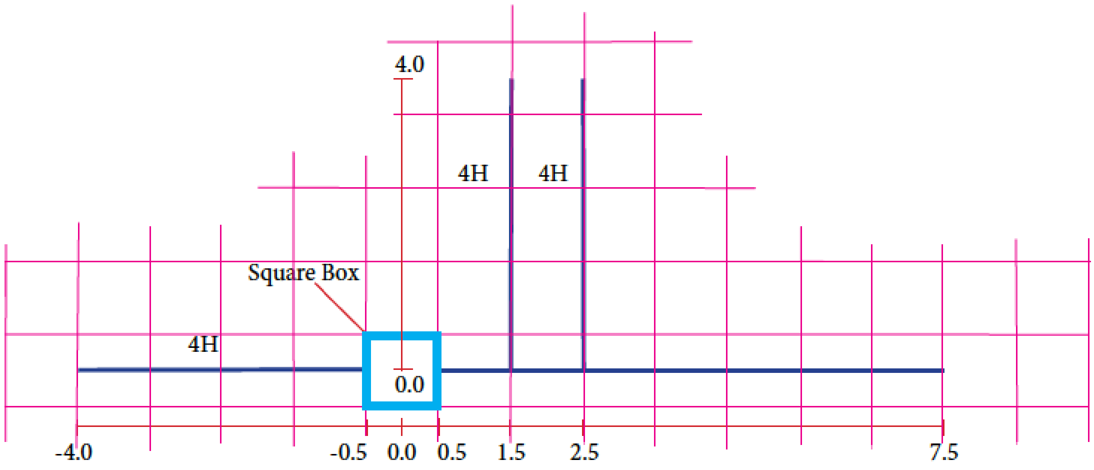

The time-averaged along-wind velocity, u_{ave}, profile along the domain centerline for these cases is defined in Figure 6.5. It would appear that the normalized velocity, u_{ave}/U_{ref}, asymptotes to near unity for the upstream velocity for case 01, where U_{ref} is the free-stream velocity, but it appears to asymptote to a lesser value for the other cases. However, all cases to tend to unity at the inlet but the greater distance of the inlet in both cases 16 and 17 from the first sampling point leads to this apparent discrepancy.

There is a notable difference in downstream velocity, u_{ave}/U_{ref}, when case 01 is compared with the other cases. While both cases 16 and 17 suggest u_{ave}/U_{ref} is marginally above 0.8, case 01 indicates a value slightly under 0.8.

In addition, it is clear that the width of the recirculation zone reduces from the coarsest case to the target case and again from the target case to the finest case.

Figure 6.5: Time-averaged velocity, u_{ave}, profile along centerline

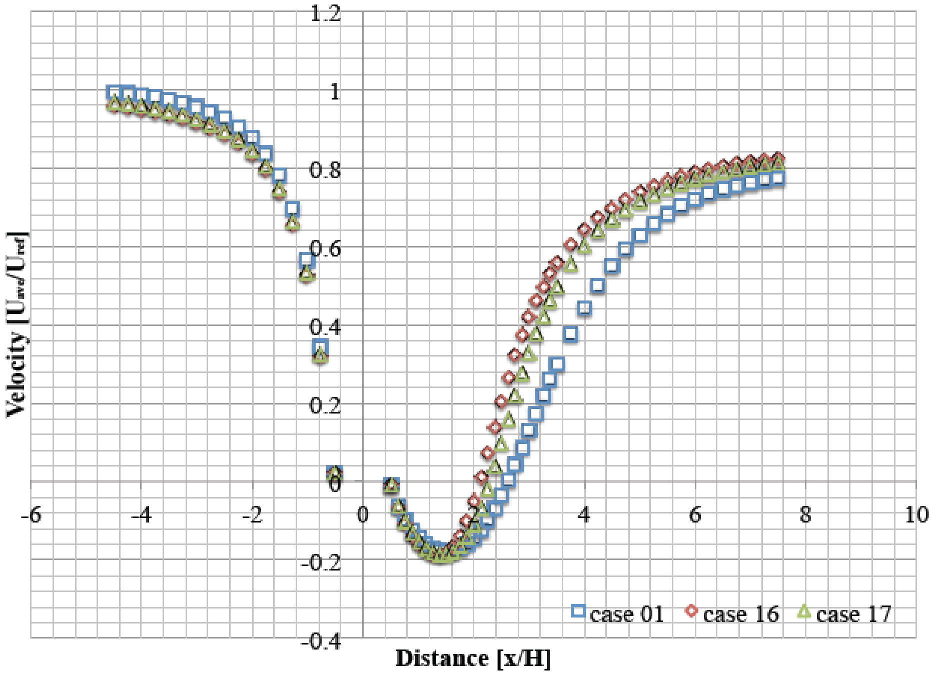

At a distance 1H from the rear face of the cylinder, the time-averaged across wind velocity, $w_{ave,1H}$, profile and the standard deviation of the along wind velocity, $u_{sd,1H}$, profiles across the domain from the centerline for cases 01, 16 and 17 are shown in Figures 6.6 and 6.7, respectively. Note that H is the dimensional length of the square cylinder. In each simulation, the peak $w_{ave,1H}/U_{ref}$ is located between 0.5H and 1.0H of the centerline. The same is true for $u_{sd,1H}/U_{ref}$. However, the peak values of $w_{ave,1H}/U_{ref}$ and $u_{sd,1H}/U_{ref}$ increase with refinement of the simulation parameters.

At a distance 2H from the rear face of the body, the time-averaged across wind velocity, $w_{ave,2H}$, and the standard deviation of the along wind velocity, $u_{sd,2H}$, profiles across the domain from the centerline for cases 01, 16 and 17 are shown in Figures 6.8 and 6.9, respectively. Once more, the peak values of $u_{sd,2H}/U_{ref}$ and

$w_{ave,2H}/U_{ref}$ are situated between 0.5H and 1.0H of the centerline in all cases and the peak values increase with refinement of the simulation parameters.

Figure 6.6: Time-averaged across wind velocity profile at x/H = 1.5

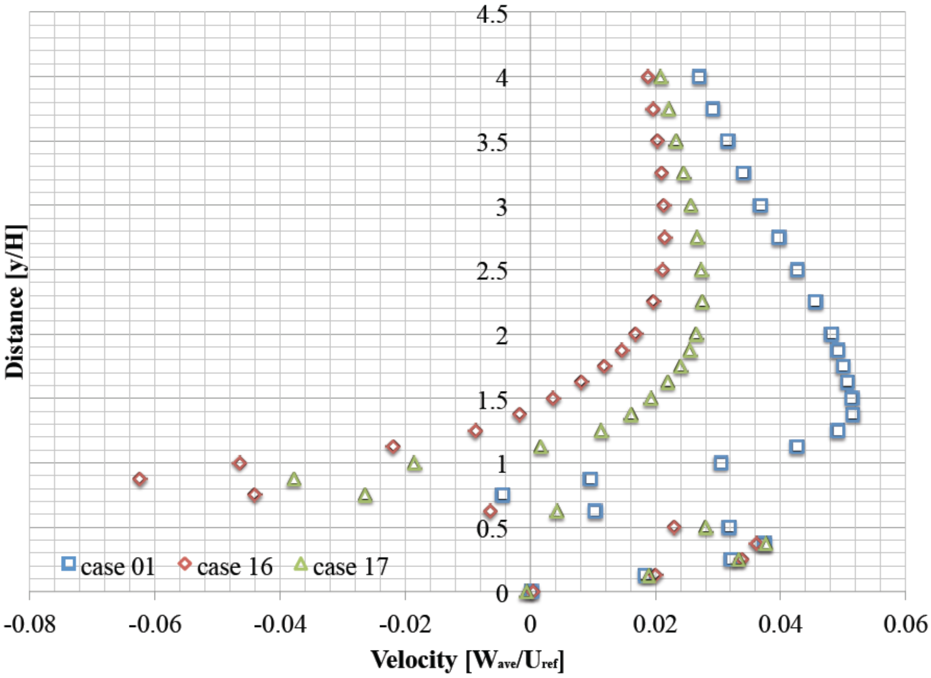

Figure 6.7: Standard deviation of along wind velocity profile at x/H = 1.5

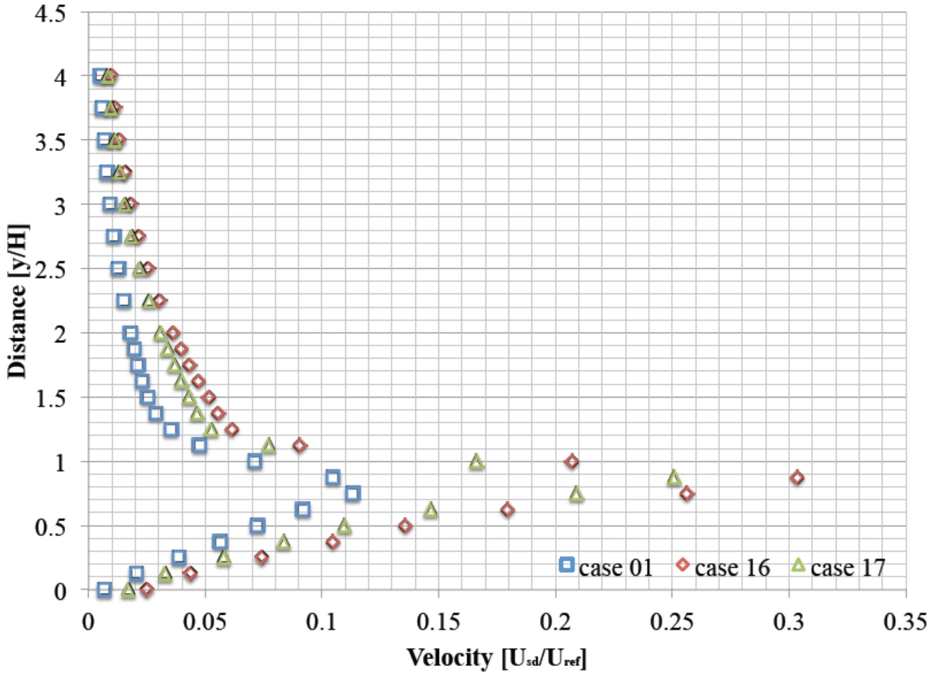

Figure 6.8: Time-averaged across wind velocity profile at x/H = 2.5

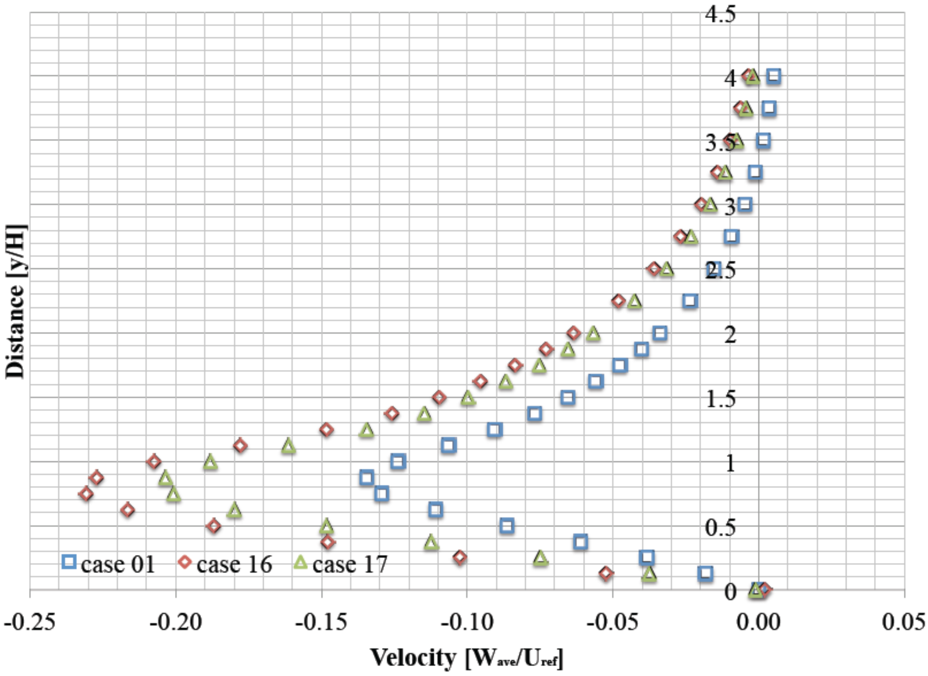

Figure 6.9: Standard deviation of along wind velocity profile at x/H = 1.5

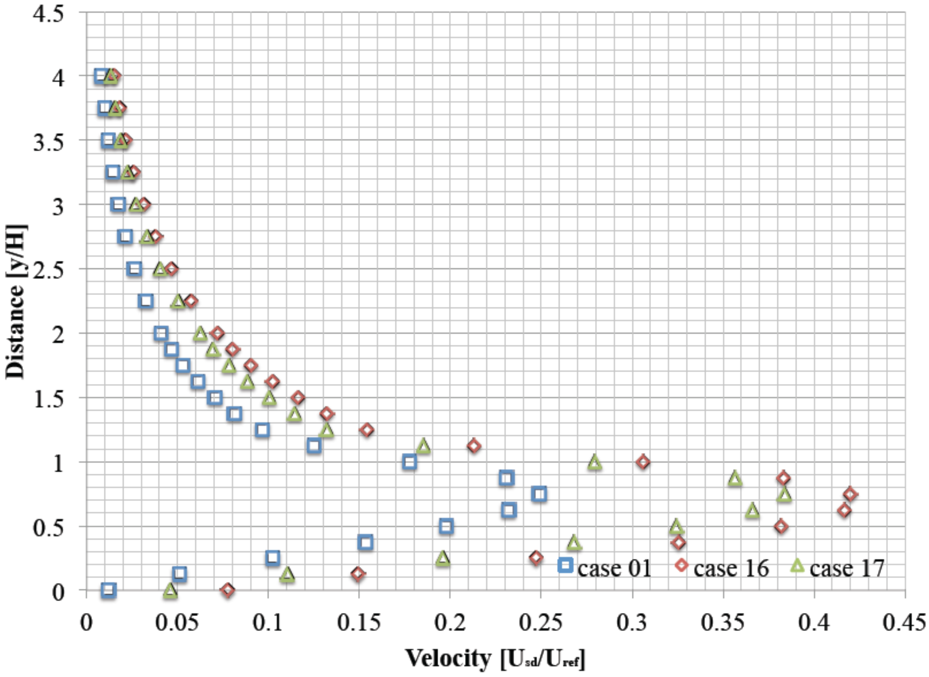

The time-averaged residual kinetic energy of the velocity fluctuations, k_{ave}, profile along the domain centerline is shown in Figure 6.10 for cases 01, 16 and 17. A distinctive peak in the residual kinetic energy, k_{ave}/U_{ref}^2, is visible at a distance of 2.5H from the rear face for cases 16 and 17. For case 01, the peak is substantially lower and less distinctive.

It appears that the CWE simulations tend to a parameter independent solution; however, it is not possible to identify the simulation parameters responsible. The fractional factorial design approach makes it possible to distinguish between the influences of different simulation parameters considered in the analysis on the solution.

Figure 6.10: Time-averaged residual kinetic energy along the centerline

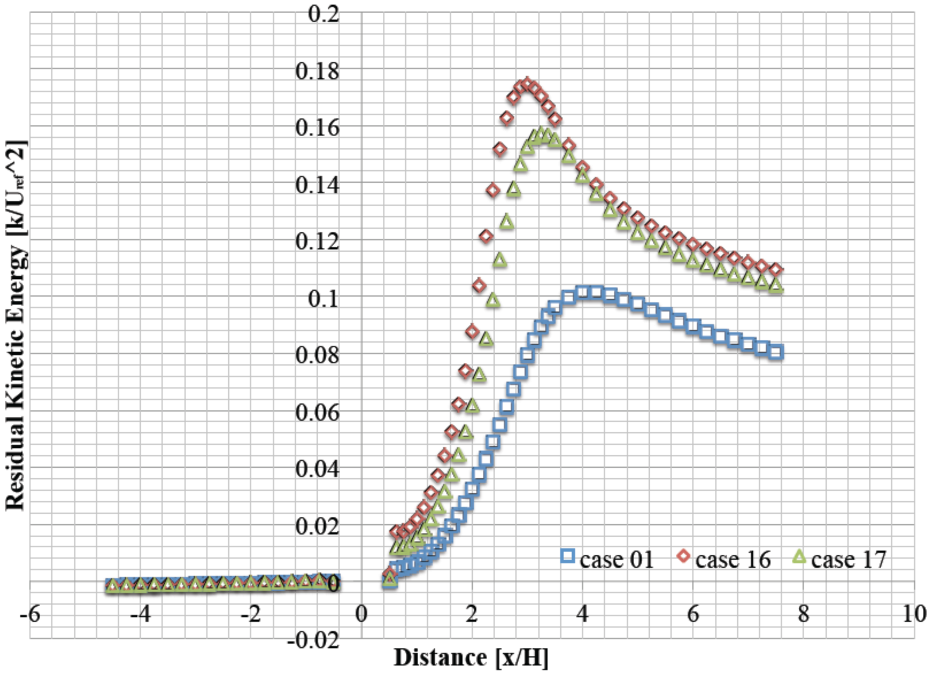

6.3.2 *Fractional Factorial Design*

In factorial design, different input parameters are evaluated over a range of values. The values of the input parameters are configured in each of the experiments to take advantage of orthogonality such that none of the experiments is a linear combination of another. This condition allows the determination of the main effects of a parameter or the interaction effects of multiple parameters using common sense and simple arithmetic.

It is unnecessary to consider all the results to discriminate between the different simulations. Instead, it is more efficient to interpret the results of a few key identities that define the critical elements of the flow. In total, 11 experimental identities are considered in this study as shown in Figure 6.11. The variables related to the velocity field are listed in Table 6.1.

The highest negative velocity (P5) and size of the recirculation zone (P6 where $u_{ave} = 0$) are important as they measure the size and strength of the base region while the downstream velocity (P7) is instructive in terms of the flow recovery downstream in the wake flow region.

Figure 6.11: Position of Identities within Computational Domain

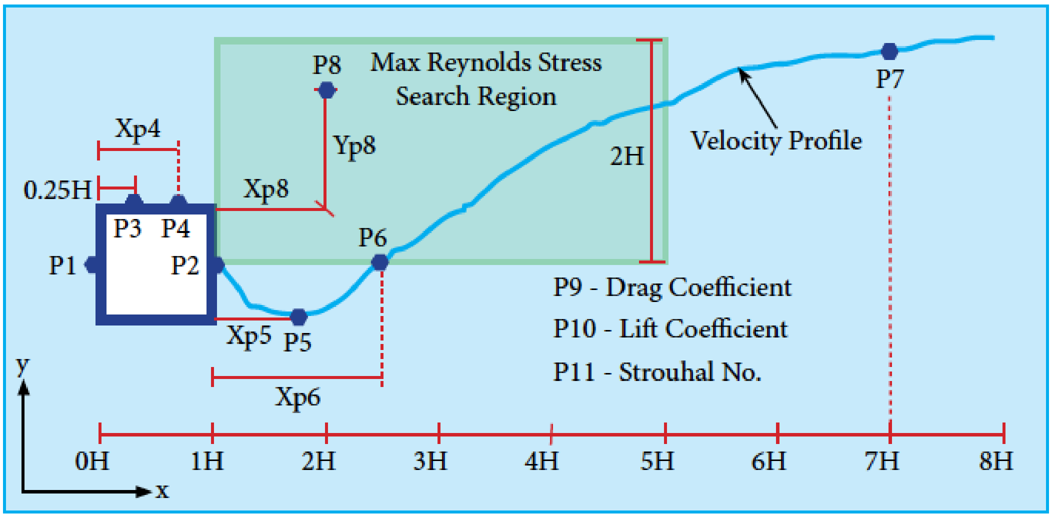

The results of the velocity related variables are summarized in Table 6.2 below. The variable average, main effects and interaction effects are calculated in accordance with the contrast of coefficients method. This involves combining the results of all the simulations for that particular variable in accordance with the appropriate sign convention and dividing the result by the relevant divisor given in Table 6.3 below. The averages, main effects and interaction effects calculated using

Table 6.1: List of Velocity Related Variables

Identity	Description	Variable	Comment
P5	Min velocity in recirculation zone	X_{p5}	Distance from back face to min velocity along centerline
		$u_{5,ave}$	Min average velocity
		$u_5{}'_{rms}$	RMS velocity fluctuations
P6	Size of recirculation zone	X_{p6}	Length of recirculation zone from back face
		$u_{6,ave}$	Average velocity at measurement point
		$u_6{}'_{,rms}$	RMS velocity fluctuations at measurement point
P7	Downstream velocity	$u_{7,ave}$	Average velocity at 7H from origin
		$u_7{}'_{,rms}$	RMS velocity fluctuations

the contrast of coefficients for the velocity related variables are given in Table 6.4 below.

Table 6.2: Summary of Results of Velocity Related Variables

Case	P5 Min. Velocity in Body Wake			P6 Recirculation Zone Size			P7 Downstream Velocity	
	Dist.	$u_{5,ave}$	$u_5'_{,rms}$	Length	$u_{6,ave}$	$u_6'_{,rms}$	$u_{7,ave}$	$u_7'_{,rms}$
	[-]	[-]	[-]	[-]	[-]	[-]	[-]	[-]
01	1.010	-0.178	0.012	2.129	0.003	0.031	0.746	0.063
02	0.886	-0.198	0.041	1.632	-0.014	0.090	0.849	0.019
03	1.010	-0.178	0.012	2.129	-0.016	0.024	0.746	0.063
04	0.886	-0.202	0.039	1.756	0.021	0.099	0.835	0.024
05	1.010	-0.167	0.013	2.005	0.001	0.032	0.718	0.061
06	0.762	-0.178	0.045	1.507	0.020	0.099	0.785	0.020
07	1.010	-0.166	0.013	2.005	-0.012	0.027	0.701	0.059
08	0.886	-0.188	0.043	1.632	0.019	0.094	0.794	0.026
09	1.010	-0.179	0.011	2.129	-0.007	0.028	0.760	0.067
10	0.886	-0.200	0.038	1.756	0.030	0.096	0.867	0.020
11	1.010	-0.178	0.011	2.253	0.018	0.030	0.758	0.065
12	1.010	-0.205	0.038	1.756	-0.025	0.082	0.854	0.030
13	1.010	-0.166	0.013	2.005	-0.001	0.031	0.722	0.063
14	0.762	-0.185	0.038	1.507	-0.027	0.082	0.821	0.023
15	1.010	-0.168	0.012	2.129	0.017	0.032	0.726	0.063
16	0.886	-0.189	0.042	1.632	0.01	0.09	0.805	0.028
17	0.886	-0.187	0.028	1.756	-0.018	0.066	0.791	0.038

Interpreting the results reveals that the minimum time-averaged velocity in the recirculation zone (P5) is on average 0.94H from the rear of the square cylinder. The most influential factor is the mesh refinement. Using the finest mesh rather than a coarse mesh can reduce the distance by an average 0.14H. This result is also shown graphically in Figure 6.12, where the distance reduces from ~1.010H to ~0.870H. However, the advantage of the graphical approach is that it includes the target value.

Table 6.3: Example of Calculation of Average, Main Effects and Interaction Effects using Contrast of Coefficients Method

Case	Average	Main Effects					Interaction Effects									
		1	2	3	4	5	12	13	14	15	23	24	25	34	35	45
01	+	-	-	-	-	+	+	+	+	-	+	+	-	+	-	-
02	+	+	-	-	-	-	-	-	-	-	+	+	+	+	+	+
03	+	-	+	-	-	-	-	+	+	+	-	-	-	+	+	+
04	+	+	+	-	-	+	+	-	-	+	-	-	+	+	-	-
05	+	-	-	+	-	-	+	-	+	+	-	+	+	-	-	+
06	+	+	-	+	-	+	-	+	-	+	-	+	-	-	+	-
07	+	-	+	+	-	+	-	-	+	-	+	-	+	-	+	-
08	+	+	+	+	-	-	+	+	-	-	+	-	-	-	-	+
09	+	-	-	-	+	-	+	+	-	+	+	-	+	-	+	-
10	+	+	-	-	+	+	-	-	+	+	+	-	-	-	-	+
11	+	-	+	-	+	+	-	+	-	-	-	+	+	-	-	+
12	+	+	+	-	+	-	+	-	+	-	-	+	-	-	+	-
13	+	-	-	+	+	+	+	-	-	-	-	-	-	+	+	+
14	+	+	-	+	+	-	-	+	+	-	-	-	+	+	-	-
15	+	-	+	+	+	-	-	-	-	+	+	+	-	+	-	-
16	+	+	+	+	+	+	+	+	+	+	+	+	+	+	+	+
Divisor	16	8	8	8	8	8	8	8	8	8	8	8	8	8	8	8
$u_{7,ave}$	0.780	**0.092**	-0.006	**-0.043**	**0.017**	-0.006	-0.002	-0.007	0.004	0.000	0.001	-0.001	0.001	0.002	-0.005	0.004

Table 6.4: Average, Main Effects and Interaction Effects for Velocity Related Variables using Contrast of Coefficients Method

Identity / Variable		Ave.	Main Effects					Interaction Effects									
			Grid Mesh	Time-step	Domain												
					Upstream	Downstream	Cross-stream										
			1	2	3	4	5	12	13	14	15	23	24	25	34	35	45
5	Dist.	0.940	**-0.140**	0.047	-0.047	0.015	-0.016	0.047	-0.047	0.016	-0.015	0.016	0.015	-0.015	-0.016	0.016	0.016
5	$u_{5.ave}$	-0.183	**-0.021**	-0.003	**0.014**	-0.002	0.001	-0.003	0.002	-0.001	0.000	-0.001	0.000	0.000	0.000	0.001	0.000
5	$u_{5,rms}$	0.026	**0.028**	0.000	0.002	-0.002	0.001	0.000	0.001	-0.001	0.000	0.000	0.001	-0.001	0.000	0.001	0.001
6	Length	1.873	**-0.451**	**0.078**	**-0.140**	0.047	0.016	0.016	-0.016	-0.016	0.015	0.016	0.016	-0.016	-0.015	-0.047	0.016
6	$u_{6.ave}$	0.002	0.004	0.003	0.002	-0.001	0.018	0.001	0.000	**-0.014**	**0.014**	0.007	0.003	-0.007	-0.006	**-0.016**	0.007
6	$u_{6,rms}$	0.060	**0.062**	-0.001	0.001	-0.003	0.005	0.001	-0.001	-0.005	0.004	0.001	0.001	-0.001	-0.001	-0.003	0.001
7	$u_{7,ave}$	0.780	**0.092**	-0.006	**-0.043**	**0.017**	-0.006	-0.002	-0.007	0.004	0.000	0.001	-0.001	0.001	0.002	-0.005	0.004
7	$u_7'{}_{,rms}$	0.043	**-0.039**	0.003	-0.001	0.003	-0.001	0.004	0.002	0.000	0.000	-0.001	0.001	0.000	0.000	0.001	0.000

Given that the target value is much closer to the finest mesh (~0.89H) gives some indication that the model is converging with refinement.

Figure 6.12: Distance to Time-averaged Minimum Velocity in Body Wake

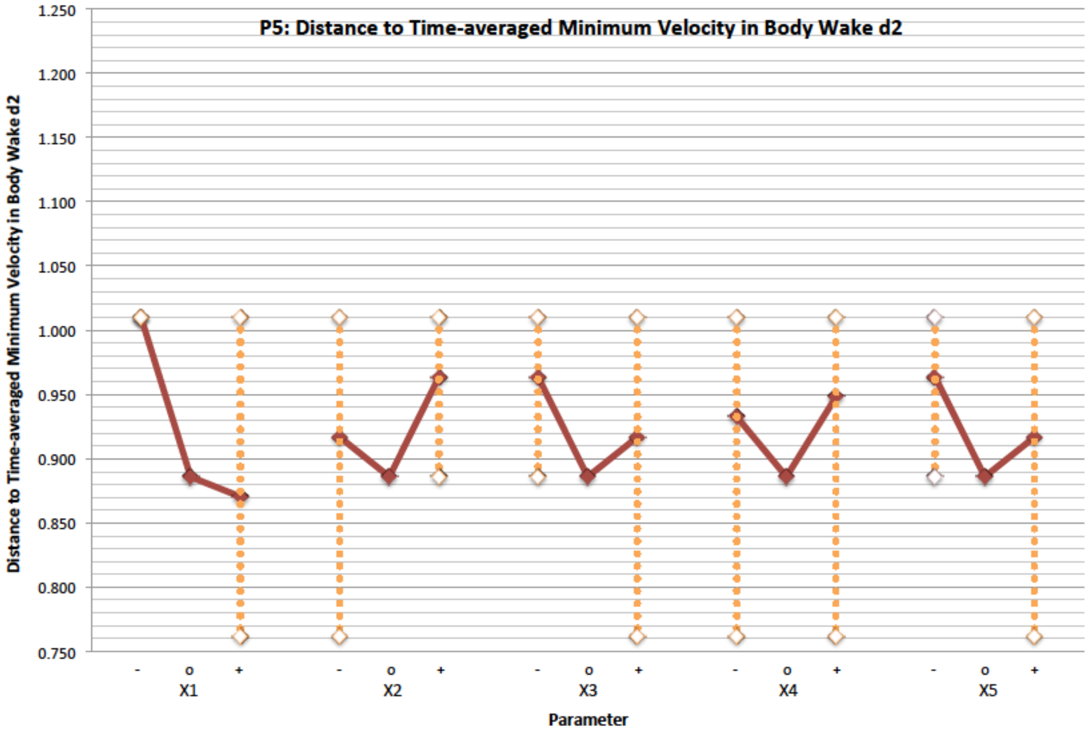

In contrast to the numerical approach of the contrast of coefficients method, the graphical approach would suggest that the other parameters have some impact on the solution. It appears that increasing upstream length (x3) and the cross-stream half-width (x5) leads to a reduction in the distance to minimum velocity. Moreover, the result on the finest mesh is close to the target mesh for both parameters, which might indicate a tendency towards convergence. However, the distance is greater on the finer mesh than the intermediate mesh for both parameters. It should be noted that the velocity field was sampled at discrete locations. The distance estimated from a single simulation for the target case, while the distance is taken as the average of a series of simulations for the coarse and fine cases. Therefore, this alone could account for this inconsistent behavior. One possible remedy would be to increase the density of sampling points.

Although it is arguable how much the downstream length impacts the distance to the minimum velocity in the wake, it appears that the time-step influences this distance. The distance increases from the coarse mesh to the finer mesh but the target value predicts a shorter distance than the other two cases. Once more, this inconsistency might be a function of the sampling point positions.

Figure 6.13: Extent of Recirculation Zone

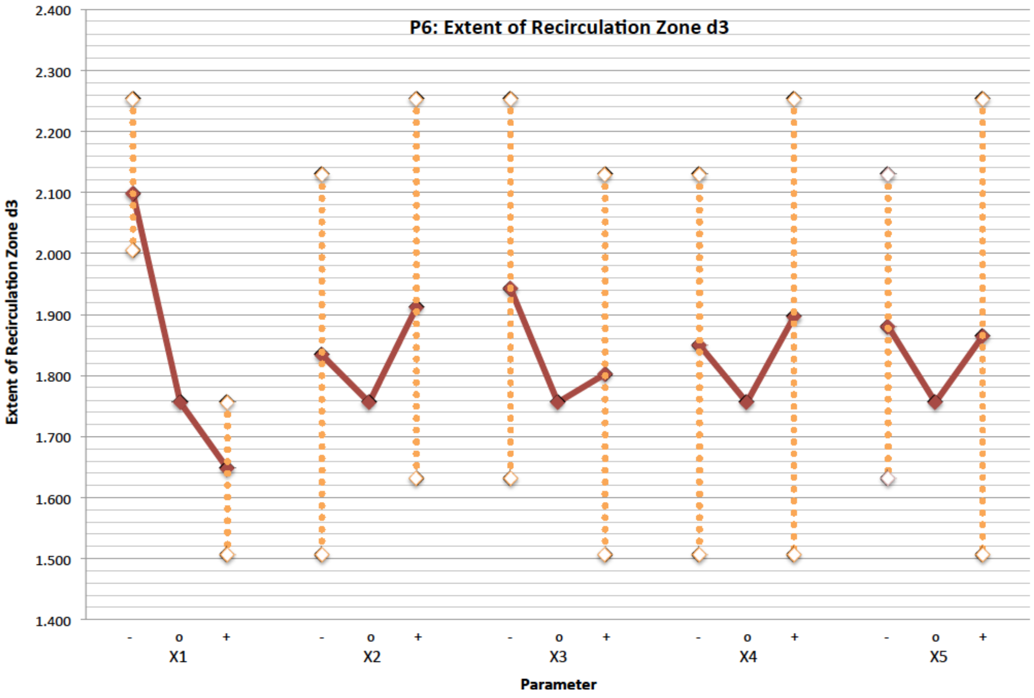

In relation the recirculation zone, its average length (P6) is estimated at 1.87H. Once more, the most dominant factor is the mesh refinement. Adopting a fine mesh instead of a coarse mesh can lead to an average reduction of 0.45H, which is consistent with the graphical representation in Figure 6.13. Moreover, the target value is close to the finer mesh, which suggests the model is tending towards grid independence. The solution is influenced by two other factors, although their effect is less pronounced. The analysis reveals that none of these parameters are dependent on each other. Increasing the upstream length can reduce the length of the recirculation zone by 0.14H on average while reducing the time-step can cause the zone to increase in size by 0.078H on average. The fluctuation in the solution for the different refinement levels of these parameters could be a result of comparing the average values with a single simulation result.

Figure 6.14: Time-averaged Downstream Velocity

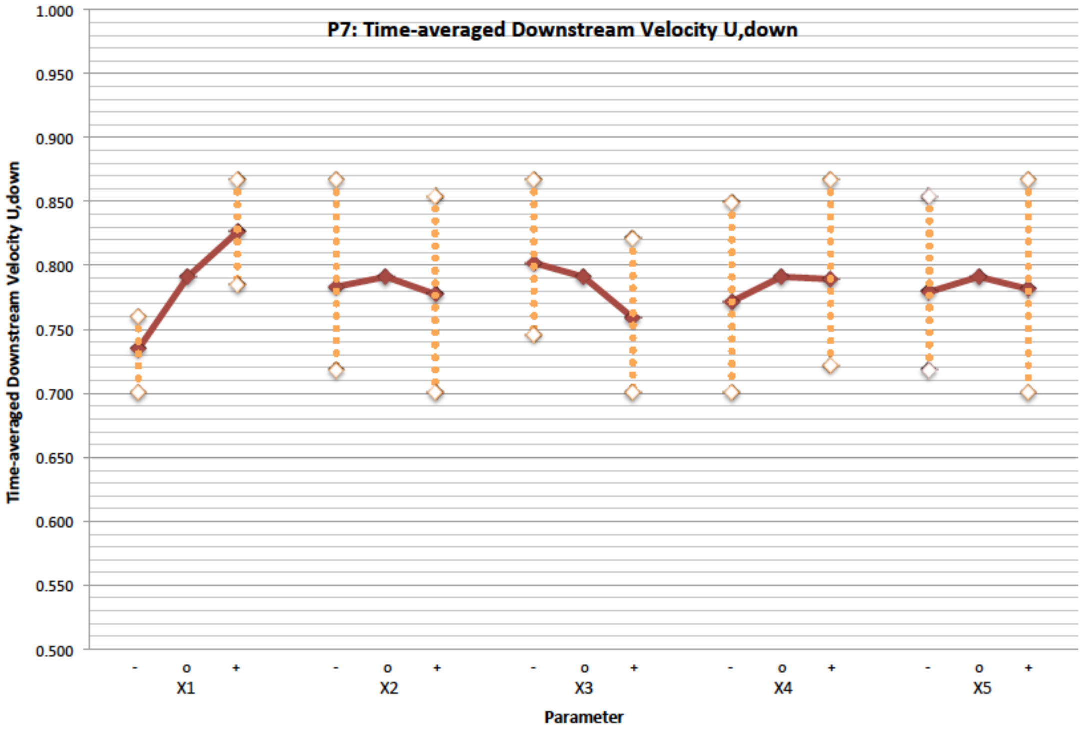

The time-averaged downstream velocity (P7), $u_{7,ave}$, averaged across all the simulations is estimated at 0.78. Three factors are identified as impacting the solution and all are adjudged to be independent from one and other. The grid refinement has the most significant influence indicated in Table 6.4 above and as shown in Figure 6.14. The refinement of the grid can result in an average increase of 0.092. Increasing the upstream length has a lesser impact as it results in a reduction of 0.043. Surprisingly, increasing the downstream length only increases the downstream velocity by 0.017 and therefore, it has a relatively minor effect.

It should be noted that for all three identities considered that the root-mean-square of the fluctuating component displays an almost exclusive dependence on mesh refinement.

6.4 Pressure

6.4.1 Time-averaged Variables

This section compares the pressure profiles of cases 01, 16 and 17. These cases facilitate comparison between the coarsest case (case 01), which has the coarsest grid, the largest time step and amongst the smallest computational domain size, with the finest case (case 16), which has the finest grid, smallest time-step and largest computational domain size. The intermediate configuration is defined in case 17, the target case.

Figure 6.15: Reference Frame for Pressure Plots

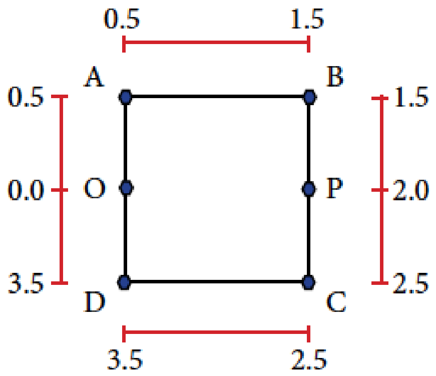

Instead of considering the entire domain, the study is only concerned with the pressure on the cylinder surfaces. The reference frame used in the pressure plots is illustrated in Figure 6.15. The origin is taken as the center of the front face of the square cylinder and the distance increases in a clockwise direction as illustrated in the figure above.

The time-averaged pressure coefficients, P_{ave}, and root-mean-square pressure coefficients, P_{rms}, acting on the cylinder surfaces for case 01, 16 and 17 are shown in Figures 6.16 and 6.17, respectively.

It is apparent from all the plots that the maximum pressure coefficient occurs at the center of the front face. For all cases, the stagnation pressure, $C_{ps,ave}$, is greater than unity. However, $C_{ps,ave}$ cannot exceed a unity by definition. The error can be explained by considering how the reference pressure is defined. The user defines the reference pressure as zero at the outlet, while OpenFOAM references the pressure at the inlet. A pressure gradient is required to drive the flow around the square cylinder and across the domain and therefore, the pressure differs between the inlet and the outlet. Furthermore, this pressure difference is domain dependent and difficult to assess a priori. The advantage of taking the reference pressure at the outlet rather than the inlet allows for some quantification of this error. It can be seen that stagnation pressure approaches unity as the refinement of the model increases; however, it is not possible to identify the simulation parameters responsible.

Figure 6.16: Time-averaged pressure coefficient on cylinder surfaces

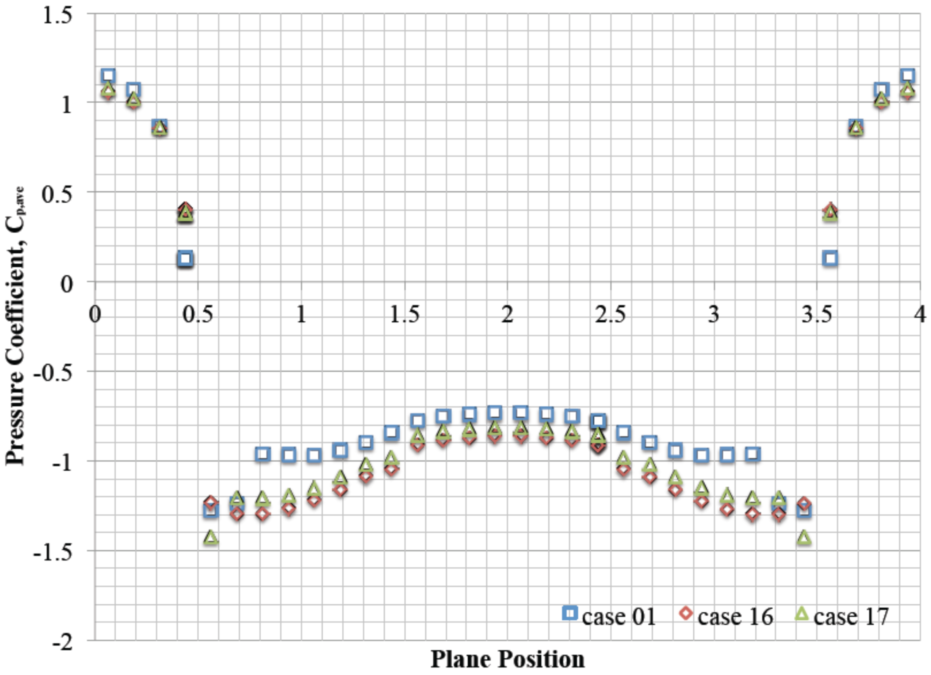

Inspection of the pressure profiles reveals that the pressure distribution is intuitively correct. The front face experiences a positive pressure as a result of encountering the oncoming flow. The maximum pressure occurs at the center and it reduces towards the corners (i.e. from 0H to 0.5H or 4.0H to 3.5H). The remaining three sides are subject to negative pressure as a result of flow separation that occurs at the front corners (i.e. 0.5H or 3.5H). The maximum negative pressure occurs near the separation point. Due to the presence of a wake at the rear of the cylinder, the pressure distribution is relatively uniform on the rear face (i.e. 1.5H to 2.5H). The pressure distributions for cases 16 and 17 are quite similar when compared with case 01. The notable differences in the pressure distributions occur near the front corners of the cylinder. In the finest case (case 16), the side face has a smooth pressure distribution. In the other cases, the pressure distribution displays significant pressure peaks near the front corner. Although there is a clear improvement in the solution as the model is refined, it is not possible to identify the parameters responsible.

Figure 6.17: Root-mean-square pressure coefficient on cylinder surfaces

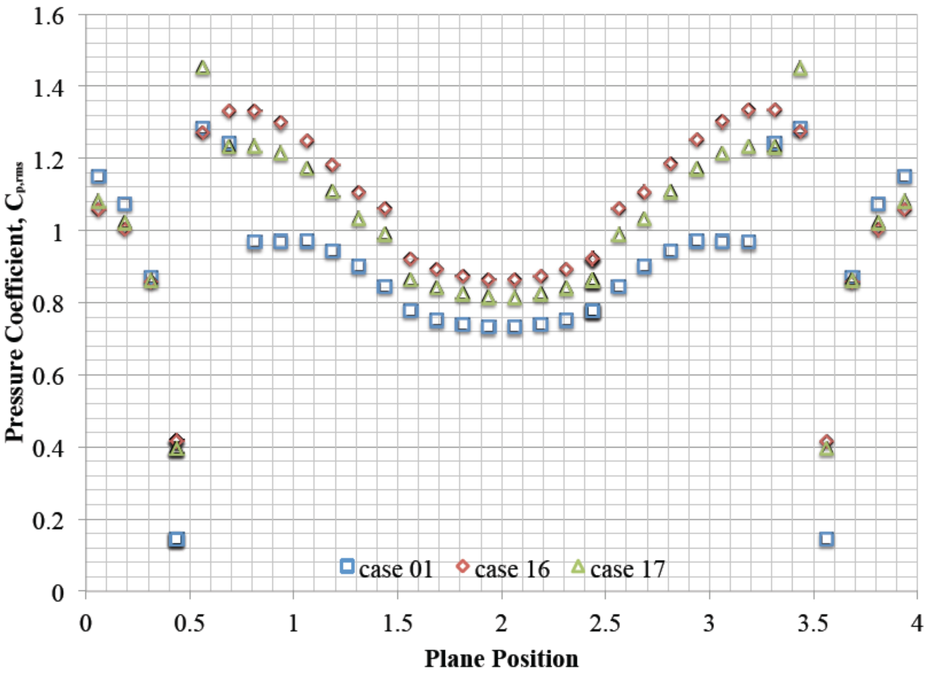

The fractional factorial design approach makes it possible to distinguish between the influences of different simulation parameters considered in the analysis on the solution.

6.4.2 Fractional Factorial Design

A few key identities have been selected to define the critical elements of the flow. The relevant pressure variables are listed in Table 6.5 below. Their location within the computational domain is illustrated in Figure 6.11.

The stagnation pressure (P1) is key identity due to its relationship to the positive upstream pressure that accelerates the flow around the body and the drag force acting on the body. In addition, the stagnation can be useful in quantifying the pressure difference between the inlet and the outlet.

The base pressure (P2) is a key variable, as not only is it a measure of the pressure in the wake but it also provides information on the vortices shed from the body. Both the strength of vortices and the distance to the formation of the vortex are related to the base pressure (Bearman and Trueman, 1972).

The inspection of the pressure plots above revealed that the pressure distribution near the front corners was very sensitive to the refinement of the model. Therefore, it was considered appropriate to examine the pressure on the top face at a distance 0.25H from the front corner (P3).

Another key identity is the maximum average pressure on the top face. This pressure is indicative of the recirculation zone on the side face. In addition, it is related to the lift acting on cylinder.

The results of the velocity related variables are summarized in Table 6.6 below. The variable average, main effects and interaction effects is calculated in accordance with the contrast of coefficients method. The averages, main effects and interaction for the pressure variables are given in Table 6.7 below.

Interpreting the results reveals that the time-averaged stagnation pressure coefficient (P1), $C_{ps,ave}$, is estimated at 1.12 on average. The over-prediction of the

Table 6.5: List of Pressure Related Variables

Identity	Description	Variable	Comment
P1	Stagnation pressure	$C_{ps,ave}$	Average pressure coefficient
		$C_{ps}'_{,rms}$	RMS pressure coefficient fluctuations
P2	Base pressure	$C_{pb,ave}$	Average pressure coefficient
		$C_{pb}'_{,rms}$	RMS pressure coefficient fluctuations
P3	Pressure on top face at 0.25H from front corner	$C_{p3,ave}$	Average pressure coefficient
		$C_{p3}'_{,rms}$	RMS pressure coefficient fluctuations
P4	Max pressure on top face	X_{p4}	Distance from front corner
		$C_{p4,ave}$	Max average pressure coefficient
		$C_{p4}'_{,rms}$	RMS pressure coefficient fluctuations

Table 6.6: Summary of Results of Pressure Related Variables

Case	P1 Stagnation Pressure		P2 Base Pressure		P3 Pressure at 0.25H		P4 Max. Pressure on Top Face		
	$C_{ps,ave}$	$C'_{ps,rms}$	$C_{pb,ave}$	$C'_{pb,rms}$	$C_{p3,ave}$	$C'_{p3,rms}$	Dist.	$C_{p4,ave}$	$C'_{p4,rms}$
	[-]	[-]	[-]	[-]	[-]	[-]	[-]	[-]	[-]
01	1.150	0.006	-0.732	0.016	-1.100	0.112	0.062	-1.277	0.129
02	1.216	0.015	-0.877	0.042	-1.363	0.329	0.188	-1.368	0.333
03	1.167	0.007	-0.721	0.016	-1.079	0.104	0.062	-1.325	0.123
04	1.198	0.010	-0.885	0.036	-1.343	0.311	0.188	-1.344	0.314
05	1.062	0.007	-0.685	0.018	-1.039	0.121	0.062	-1.216	0.135
06	1.070	0.011	-0.846	0.047	-1.302	0.349	0.188	-1.307	0.352
07	1.036	0.005	-0.681	0.016	-1.015	0.115	0.062	-1.248	0.134
08	1.112	0.012	-0.830	0.040	-1.268	0.319	0.188	-1.269	0.322
09	1.139	0.004	-0.739	0.013	-1.123	0.107	0.188	-1.257	0.117
10	1.180	0.008	-0.913	0.031	-1.403	0.319	0.188	-1.409	0.322
11	1.150	0.003	-0.740	0.012	-1.098	0.102	0.062	-1.345	0.121
12	1.194	0.008	-0.887	0.028	-1.345	0.292	0.188	-1.345	0.295
13	1.023	0.004	-0.702	0.014	-1.051	0.119	0.062	-1.226	0.133
14	1.097	0.008	-0.854	0.034	-1.319	0.331	0.188	-1.324	0.335
15	1.062	0.004	-0.691	0.013	-1.033	0.111	0.062	-1.272	0.129
16	1.058	0.008	-0.862	0.033	-1.294	0.311	0.188	-1.295	0.314
17	1.082	0.007	-0.814	0.025	-1.207	0.254	0.062	-1.425	0.279

stagnation pressure is related to the pressure gradient across the domain, it is unsurprising that the upstream length is the most dominant parameter and that increasing the upstream length to 15H can reduce this discrepancy by as much as 0.11.

The graphical plot, Figure 6.18, reveals that the results of the target (case 17) and maximum upstream lengths (case 16) are close and thus, this suggests that the model approaches parametric independence.

Table 6.7: Average, Main Effects and Interaction Effects for Pressure Related Variables using Contrast of Coefficients Method

Identity / Variable		**Ave.**	**Main Effects**					**Interaction Effects**									
			Grid Mesh	Time-step	Domain												
					Upstream	Downstream	Cross-stream										
			1	2	3	4	5	12	13	14	15	23	24	25	34	35	45
1	$C_{ps,ave}$	1.120	**0.042**	0.005	**-0.109**	-0.014	**-0.023**	-0.005	-0.003	-0.003	-0.005	-0.001	0.001	0.000	0.003	-0.014	0.003
1	$C_{ps}'{}_{,rms}$	0.008	**0.005**	-0.001	0.000	**-0.003**	-0.001	0.000	0.000	-0.001	0.000	0.001	0.001	0.000	0.001	0.001	0.001
2	$C_{pb,ave}$	-0.790	**-0.158**	0.006	**0.043**	**-0.016**	**-0.010**	0.000	0.000	-0.003	-0.005	-0.001	0.001	0.000	0.000	0.002	-0.002
2	$C_{pb}'{}_{,rms}$	0.026	**0.022**	-0.003	0.003	**-0.007**	0.000	-0.002	0.002	-0.003	0.001	0.000	0.001	0.000	0.000	0.001	0.000
3	$C_{p3,ave}$	-1.198	**-0.262**	**0.028**	**0.067**	**-0.020**	-0.005	0.006	0.001	-0.002	-0.007	-0.003	0.003	-0.002	0.001	0.004	-0.002
3	$C_{p3}'{}_{,rms}$	0.216	**0.209**	**-0.015**	**0.013**	-0.008	0.003	-0.009	0.002	-0.005	0.002	-0.001	0.000	0.000	0.001	0.000	0.000
4	Dist.	0.133	**0.110**	-0.016	-0.016	0.016	-0.016	0.016	0.016	-0.016	0.016	0.016	-0.016	0.016	-0.016	0.016	-0.016
4	$C_{p4,ave}$	-1.302	-0.062	-0.007	**0.064**	-0.015	-0.009	**0.046**	0.004	-0.006	-0.003	0.005	-0.003	0.004	-0.004	0.011	-0.010
4	$C_{p4}'{}_{,rms}$	0.226	**0.196**	-0.013	0.013	-0.010	0.004	-0.011	0.002	-0.004	0.000	-0.001	0.001	0.000	0.002	-0.001	0.000

Figure 6.18: Time-averaged Stagnation Pressure Coefficient

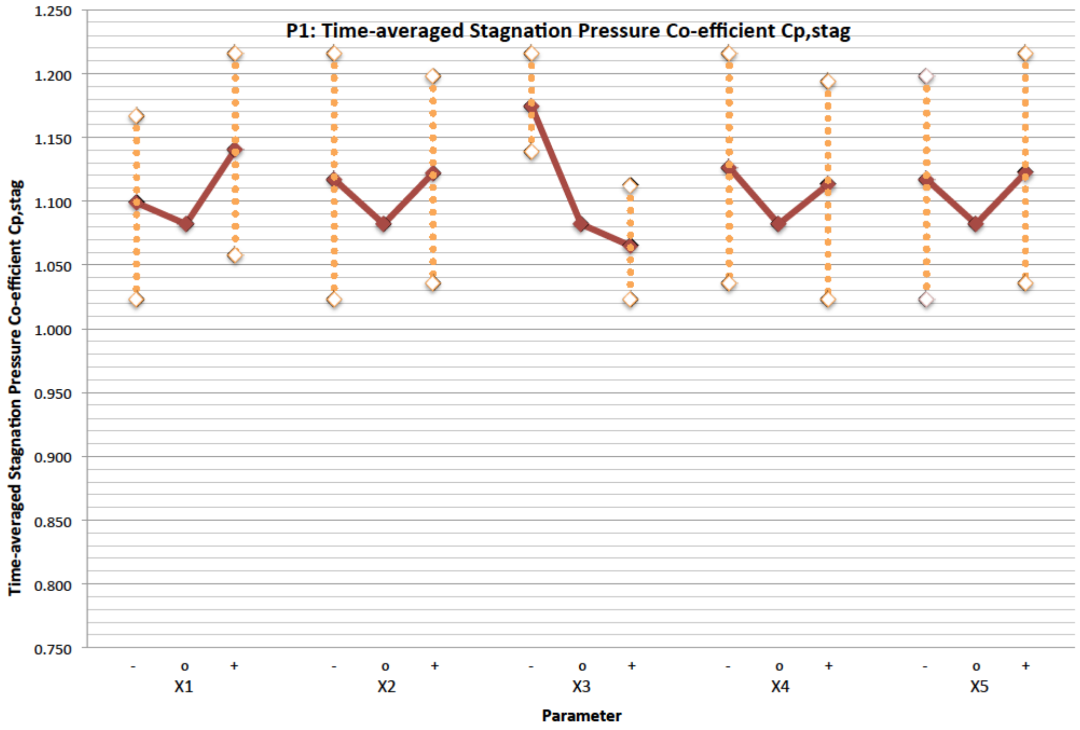

The upstream length is not the only parameter to influence the stagnation pressure, although there are no dependencies between parameters. The contrast of coefficients method and the graphical representation indicate that the grid refinement has a lesser impact and acts to increase the stagnation pressure, which is understandable as a finer grid will allow better approximation of peaks in pressure field. However, the target value is less than both the coarse and fine mesh results. This is a counter-intuitive result, as the solution appears to diverge with further refinement. Moreover, there is no evidence to support any interaction with any other parameters. The fluctuation in the solution depending on the level of refinement may indicate inconsistency in the model.

In addition, the contrast of coefficients method suggest that the cross-stream half-width may influence the estimate of stagnation pressure. However, this is not apparent in the graphical plot.

The base pressure (P2), $C_{pb,ave}$, is predicted at -0.79 on average. It could be argued that all the simulation parameters influence the $C_{pb,ave}$ independently. It is difficult to distinguish the influence of the time-step from the background noise, however, inspection of the contrast of coefficients method and graphical plot, Figure 6.19, would suggest that the other parameters have at least a minor impact on the result. The most dominant factor is the grid refinement. This could be related to better approximation of pressure peaks on a finer grid. Refining the grid can result in a 0.158 reduction in pressure. The plot reveals that the target value (case 17) between the coarse case (case 01) the refined value (case 16), which suggests that the solution does not tend to converge.

Figure 6.19: Time-averaged Base Pressure Coefficient

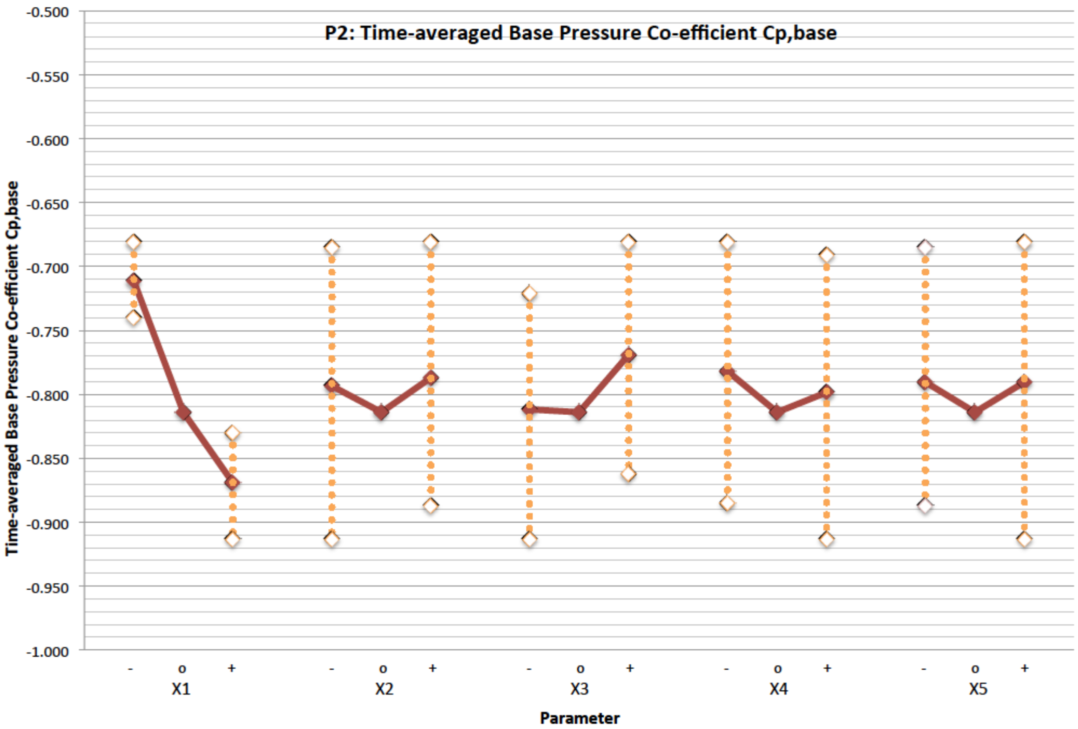

The increasing the downstream length and cross-stream half-width causes a slight reduction in base pressure but the impact is negligible in comparison to grid refinement. The upstream length has a minor impact and it acts to increase the base pressure. It is apparent from the graphical representation that the impact is most notable between the target and refined values (cases 16 and 17). However, this result is counter-intuitive too, as the solution appears to diverge with further refinement and at the same time, there is no evidence of interaction between simulation parameters.

In the case of the pressure on the top face at 0.25H from the front corner (P3), the grid refinement, time-step, upstream and downstream length are influence the time-averaged pressure coefficient, $C_{p3,ave}$, independently without any dependence between these parameters. The $C_{p3,ave}$ is estimate at -1.198 on average. The most significant parameter is the grid refinement and it can cause a reduction of 0.262 in pressure. However, it would appear from Figure 6.20 that further grid refinement is required to achieve a convergent solution, as the target value is almost equidistant between the lower and upper bound solutions.

Figure 6.20: Time-averaged Pressure Co-efficient at 0.25H behind Front Corner

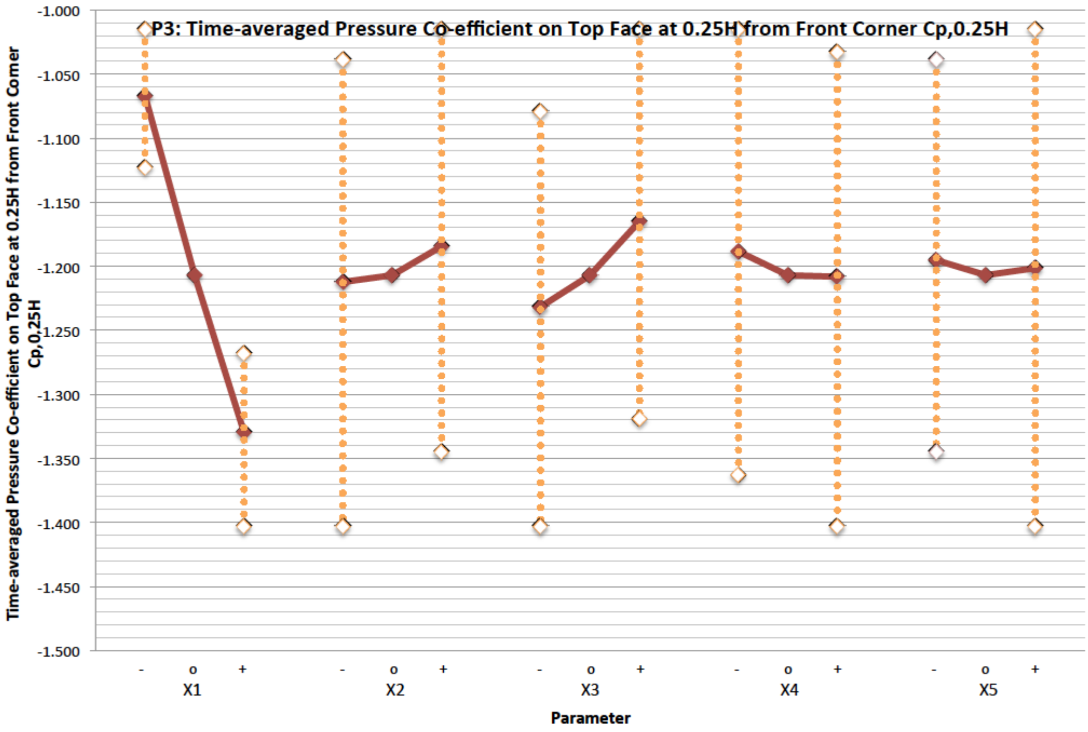

The upstream length has a minor impact on the solution as increasing its length causes a 0.067 increase in pressure. The graphical plot indicates the target value is situated closer to the minimum rather than the maximum, which would indicate that the solution is not converging. The impact of the time-step and downstream length are comparatively small resulting a 0.028 pressure increase and 0.020 pressure reduction, respectively.

The distance to the point of maximum time-averaged pressure, which is estimated at 0.226H on average, appears to be entirely dependent upon the mesh refinement as indicated in Table 6.7 and as shown in Figure 6.21 below. Refining the mesh can result in a 0.110H increase in distance from the front corner. This might possibly be attributed to a better approximation of the pressure peak on the more refined grid. It should be noted that the pressure field was sampled at discrete locations. Similar to the earlier measurements of distance, the target value is based on a single simulation while the other values are derived from multiple simulations. Therefore, this could account for the fluctuations in the solutions for the different levels of refinement of each parameter.

Figure 6.21: Distance to Time-averaged Maximum Pressure Coeff on Top Face

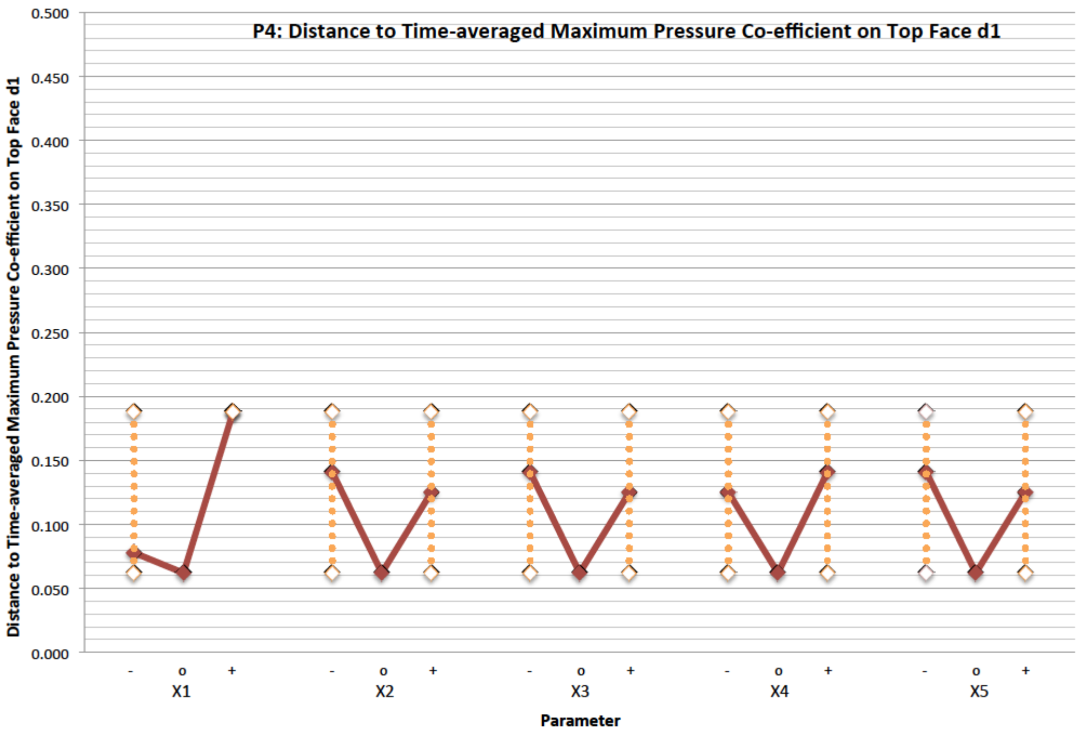

It should be noted that for all four identities considered that the root-mean-square of the fluctuating component displays an almost exclusive dependence on mesh refinement.

6.5 Drag and Lift Coefficients

6.5.1 Time-averaged Variables

Time-series plots of the drag and lift coefficients for cases 01, 16 and 17 are given in Figure 6.22.

Figure 6.22: Time series drag coefficient, C_d, and lift coefficient, C_l

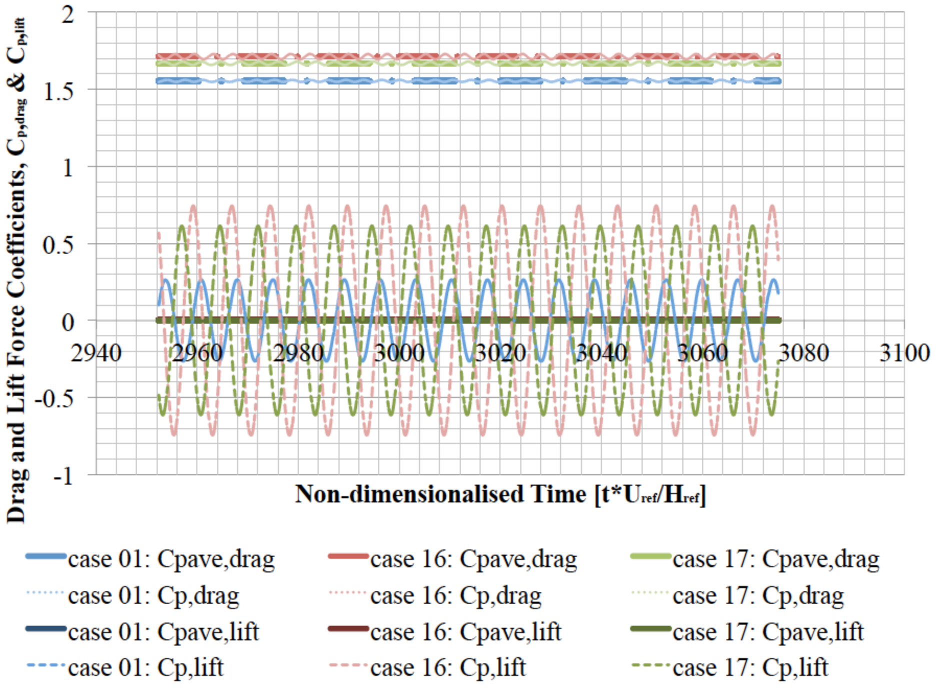

The drag co-efficient, C_d, is calculated as the difference in pressure between the front face and the rear face averaged over the entire face. Given that the pressure coefficients on the front and back vary with time so does the drag coefficient. The drag coefficient fluctuates each time a vortex is shed from the rear of the cylinder, however, the fluctuation in drag is relatively small in comparison to the total drag acting on the cylinder.

The lift coefficient, C_l, is also a time varying quantity except it is the difference in pressure between the top and bottom faces averaged over the entire face. The formation of a lower pressure recirculation zone on one side of the cylinder when compared to the other, which is associated with the formation of vortices at the rear of the body, generates lift. Instability in the flow causes the vortex formation to alternate from side to side. Hence, the magnitude of the lift coefficient oscillations is substantially greater than those associated with the drag coefficient. However, the symmetry of the section ensures that these opposite vortices are of equivalent strength and hence, these fluctuations oscillate about zero.

Figure 6.23: Spectrum of drag coefficient, C_d

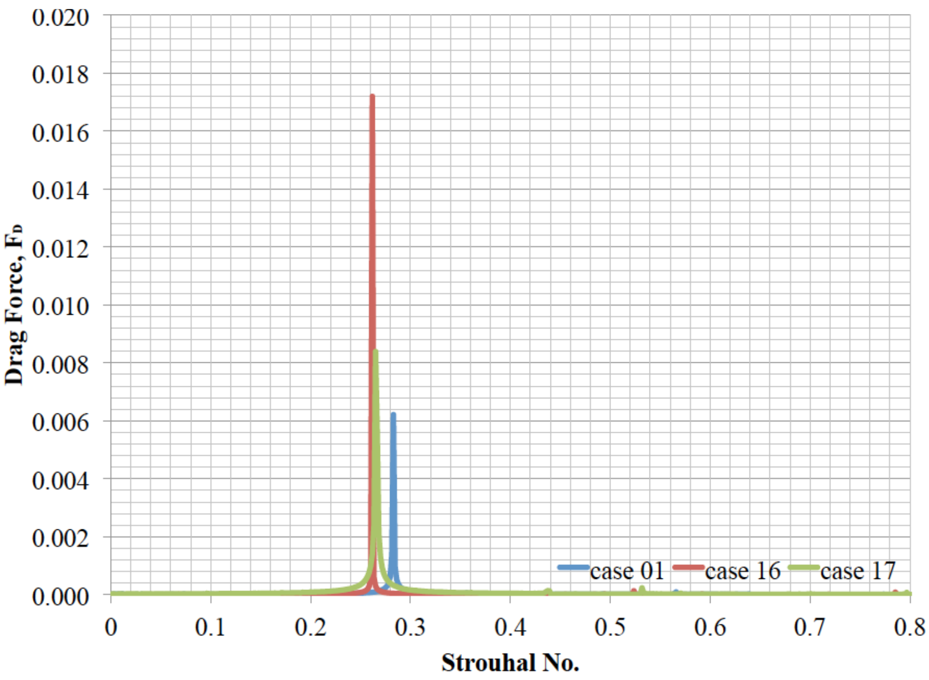

It is possible to evaluate the fluctuation frequency by taking the Fourier Fast Transform (FFT) of the time-series response. Given that the fluctuations in drag are related to each vortex shed rather than each alternate vortex shed, as is the case for the lift coefficient, the drag fluctuations have twice the frequency of the oscillations in lift. The non-dimensionalized fluctuation frequency is known as the Strouhal number. The response spectrum can be transformed into the Strouhal number by multiplying the frequency by the characteristic length, H, and dividing by the freestream velocity, U_∞. The Strouhal number associated with drag and lift are given in Figures 6.23 and 6.24 for case 01, 16 and 17, respectively.

Figure 6.24: Spectrum of lift coefficient, C_l

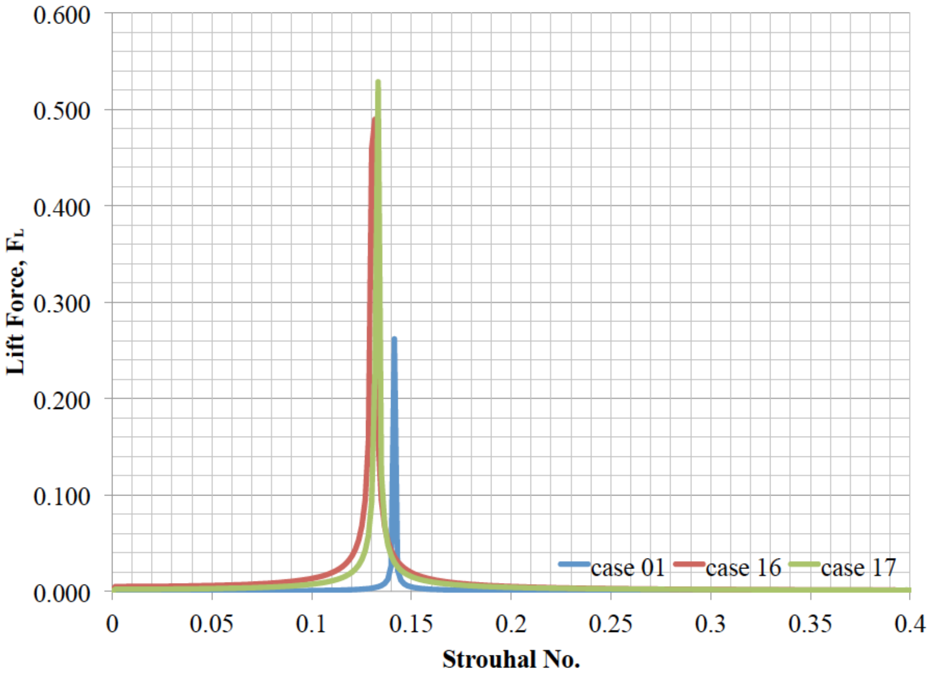

6.5.2 *Fractional Factorial Design*

A few key identities have been selected to define the critical elements of the flow. The relevant drag and lift variables are listed in Table 6.8 below. Their location within the computational domain is illustrated in Figure 6.11 above.

The drag and lift coefficients (P9 and P10) are easily related to resultant forces acting on the body. The accurate evaluation of these variables can be critical from the perspective of design. The Strouhal number (P11) is a key variable as it is a measure of the vortex shedding frequency.

The results of the velocity related variables are summarized in Table 6.9 above. The variable average, main effects and interaction effects is calculated in accordance with the contrast of coefficients method. The averages, main effects and interaction for the pressure variables are given in Table 6.10 below.

Table 6.8: List of Drag and Lift Related Variables

Identity	Description	Variable	Comment
P9	Drag Co-efficient	$C_{d,ave}$	Time-averaged drag coefficient
		$C_{d,rms}$	Root-mean-square of drag coefficient fluctuations
P10	Lift Co-efficient	$C_{l,ave}$	Time-averaged lift coefficient
		$C_{l,rms}$	Root-mean-square of lift coefficient fluctuations
P11	Lift Strouhal No.	St	

Table 6.9: Summary of Results of Drag and Lift Related Variables

Case	P9 Drag Coefficient		P10 Lift Coefficient		P11 Strouhal Number
	$C_{d,ave}$	$C_{d,rms}$	$C_{l,ave}$	$C_{l,rms}$	St
	[-]	[-]	[-]	[-]	[-]
01	1.555	0.005	0.000	0.188	0.143
02	1.868	0.013	0.002	0.562	0.136
03	1.559	0.004	0.000	0.176	0.143
04	1.856	0.013	0.001	0.529	0.136
05	1.442	0.005	-0.001	0.203	0.138
06	1.711	0.016	-0.002	0.594	0.132
07	1.418	0.005	0.000	0.196	0.135
08	1.731	0.013	0.001	0.540	0.133
09	1.535	0.004	0.004	0.176	0.143
10	1.868	0.011	-0.003	0.546	0.138
11	1.560	0.003	0.000	0.173	0.143
12	1.854	0.010	-0.001	0.498	0.136
13	1.424	0.004	0.000	0.200	0.136
14	1.743	0.012	0.002	0.566	0.133
15	1.448	0.004	0.000	0.189	0.138
16	1.712	0.012	0.003	0.527	0.133
17	1.669	0.008	-0.001	0.435	0.135

Interpreting the results reveals that the time-averaged drag coefficient (P9), $C_{d,ave}$, is estimated at 1.643 on average. The contrast of coefficients method reveals that the main effects are due to the grid refinement and the upstream length, which is consistent with Figure 6.25. This is not surprising, as these two parameters are the main factors influencing both the stagnation and base pressure coefficients. There is no interaction between the parameters. The grid refinement has a more significant impact, as reducing the mesh size results in a 0.300 increase in drag, while increasing

Table 6.10: Average, Main Effects and Interaction Effects for Drag and Lift Related Variables using Contrast of Coefficients Method

Identity / Variable		**Ave.**	**Main Effects**					**Interaction Effects**									
					Domain												
			Grid Mesh	Time-step	Upstream	Downstream	Cross-stream										
			1	2	3	4	5	12	13	14	15	23	24	25	34	35	45
9	$C_{d,ave}$	1.643	**0.300**	-0.001	**-0.128**	0.001	-0.010	-0.008	-0.009	0.002	-0.003	-0.002	0.002	-0.002	0.006	-0.015	0.006
9	$C_{d,rms}$	0.008	**0.008**	-0.001	0.001	-0.002	0.001	0.000	0.001	-0.001	0.001	0.000	0.000	0.000	0.000	0.000	-0.001
10	$C_{l,ave}$	0.000	0.000	0.000	0.000	0.001	-0.001	0.001	0.001	-0.001	0.000	0.001	-0.001	0.002	0.001	0.001	0.000
10	$C_{l,rms}$	0.366	**0.358**	**-0.026**	**0.021**	-0.014	0.005	-0.018	0.002	-0.008	0.002	-0.002	0.001	0.000	0.001	-0.001	-0.001
11	St	0.137	**-0.005**	0.000	**-0.005**	0.001	-0.001	0.000	0.001	0.000	0.001	0.000	0.000	0.000	0.000	-0.001	0.001

the upstream length reduces drag by 0.128. It is clear from the plot that there is little or no convergence between the target value (case 17) and the refined solution (case 16).

Figure 6.25: Time-averaged Drag Co-efficient

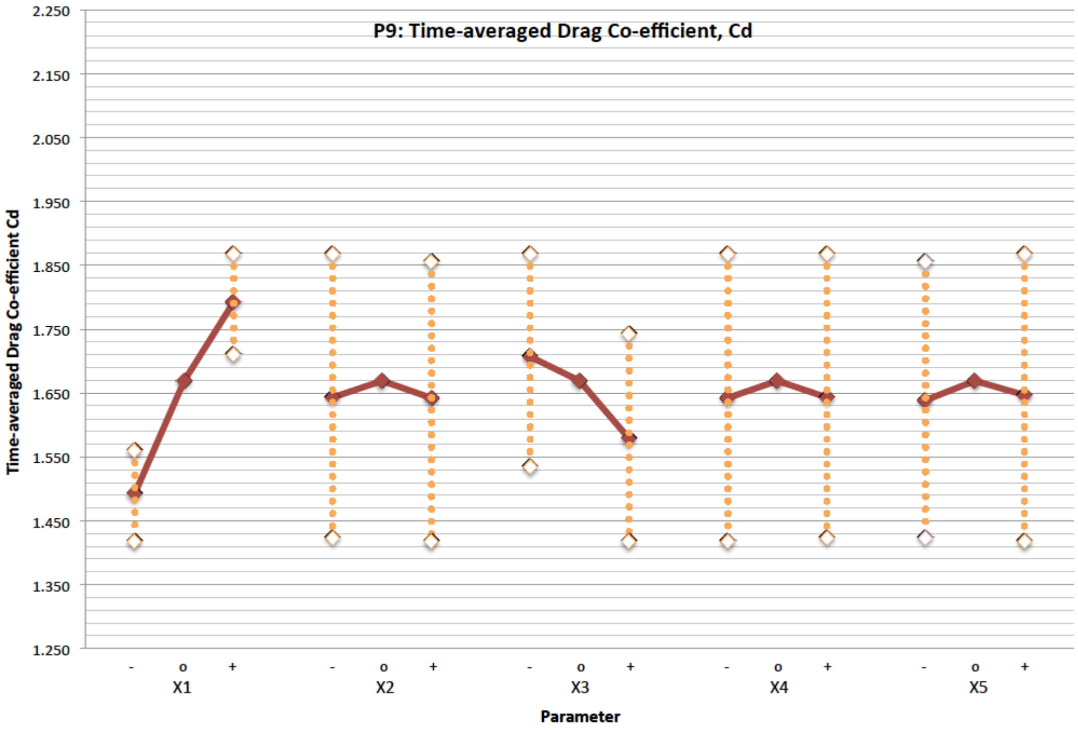

The time-averaged lift coefficient (P10), $C_{l,ave}$, is close to zero. The main effects and interactions calculated are all extremely small. Therefore, it is difficult to distinguish between effects and background noise. The root-mean-square of the fluctuating lift coefficient, $C_{l,rms}$, which is estimated at 0.366 on average, is entirely dependent upon the grid refinement. This relationship between the grid refinement and the fluctuating lift coefficient is apparent in the graphical plot shown in Figure 6.26. In this plot, there is a slight hint that the solution is converging given that the target value (case 17) is closer to the finer solution (case16).

The interpretation of the results in Table 6.10 or shown in Figure 6.27 indicates that the Strouhal number (P11), which is estimated at 0.137 on average, is dependent on two parameters, namely, the grid refinement and the upstream length.

However, it should be noted that their influence on the Strouhal number is minimal (i.e. 0.05 decrease). Therefore, the Strouhal number is insensitive to changes in the parameters investigated in this study.

Figure 6.26: RMS of Fluctuating Lift Coefficient

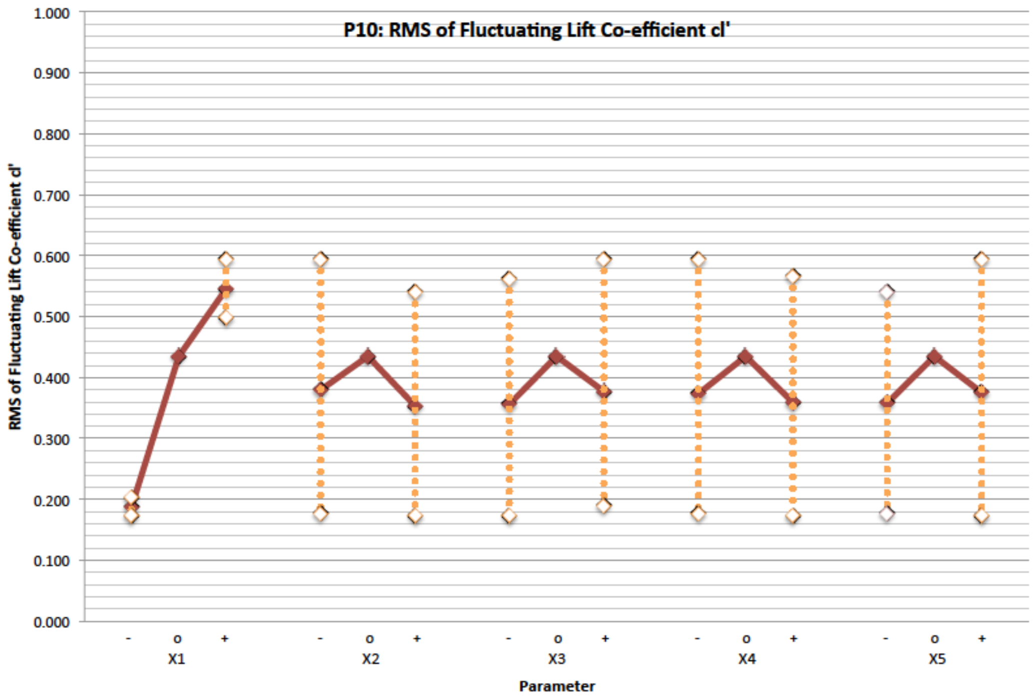

Figure 6.27: Strouhal Number

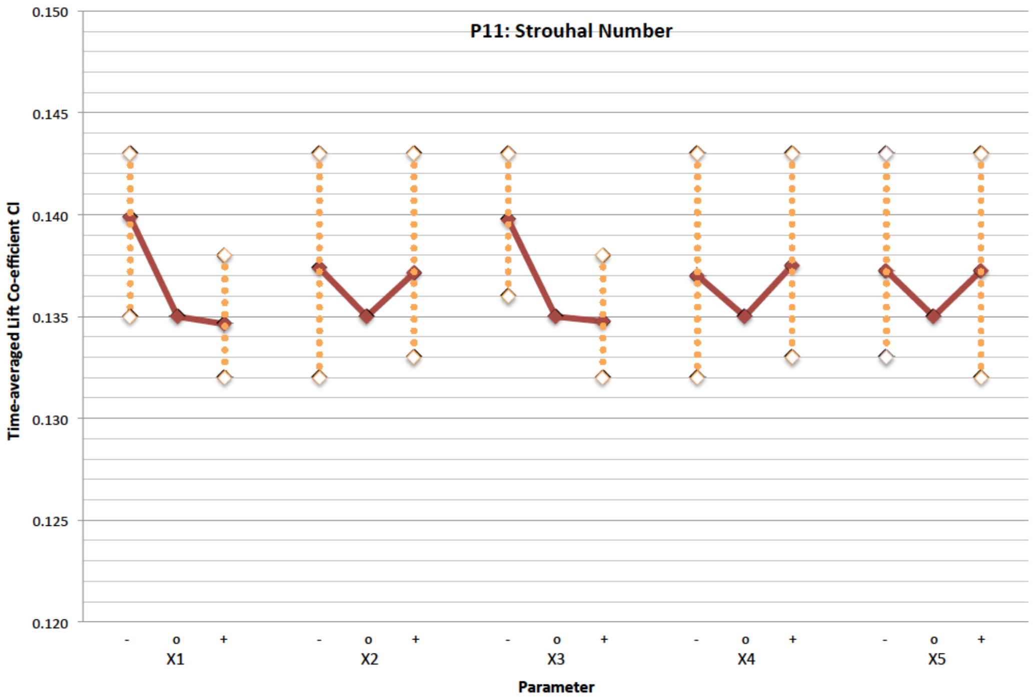

6.4 Discussion

6.4.1 Visual Inspection

From visual inspection, it would appear that the CWE model is consistent with theory.

6.4.2 Time-averaged Variables

Examination of the time-averaged and root-mean-square plots indicates that the solution converges, as the simulation parameters in the model are refined. However, this investigation has revealed errors in the model. For instance, the upstream velocity in the more refined models is slightly less than the free-stream velocity. In a similar fashion, the model over-estimates the stagnation pressure on the front face of the square cylinder. It is possible that this error difference in the definition of the reference pressure. The user prescribes a zero reference pressure at the outlet; however, OpenFOAM utilizes a higher pressure at the inlet as the reference pressure. No correction has been made to the models to account for this error as it is easy to quantify this error.

6.4.3 Fractional Factorial Design

The analysis of the results tend to suggest that different levels of refinement are required to produce an accurate pressure flow field than that required to generate an accurate velocity flow field. For instance, the velocity related variables show signs of convergence to a parameter independent solution for the finest mesh size considered in the study, while the pressure related variables remain strongly influenced by the refinement of the mesh.

In the analysis, it was not uncommon to find the target value was unbounded by the coarse and fine solutions. In the case of distance measurements, it is believed that apparent inconsistency arises from having a finite number of discrete sampling points and comparing a single simulation result with the average of a series of simulations. However, this is not necessarily the case for some of the other variables considered. In certain cases, the solution appears to diverge with refinement. These fluctuations suggest an inconsistency in the model.

The simulation parameters chosen for the fractional factorial design are largely orthogonal to each other. Even though a number of parameters influenced specific variables, the analysis revealed little or no interaction among the parameters in most cases.

One shortcoming of this method was identified. In the case of the time-averaged lift coefficient, the values were found to be extremely small approaching zero. Under these circumstances, it was not possible to differentiate between any main or interaction effects and the background noise.

The different simulation parameters are discussed in detail below.

6.4.3.1 Mesh Refinement (x1)

The mesh refinement is the most significant simulation parameter, as it influences the majority of the variables considered in the study. In addition, it was the most prominent variable in many cases and therefore, the CWE solution is very sensitive to the mesh size.

The mesh refinement has a significant influence on both the size and minimum velocity of the recirculation zone behind the cylinder as well as the downstream velocity. Moreover, the results were tending to converge with refinement of the mesh with the exception of downstream velocity. Similarly, the mesh refinement is a dominant factor affecting the base pressure and side face pressures. However, the graphical results would suggest further refinement is required for convergence to occur. Furthermore, the drag and lift coefficients are strongly dependent on the mesh size. It is likely that the ability of the finer grid to approximate peak values better than a coarse grid might be somewhat responsible for this marked improvement.

The stagnation pressure depends on the size of the mesh; however, it only has a minor impact on it.

The Strouhal number does depend on the mesh refinement. Although it is a dominant factor, its impact in comparison with the overall value is relatively minor. In fact, the Strouhal number would appear to be relatively insensitive to any of the parameters considered in this study.

It should be noted that for all fluctuating velocities and pressures as well as the fluctuating lift coefficient, their values were found to be entirely mesh dependent.

6.4.3.2 Time-step (x2)

The analysis did not reveal that the time-step significantly influenced any of the variables. It was shown to have a relatively minor impact on the length of the recirculation zone and the pressure on the top surface at 0.25H from the front corner. Typically, the time-setup is a critical factor in developing a parameter independent solution. This is credited to the PIMPLE algorithm, which utilizes under-relaxation to improve convergence of the solution during each time-step.

6.4.3.3 Upstream Length (x3)

The upstream length is an important parameter in determining the stagnation pressure. It is also has a minor impact on the recirculation zone behind the cylinder in terms of size and minimum velocity. Moreover, it would appear that these solutions converge as upstream length is increased.

Although it does have a minor influence on the drag coefficient, downstream velocity, base and side cylinder pressures, there is no evidence to suggest that the solution tends to converge as the length increases.

The Strouhal number does depend on the upstream length. Although it is a dominant factor, its impact in comparison with the overall value is relatively minor. In fact, the Strouhal number would appear to be insensitive to any of the parameters considered in this study.

6.4.3.4 Downstream Length (x4)

The downstream length only influences a few variables including the downstream velocity as well as the base and side cylinder pressures. Its influence is minor and there is no indication that the solutions converge with increased length.

6.4.3.5 Cross-stream Half-width (x5)

The cross-stream width has little or no influence on most of the parameters. It does impact the stagnation and base pressures. However, its impact is very slight and does not influence the drag coefficient as a result.

6.4.4 Optimal Configuration

Based on these results of the above analysis, the optimal configuration for the computational model has been determined as follows.

1.	Mesh refinement:	H/24	finest mesh
2.	Time-step:	0.0005 secs	largest time-step
3.	Upstream length:	15H	maximum length
4.	Downstream length	20H	median length
5.	Cross-section half-width:	10H	minimum width

Chapter 7

Stage II: Validation

7.1 Overview

In the final stage of the study involves the validation of the CWE solution. The validation stage sets out to determine if the mathematical model is a good representation of the physical phenomenon. The CWE simulation in this study considers high Reynolds number flow around a 3D square cylinder with a finite spanwise length. The optimal experimental parameters determined during the verification stage are used to inform the configuration of the model for the 3D simulation. The ideal situation would be to conduct additional verification of the 3D simulation before proceeding to the validation stage; however, this is not possible due to research time constraints. The simulation will be validated through comparison with the previous experimental studies, which are listed in Table 7.1 below.

In addition, the results from the present study will be compared with other similar CFD simulations in an effort to evaluate the performance of the present model and identify potential areas of improvement. The other simulations considered in this study and their attributes are summarized in Table 7.2 below.

7.2 Flow Visualization

The flow fields (i.e., velocity, pressure, etc.) were visualized using the Paraview. The variation of the velocity filed with time for a single vortex shedding cycle is shown in Figure 7.1 below. The regions of low and high-speed flow are shown as blue and red, respectively, while the contours denote the magnitude of vorticity.

Figure 7.1: Summary of previous experimental studies

Study	Bearman[1]	Bearman[2]	Durao[3]	Lee[4]	Lyn[5]	Lyn[6]
	(1975)	(1981)	(1988)	(1975)	(1994)	(1995)
Reynolds number, Re	20,000 – 70,000	5,800 – 32,000	14,000	176,000	21,400	21,400
Turbulence (%)	0.3 %	0.04 %	6 %	0 – 12.5 %	2 %	2 %
Blockage (%)	6 %	5.5 %	12.8%	3.6 %	7 %	7 %
Measurement method	PT & HW	PT	LDV	PT	LDV	LDV
Base Pressure, C_{pb}	1.4	1.6	-	0.8 -1.4	-	-
Drag Coefficient, C_d	2.2	-	-	1.5 - 2.2	-	-
Lift Coefficient, C_l	-	1.2	-	-	-	-
Strouhal Number, St	0.125	0.130	0.133	0.120 – 0.126	0.134	0.132

Superscript Notes:

1. Bearman and Trueman (1975): Time-averaged results from pressure tappings (PT) and flying-hot-wire anemometry (HW)
2. Bearman and Obasaju (1981): Time-averaged results from pressure tappings (PT)
3. Durao et al. (1988): Time-averaged results from Laser Doppler Velocimetery (LDV)
4. Lee (1975): Time-averaged results from pressure tappings (PT)
5. Lyn and Rodi (1994): Time-averaged and phase-averaged results from Laser Doppler Velocimetery (LDV)
6. Lyn et al. (1995): Time-averaged and phase-averaged results from Laser Doppler Velocimetery (LDV)

Table 7.2: Comparative computational fluid dynamics studies

Study		**Present**	**Franke et al.**	**Lee**[1]	**Shimada**[2]	**Tamura**[3]	**Tian et al.**	**Dahl**
		(-)	(1990)	(1998)	(2001)	(2003)	(2012)	(2014)
Simulation		3D	2D	3D	2D	3D	2D	2D
Method		RANS	DNS	LES	RANS	LES	RANS	RANS
Turbulence Model		k-ω	-	-	k-ε	-	k-ω SST	k-ε
Turbulence Intensity, I_u	[%]	2.0	-	0.5	-	0.0 – 13.0	2.0	0.8
Domain Size		35Hx21Hx2H	20Hx12H	22.5Hx14Hx2H	30H (radius)	38Hx29Hx2H	35Hx20H	40Hx20H
Elements		597,990	-	47,700	-	-	77,670	155,300
Blockage	[%]	4.8	8.3	7.1	1.6	3.4	5	5
Mesh Size, $\Delta H / H$	[-]	0.0417	0.0013 – 0.0063	~0.0100	-	-	0.0020	0.0013 – 0.0180
Time Step, $(U^*\Delta t) / H$	[-]	0.0256	-	0.005	-	-	0.004	0.002
CFL No., $(U^*\Delta t) / \Delta H$	[-]	0.615	-	~0.500	-	-	2.000	0.111 – 1.530
Reynolds No., Re	[-]	21,721	40 – 300	22,000	22,000	22,000	21,400	20,000

Superscript Notes:

1. Lee and Bienkiewicz (1998)
2. Shimada and Isihara (2001)
3. Tamura and Ono (2003)

Figure 7.1: 3D simulation velocity field with vorticity contours varying with time

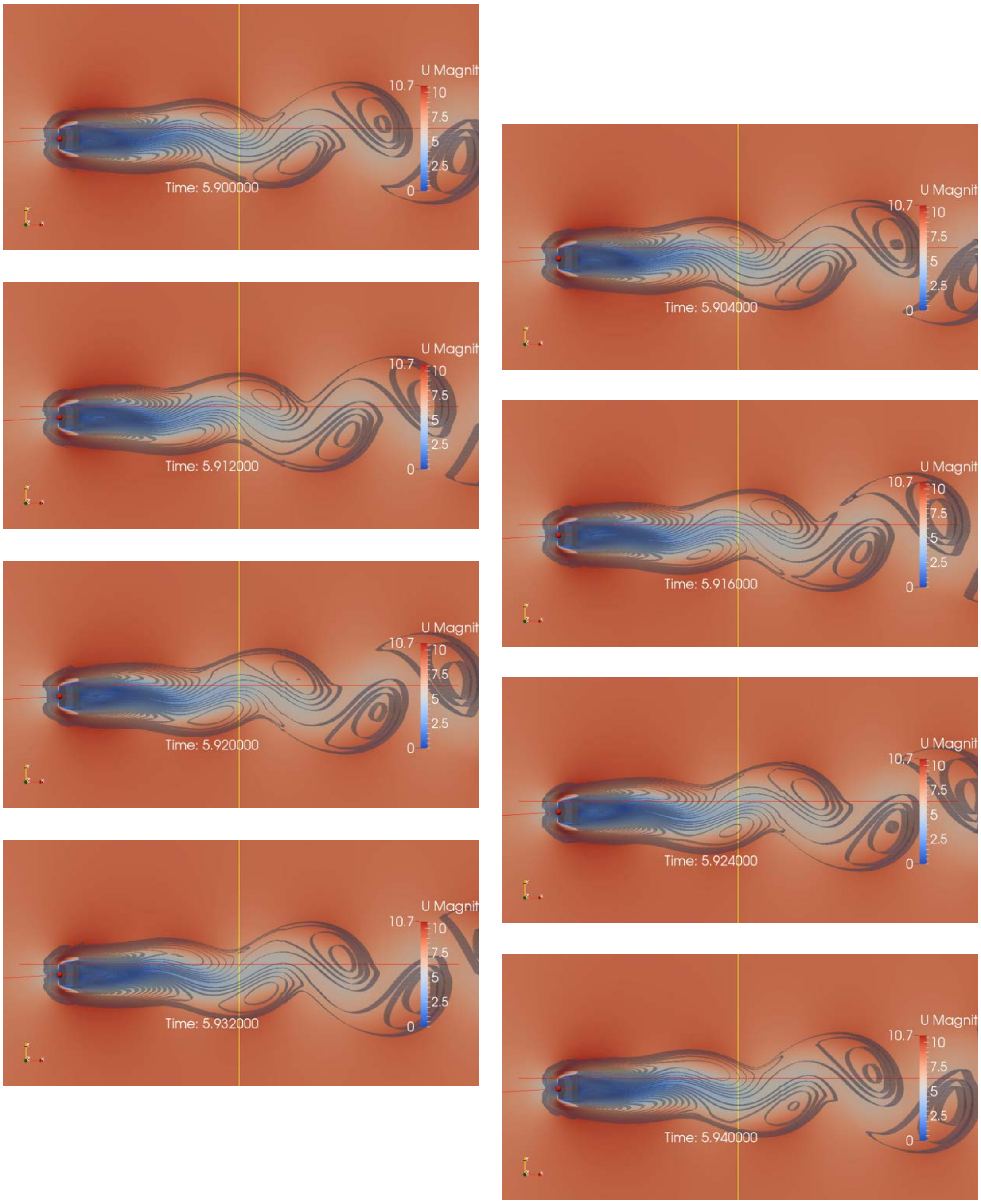

It is immediately apparent that the velocity field is remarkably different than the flow field encountered during the verification stage. As before, the flow accelerated around the body separates, due to the abruptness of the front corners, forming free shear layers on each side. However, the same jet-like thin layers are not apparent in the vorticity contours. Examination of the entire vortex shedding cycle reveals that shear layers on the top and bottom of the cylinder remain almost parallel to the cylinder surfaces. The absence of shear layer curvature leads to less cross-stream mixing a less interaction between the shear layers. The delayed interaction between the shear layers permits a longer wake to form behind the cylinder as shown in Figure 7.2. However, although the wake extends over a larger region, the base pressure is higher as shown in Figure 7.3. As a result, weaker vortices form further downstream of the cylinder.

The Q-criterion field, which is illustrated in Figure 7.4 below, reveals discrete regions of high Q-criterion in close proximity to the square cylinder. This suggests vortices are shed close to the square cylinder. However, the vorticity field, which is shown in Figure 7.5, appears to indicate that vortex shedding occurs further downstream consistent with the velocity and pressure fields.

Figure 7.2: 3D simulation instantaneous velocity field with vorticity contours

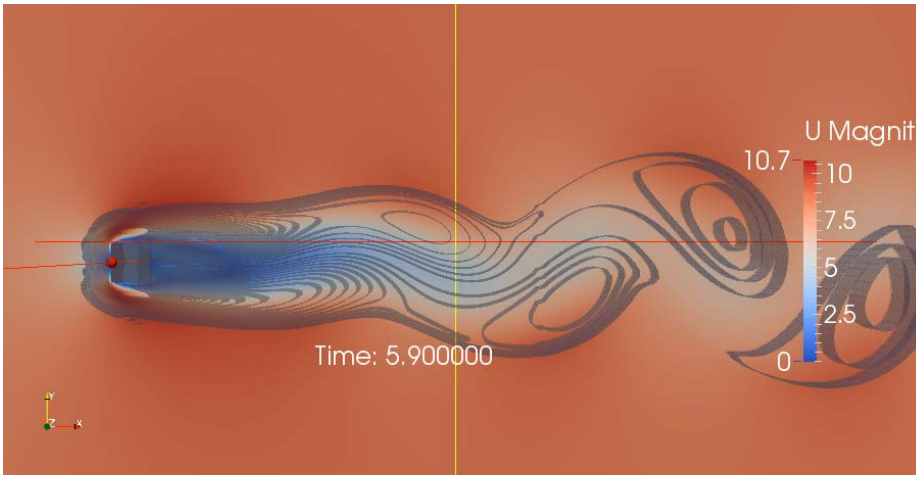

It should be noted that the flow visualizations examine the flow as it approaches 6 seconds simulation time, while the previous evaluations examined the flow after 14 seconds simulation time. This could account for the discrepancies if the flow has not transitioned from a steady state condition to a fully developed unsteady flow condition after 6 seconds of simulation time.

Figure 7.3: 3D simulation instantaneous pressure field with vorticity contours

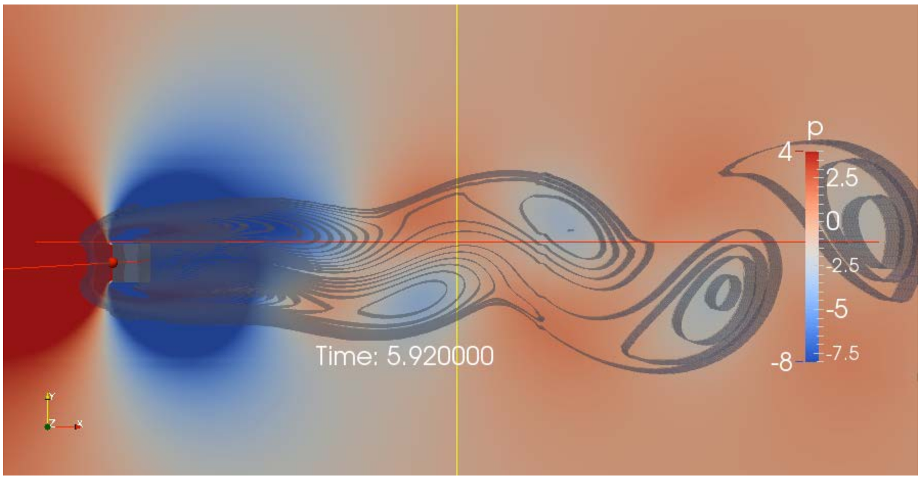

Figure 7.4: 3D simulation instantaneous Q-criterion field with vorticity contours

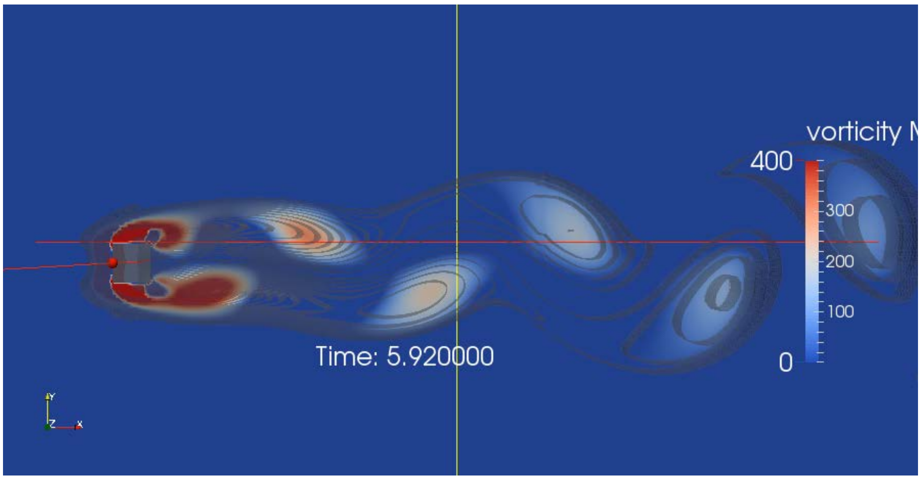

Figure 7.5: 3D simulation instantaneous vorticity field with contours

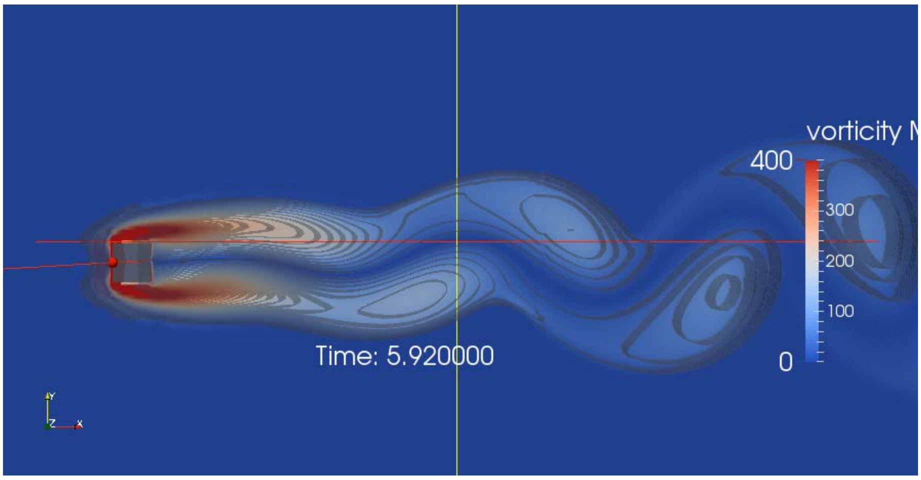

7.3 Time-averaged Variables

7.3.1 Velocity

Figure 7.6: 3D Prism: velocity time history at x/H= 0.5 from rear surface

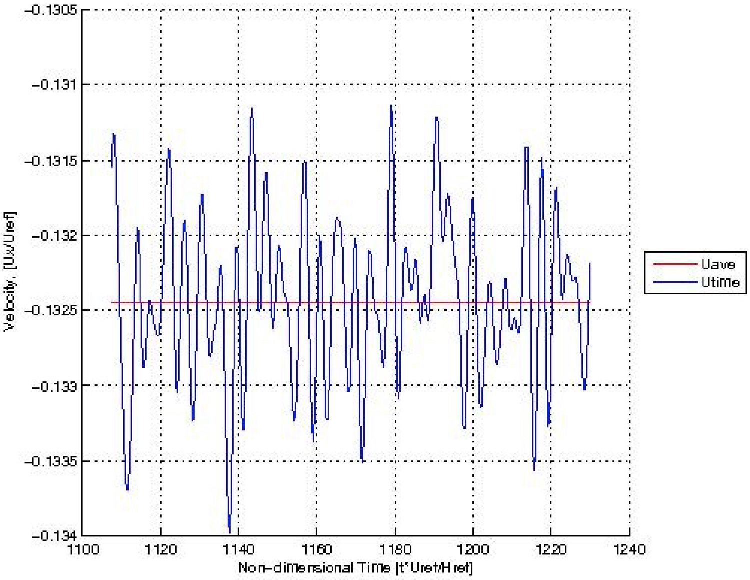

Figure 7.7: case 16: velocity time history at x/H= 0.5 from rear surface

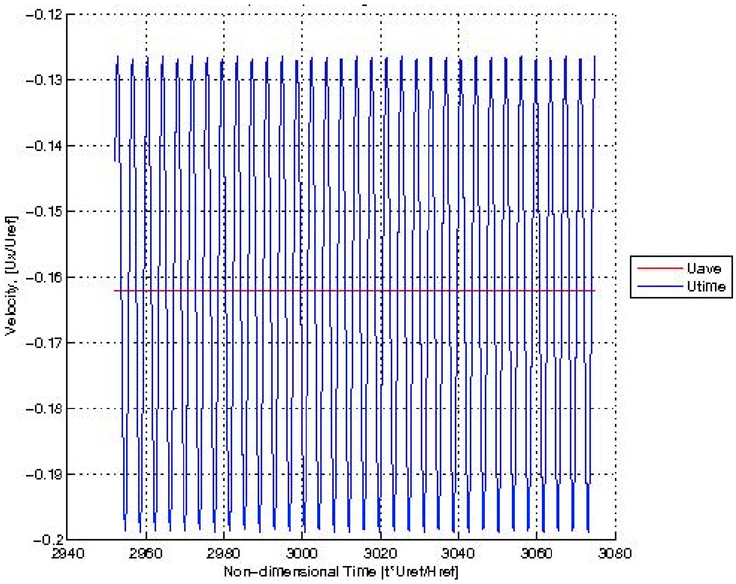

Past experiments have shown although the high Reynolds number flow around a square cylinder is unsteady; the flow is periodic rather than erratic. However, the time history of the along-wind velocity at a distance x/H = 0.5 behind the 3D square cylinder, which is shown in Figure 7.6, is random. This is inconsistent with the velocity time-histories determined during the verification stage, such as in case 16 shown in Figure 7.7, which indicates a sinusoidal oscillation of equal amplitude. Therefore, it is assumed that this irregularity is due to the flow transitioning from a steady state to a fully developed unsteady state. It is assumed that once the unsteady flow is fully developed, that the results will closer resemble the results of case 16 of the verification stage. Therefore, the validation stage shall only consider case 16 of the verification stage.

Figure 7.8: Time-averaged along-wind velocity along centerline

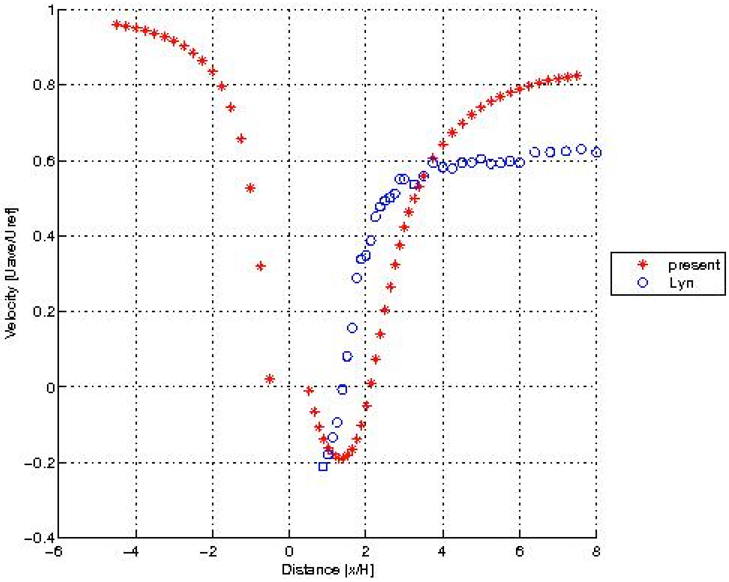

The time-averaged profile along the centerline of the domain, which is shown in Figure 7.7, shows a rapid decrease in velocity as the flow approaches the cylinder, which is consistent with other simulations. As discussed earlier, the upstream velocity does asymptote to unity but this occurs further upstream closer to the inlet.

The minimum velocity in the recirculation zone is predicted to occur at a non-dimensional distance equal to 0.886 downstream of the rear face. The distance is around double the distance downstream of 0.4 and 0.5 measured by Lyn et al. (1995) and Durao et al. (1988), as listed in Table 7.3 below. Moreover, the other CFD simulations underestimate this distance in comparison to the experimental results.

The length of the recirculation zone is estimated at a non-dimensional distance of 1.632. This is a significant over-estimate recirculation zone given that the experimental results indicate the length between 0.8 and 1.0 according to Lyn et al. (1995) and Durao et al. (1988), respectively. Typically, the other CFD simulations underestimated the length of this zone, although Lee and Bienkiewicz (1998) did estimate a recirculation zone length (i.e., 0.9) consistent with experimental results, as shown in Table 7.3. Shimada and Isihara (2002) suggest that the size of the zone is related to the level of turbulent mixing in the flow.

Given that the present study overestimates the position of the minimum velocity and the length of the recirculation zone when compared with experimental results, which is in complete contrast to the previous studies, there must be at least one distinctive aspect of this simulation responsible for this uncharacteristic behavior. It was noted earlier that care is required when using wall functions and they are not suited for flow near solid boundaries and for separated flows, in particular. The wall functions were adopted in this study to avoid using a very fine mesh. Examination of the other studies revealed that an extremely fine mesh was provided at boundaries rather using a wall function, even though turbulence models were utilizes. Furthermore, Shimada and Isihara (2002) plot results from a paper by Kato and Launder (1995) where the minimum velocity occurs at approximately 0.8 from the rear face and the recirculation zone has an approximate length of 1.3. The Kato and Launder study used a k-epsilon turbulence model and wall functions. Therefore, it is likely that the wall function is responsible for the atypical behavior of the CWE model in the vicinity of the recirculation zone.

The present study gives a reasonable good prediction of the magnitude of the downstream velocity. The experimental results measure downstream velocity between 0.6 (Lyn et al., 1995) and 0.9 (Durao et al., 1988). Typically, the other CFD studies prediction is close to the Durao et al. measurement. This study estimates the downstream velocity equal to 0.8, which is between both experimental results and is consistent with Lee and Bienkiewicz (1998) result.

Figure 7.9: Time-averaged and std. deviation velocity profile at x/H = 1.5

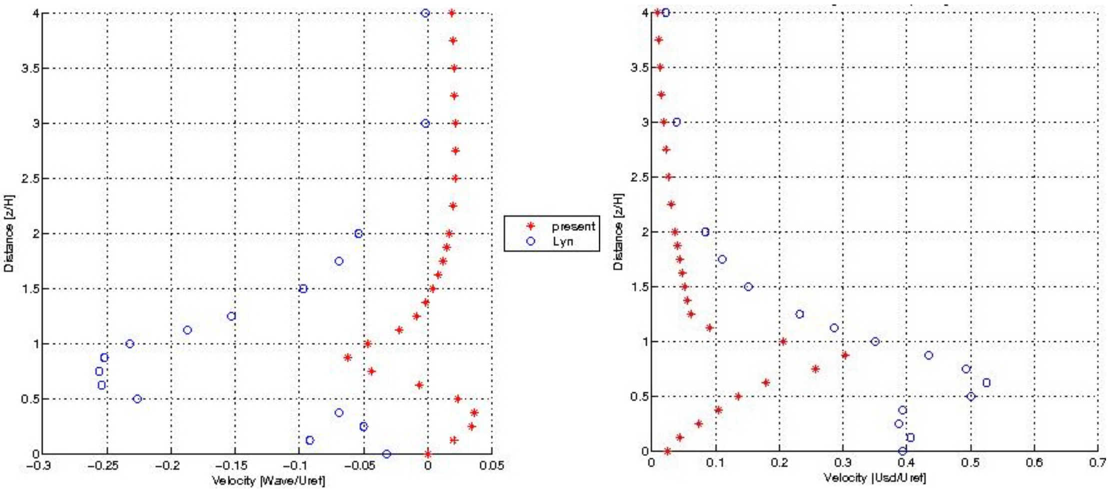

Figure 7.10: Time-averaged and std. deviation velocity profile at x/H = 2.5

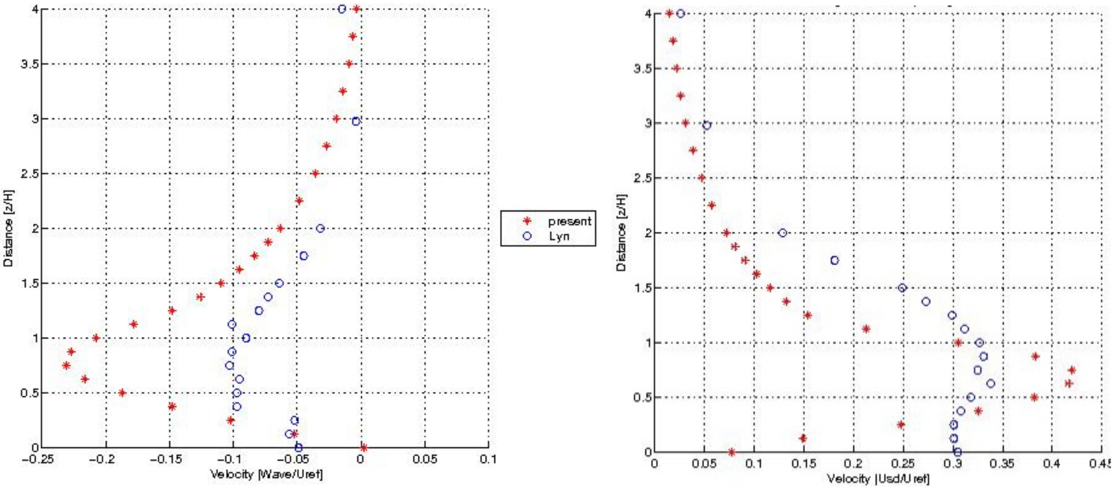

It is clear from in Figures 7.9 and 7.10 that the velocity field remote from the centerline downstream of the cylinder indicates the turbulence in the vicinity of the cylinder is poorly modeled. At x/H = 1.5, the velocity of the cross-stream flow is significantly underestimated as are the fluctuation in the along-wind direction.

Further downstream at x/H = 2.5, the flow field is approximated better, the peak cross-stream velocity is significantly overestimated while the along-wind velocity is both underestimated and overestimated depending on position in the flow. It is difficult to ascertain if this is a common problem of CWE models or if it is unique to this study because none of the other studies presented results on this aspect of the flow field. It might be due to the attenuation of the smaller fluctuations in the flow, which are treated as turbulent components by Reynolds-averaging. Alternatively, it could be an artifact of the wall function applied in close proximity to the cylinder.

The comparison of the velocity related variables determined in this study with the results of other studies are listed in Table 7.3 below.

7.3.2 Kinetic Energy

Figure 7.11: Residual kinetic energy along centerline

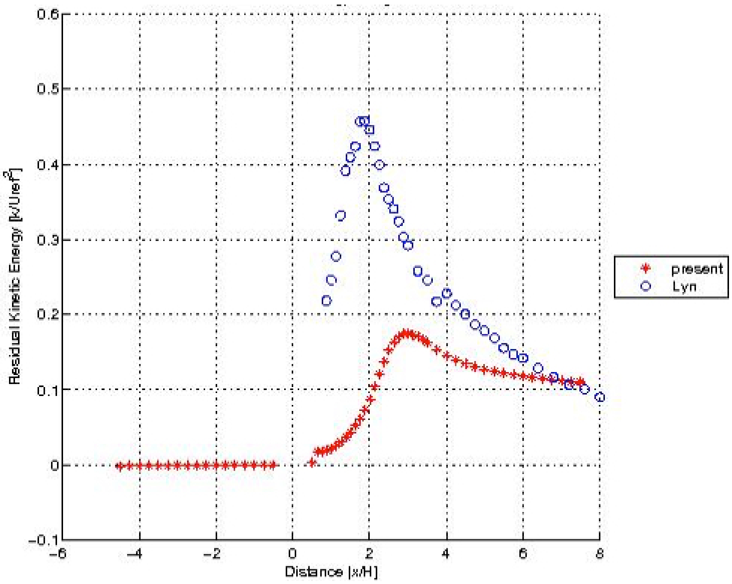

The kinetic energy associated with the turbulent fluctuations in the flow is plotted in Figure 7.11 above. The peak residual kinetic energy is approximately 30% of the kinetic energy predicted by experiment (Lyn et al., 1995). Shimada and Isihara estimated the peak residual kinetic energy at approximately 60% the measured experimental value (Lyn et al., 1995). Shimada and Isihara suggest that "the treatment of the flow near the solid boundary significantly influences the turbulence statistics". In particular, Shimada and Isihara (2002) reference a Kato and Launder (1993) study that estimated low kinetic energy associated with turbulent fluctuations, which used wall functions in conjunction with a k-epsilon model. This study predicted the peak residual kinetic energy at 50% the experimental value (Lyn et al., 1995). It should be noted that underestimation in residual kinetic energy is not a characteristic of RANS models alone. The study conducted by Lee & Bienkiewicz (1998) using LES found that the contribution to the total kinetic energy from the turbulent fluctuations amounted to 23% in the simulation rather than 45% as indicated by experimental results (Lyn et al., 1995) In this case, the reduced peak residual kinetic energy was attributed to an upwind scheme used in the numerical approximations.

7.3.3 Pressure

The time histories of pressure at the center of the front and back faces of the square cylinder reveal that periodic fluctuations occur on both faces, as shown in Figure 7.12. The fluctuations on the back face are more important than those on the front face. Examination of the pressure time histories associated with the top and bottom faces reveal that the fluctuations consist of alternating sinusoidal oscillations of constant amplitude.

Inspection of the time-averaged pressure distribution in Figure 7.13 shows good correlation with results from previous experiments and studies on the front face of the cylinder. However, it should be noted that the pressure on the front face. There is a slight error in the prediction of the pressure on the front face due to OpenFOAM using the inlet as its reference pressure instead of the outlet. It is estimated that the front face pressure is over-estimated by as much as 6%.

Table 7.3: Comparison of velocity related variables with other experiments and studies

Study		Present	Durao[1]	Lyn[2]	Lee[3]	Shimada[4]	Tian[5]	Dahl
		(-)	(1988)	(1995)	(1998)	(2001)	(2012)	(2014)
Distance to minimum velocity	X_{p5}	0.886	0.5	0.4	0.4	0.3	0.3	0.3
Size of recirculation zone	X_{p6}	1.632	1.0	0.8	0.9	0.5	0.7	0.6
Downstream velocity	$u_{7,ave}$	0.805	0.9	0.6	0.8	0.9	0.9	0.9

Superscript Notes:

1. Durao et al. (1988)
2. Lyn et al. (1995)
3. Lee and Bienkiewicz (1998)
4. Shimada and Isihara (2001)
5. Tian et al. (2012)
6. Dahl (2014)

In the present study, predicts the pressure at 0.25H from the front corner to be -1.294. This appears reasonable in the context of experiments by Lee (1975) that indicate a range of -1.2 to -1.6 for this pressure, as shown in Table 7.4. However, Lee did examine flows with turbulence intensities as high as 12.5% and the more positive pressures are associated with these higher turbulence intensities. Therefore, it is likely that the pressure should lower than predicted. Typically, other CFD simulations estimate pressure to be -1.8 in this region, which is consistent with Bearman and Obasaju (1981).

Figure 7.12: Pressure time history on center of front, back and side faces

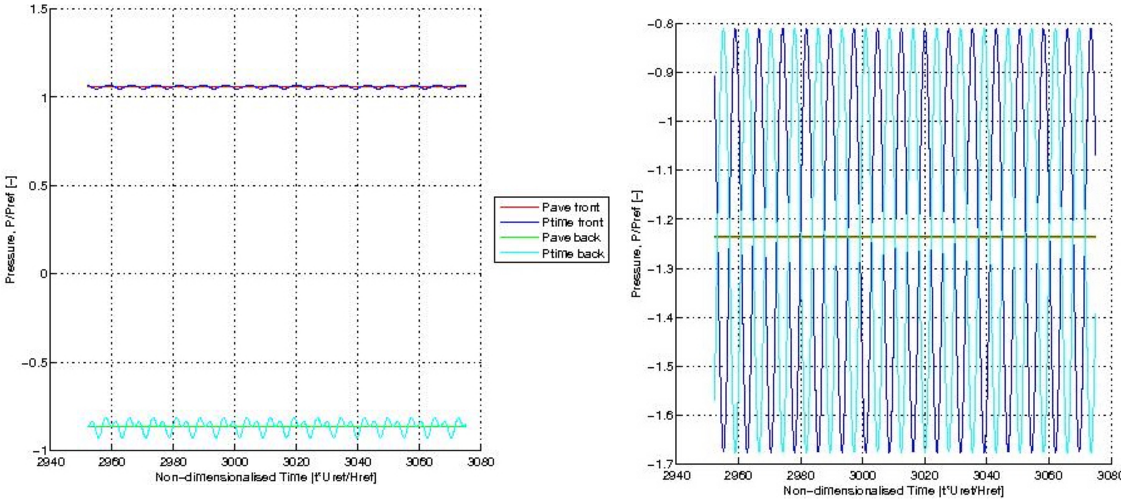

The experiments conducted by Lee (1975) revealed that the maximum average pressure could occur anywhere on the side face depending on turbulence intensity. Bearman and Obasaju (1981) found the point of maximum pressure near the center of the side. Tian et al (2012) and Dahl (2014) noted similar results in their simulations. However, a peak pressure concentration developed at the front corner of the cylinder in many other simulations. In this study, the maximum pressure was situated at 0.188 from the front corner.

The CWE simulation in the present study displays a smooth pressure distribution of the back face, which is consistent with measurements undertaken by

Lee (1975). However, the base prediction of -0.862 is significantly higher than any other experiment or simulation. Experimental results from Lee (1975) and Bearman and Obasaju (1981) would indicate that the base pressure for a relatively low turbulent flow should be close to -1.4 and -1.6. Other CFD simulations, as listed in Table 7.4, estimate the base pressure to be between 1.4 and 2.0.

Figure 7.13: Time-averaged pressure on surfaces of the cylinder

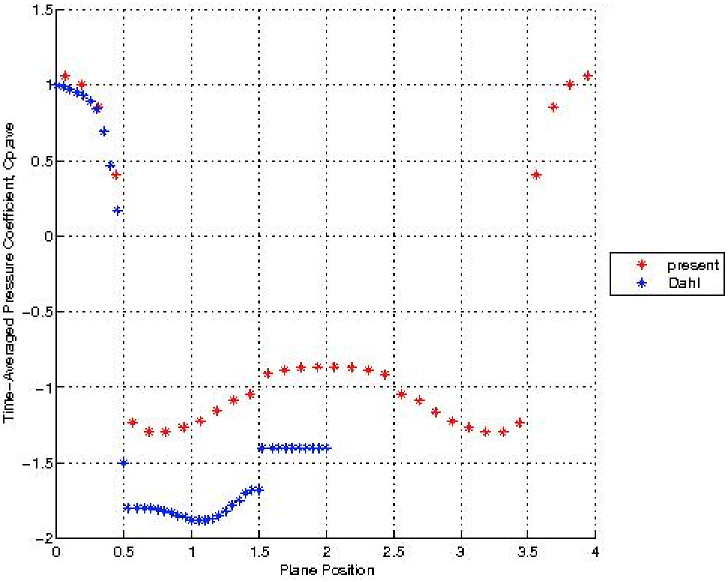

Figure 7.14: Root-mean-square pressure on surfaces of the cylinder

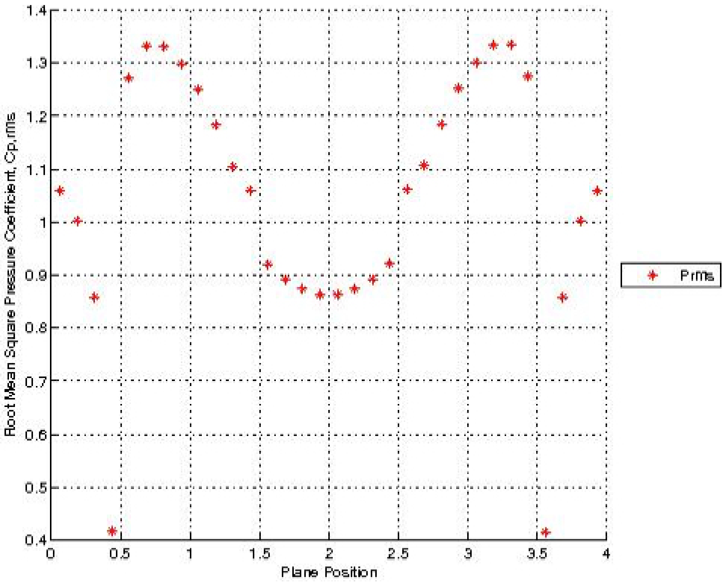

Table 7.4: Comparison of pressure related variables with other experiments and studies

Study		Present	Bearman[1]	Lee[2]	Bearman[3]	Lee[4]	Shimada[5]	Tamura[6]	Tian[7]	Dahl[8]
		(-)	(1972)	(1975)	(1981)	(1998)	(2001)	(2003)	(2012)	(2014)
Stagnation pressure	$C_{ps,ave}$	1.058	-	1.0	1.0	1.0	1.05	1.0	1.0	1.0
Base pressure	$C_{pb,ave}$	0.862	1.4	0.8 – 1.4	1.6	2.0	1.8	1.5	1.9	1.4
Pressure at 0.25H from front corner	$C_{p3,ave}$	-1.294	-	-1.2 – -1.6	-1.8	-2.0	1.7	1.5	1.8	1.8
Distance to min pressure	X_{p4}	0.188	-	0.0 – 0.9	0.6	0.0	0.0	0.0	0.5	0.5

Superscript Notes:

3. Bearman and Trueman (1972)
4. Lee (1975)
5. Bearman and Obasaju (1981)
3. Franke et al. (1990)
4. Lee and Bienkiewicz (1998)
5. Shimada and Isihara (2001)
6. Tamura and Ono (2003)
7. Tian et al. (2012)
8. Dahl (2014)

The difference in pressure coefficients between the experimental results and this study is ascribed to the use of wall functions. Although the CWE model gives a reasonable good approximation of the stagnation pressure, it gives a poor approximation of the pressure further downstream after the flow has encountered the body. Both Tian et al. (2012) and Dahl (2014) predict the pressure at 0.25H from the front corner and the location of maximum pressure on the side face reasonably well using RANS with a turbulence model. In both cases, however, a fine mesh near the boundaries is adopted instead of using wall functions. Moreover, it was noted earlier that the introduction of wall functions results in a larger recirculation zone, which could be responsible an increase in base pressure experienced in the present study.

7.3.4 Drag and Lift Coefficient

Figure 7.15: Time series of drag force

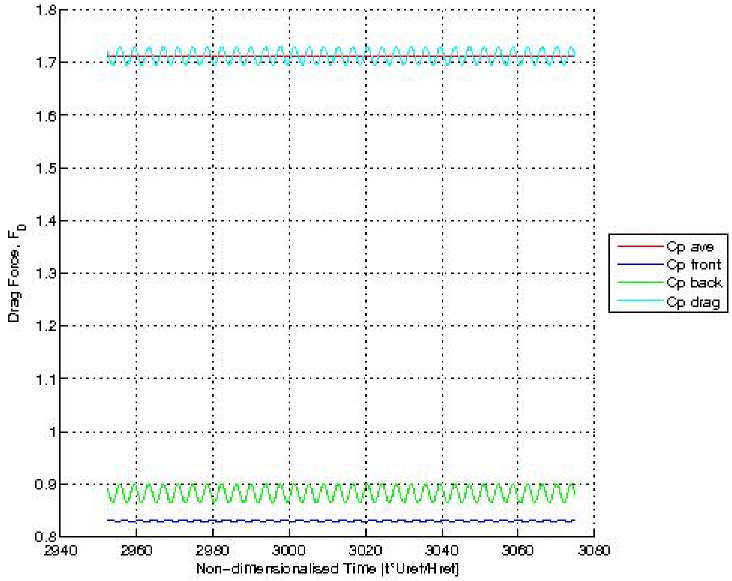

The time histories of the front and back face pressures have been plotted with the variation in the drag coefficient over time in Figure 7.14. It is clear that time the front and back face pressures are similar in magnitude. The drag coefficient is calculated as the difference between these two pressures and therefore, time-averaged drag coefficient is predicted at slightly greater than 1.7. While this is consistent with some of the earlier CFD models, it differs greatly from more recent CFD studies (Shimada and Isihara, 2001) (Tamura and Ono, 2003) (Tian et al, 2012) (Dahl, 2014) and it is significantly lower than the relevant values predicted by Bearman and Trueman (1972) and Lee (1975).

In addition, it is apparent from Figure 7.14 that the fluctuation in drag coefficient is closely related to the fluctuation on the back face, as the fluctuations on the front face of the cylinder are less significant.

The time histories for the top and bottom pressures have been plotted alongside the variation of the lift coefficient over time in Figure 7.15. It is clear that the top and bottom pressures oscillate about an equivalent pressure range but are completely out of phase with each other. As a result, lift coefficient oscillations are sinusoidal and they fluctuate about zero, which is consistent with flow theory around a symmetric bluff body.

Figure 7.16: Time series of lift force

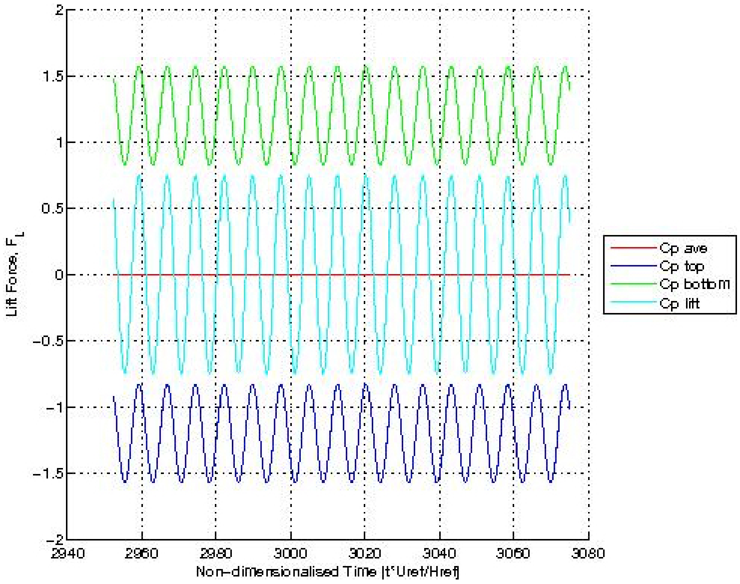

However, it would appear that the magnitude of the fluctuations predicted in this study is too small. Shimada and Isihara (2002) predicted the lift coefficient oscillates between -2.0 and 2.0, as opposed to -0.7 and 0.7 as shown in Figure 7.15

above. Other studies predict the root-mean-square (RMS) of the lift coefficient between 1.0 and 1.5, while the present study estimates this value closer to 0.5. Shimada and Isihara (2002) did suggest that the fluctuations in the lift coefficient are related to the turbulent mixing and the size of the wake. This might explain the error in the calculation of the lift coefficient. Due to the presence of the wall function near the boundaries, the flow near the boundary and the separation of the shear layer is modeled incorrectly. This leads to an over-estimation of the size of the wake. The flow is unable to support a significant low pressure in the wake zone due to the scale of the wake. This results in the base pressure becoming uncharacteristically high, which causes a reduction in the strength of the vortices that leads a reduction in the magnitude of the suction pressures on the side faces and therefore, a reduction in the amplitude of the lift coefficient.

Figure 7.17: Spectrum of lift force

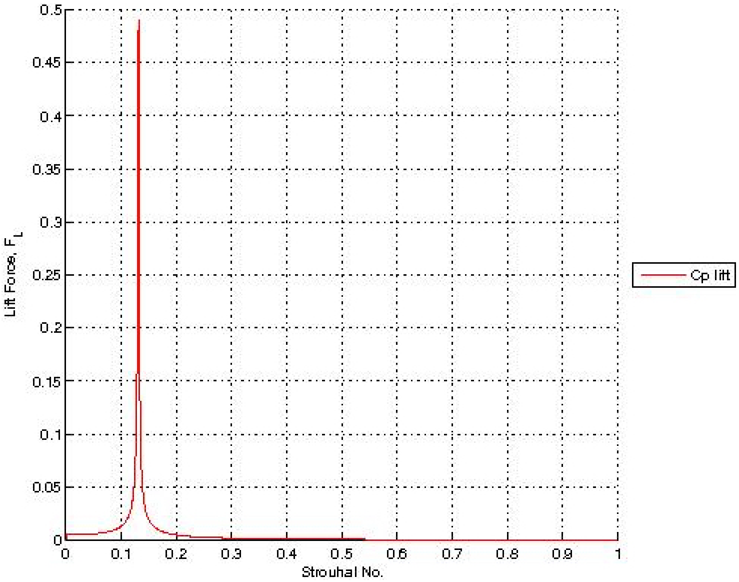

The Fourier Fast Transform of the lift coefficient time series data identifies a single peak frequency. The Strouhal number is calculated at 0.133. This is consistent, if slightly higher, than the results of experiments in the past (Bearman and Trueman, 1972) (Lee, 1975) (Bearman and Obasaju, 1981) (Lyn, 1995). However, it is lower than many other CFD simulations (Shimada, 2002) (Tian et al., 2012) (Dahl, 2014). It is a shame the 3D simulation had not transitioned to full transient flow sooner, as Shimada and Isihara (2002) found better correlation in the 3D results than in the 2D results for estimated the Strouhal number and it would be interesting to determine if the 3D simulation does provide a more accurate result. Interestingly, the different studies do predict a range of values for the Strouhal number, however, the mesh refinement and upstream length were only found to moderately influence the result. Therefore, there must be another parameter that influences the Strouhal number.

It should be recognized that although the k-omega wall function negatively impacts that accuracy of the CWE model, the adoption of a turbulence model, such as the k-omega, could be beneficial in terms of generating an accurate solution. Franke et al. (1990) found that a turbulence model is required to give reasonably accurate results for drag, lift and Strouhal number for large Reynolds number flows. Similarly, Shimada and Isihara found the variation of drag and lift coefficients with time erratic without a turbulence model. Moreover, the aerodynamic coefficients oscillated in a sinusoidal fashion with the introduction of a turbulence model.

Figure 7.18: Time series of lift and drag force

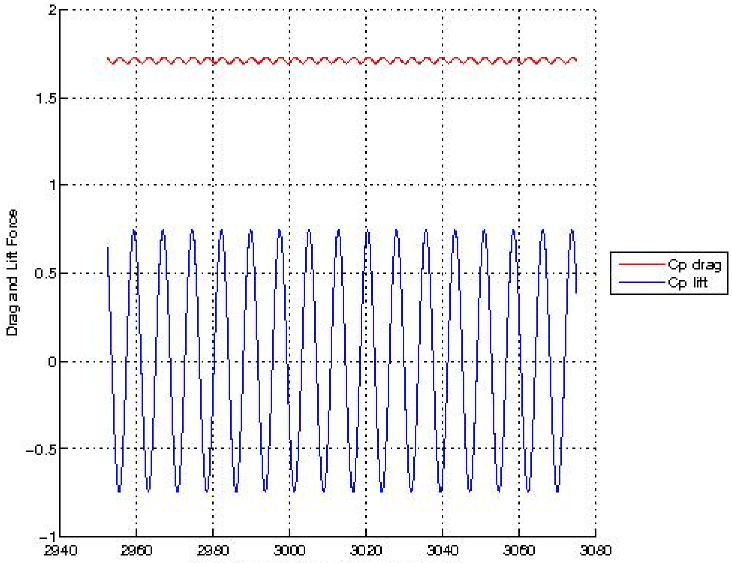

Table 7.5: Comparison of drag and lift related variables with other experiments and studies

Study		**Present**	**Bearman[1]**	**Lee[2]**	**Bearman[3]**	**Franke[4]**	**Lyn [5]**	**Lee[6]**	**Shimada[7]**	**Tamura[8]**	**Tian[9]**	**Dahl[10]**
		(-)	(1972)	(1975)	(1981)	(1990)	(1995)	(1998)	(2001)	(2003)	(2012)	(2014)
Drag Coeff	$C_{d,ave}$	1.712	2.20	1.5 – 2.2	-	1.55 – 1.89	-	1.67 – 1.97	2.050	2.130	2.060	2.098
Lift Coeff	$C_{l,rms}$	0.527	-	-	1.20	0.16 – 1.84	-	0.30 – 1.09	1.430	1.200	1.492	1.402
Strouhal No.	St	0.133	0.125	0.12 – 0.13	0.130	0.13 – 0.16	0.13 – 0.14	0.15 – 0.16	0.141	0.125	0.138	0.137

Superscript Notes:

1. Bearman and Trueman (1972)
2. Lee (1975)
3. Bearman and Obasaju (1981)
4. Franke et al. (1990)
5. Lyn et al. (1995)
6. Lee and Bienkiewicz (1998)
7. Shimada and Isihara (2001)
8. Tamura and Ono (2003)
9. Tian et al. (2012)
10. Dahl (2014)

7.4 Phase-averaged Variables

7.4.1 Introduction

Turbulent flow can be envisaged as random fluctuations oscillating about a time-averaged mean. Alternatively, if there are coherent turbulent structures present within the flow, the turbulent flow can be decomposed into three distinct components: a time-averaged mean flow, a periodic flow with zero mean and a random fluctuating component. The advantage of this approach is that the periodic component can be resolved into a number of different phases. It is possible to develop ensemble averages for each phase if the flow is investigated over a sufficiently large time period.

Hussain (1988) defines a coherent structure is a comparatively large region of turbulent fluid with phase correlated vorticity over its spatial extent. Coherent structures cannot be defined by velocity and pressure alone. Instead, coherent structures are characterized regions that contain high levels of coherent vorticity, Reynolds stresses, production and mass transportation. They are not associated with areas of high kinetic energy necessarily, as it is the incoherent turbulence that is mostly responsible for high levels of kinetic energy. Coherent structures are mutually exclusive and their interaction leads to the formation of new structures. Vortex rings, vortex rolls and vortex spirals are all considered coherent structures.

In the case of flow past a square cylinder, vortices form downstream of the body and their formation is exactly periodic. Furthermore, the variation the frequency of the lift coefficient fluctuations is equivalent to the vortex shedding frequency. The identification of coherent structures is unnecessary. The Strouhal number can be used to identify the duration of the vortex shedding cycle and therefore, it facilitates the decomposition of the flow into a number of phases. For validation purposes, the phase-averaged results from simulated data are compared with phase-averaged from a past experiment conducted by Lyn et al. (1995).

7.4.2 Velocity

Figure 7.19: Velocity streamlines fixed reference frame

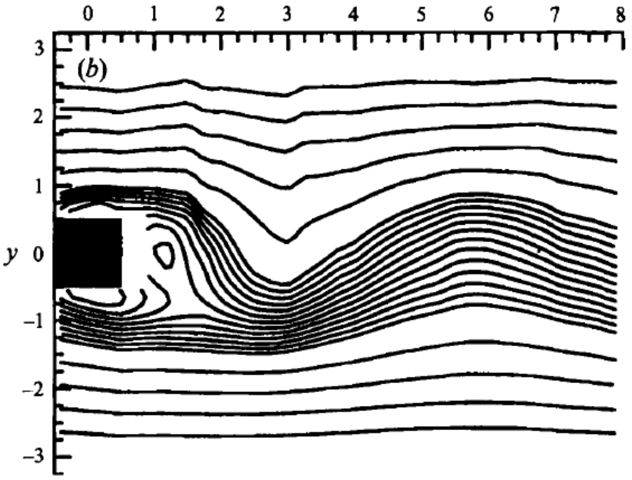

Streamlines are not Galilean invariant and the velocity of the reference frame is very important (Lyn et al, 1995). In fact, the velocity at any point in the field is dependent upon the motion of the frame of reference. Figure 7.19 shows the phase-averaged velocity streamlines is flow past a square cylinder given a fixed of reference frame. Only two distinguishing features are visible: a center and a saddle, which are located immediately downstream of the rear of the cylinder (Lyn et al., 1995). In Figure 7.20, the streamlines are more accurate, as the reference frame is moving downstream at approximately the same velocity as the vortices s being shed (Lyn et al., 1995). The velocity of the frame of reference is critical (Lyn et al., 1995). This moving frame is difficult to apply, as vortices accelerate downstream after shedding. In any case, the difference is striking. The vortices obscured in Figure 7.19 are clearly present in Figure 7.20.

Figure 7.20: Velocity streamlines moving reference frame

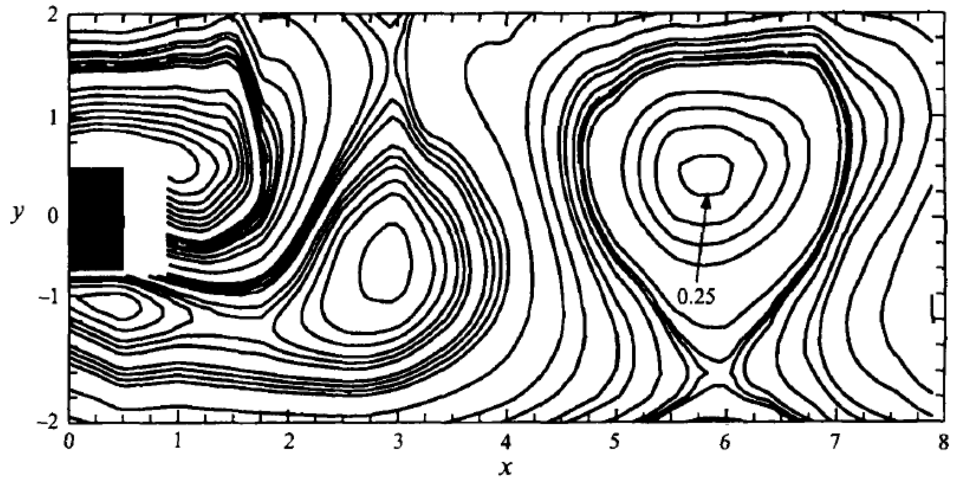

It was difficult to implement a moving reference frame in this study. A frame of reference fixed on the square cylinder was used for the comparison with the experimental data (Lyn et al., 1995). Lyn et al. (1995) carried out an extensive analysis of phase-averaged data. The Lyn et al. (1995) study focused on phase (9.19), which is the phase when a vortex is shed from the bottom face of the cylinder. For the purposes of validation stage, it was necessary to identify the equivalent phase from the simulated data. After examining all the phases of the shedding cycle, phase 1 of the present study is considered the closest match to phase (9,19) examined by Lyn et al (1995).

7.4.3 Phase-averaged Periodic Normal and Reynolds Stresses

The phase-averaged periodic along wind normal stress component, $<\tilde{u}\tilde{u}>$, is symmetric about the centerline in accordance with the experimental results of Lyn et al (1995), which are shown in Figure 7.22. Although the distribution of the stresses is comparable with the experimental data as shown in Figure 7.23, the magnitude of $<\tilde{u}\tilde{u}>$ is significantly different that Lyn et al. measured. The peak value, which situated downstream of the upper rear corner, is approximately 50 times smaller the experimental measurement as indicated in Table 6.7.

Figure 7.21: Comparison of phase-averaged streamlines

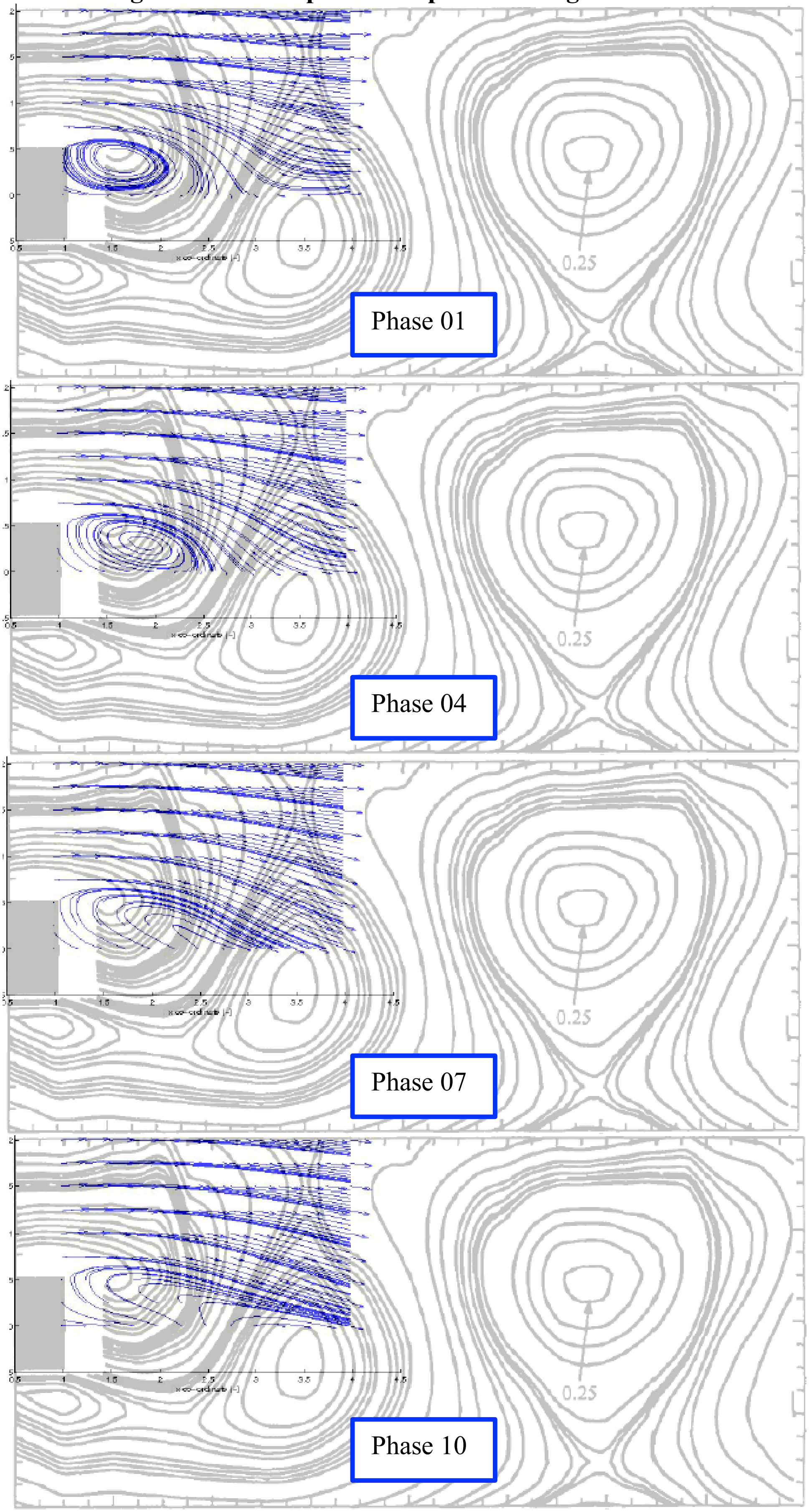

Figure 7.21: Comparison of phase-averaged streamlines (cont'd)

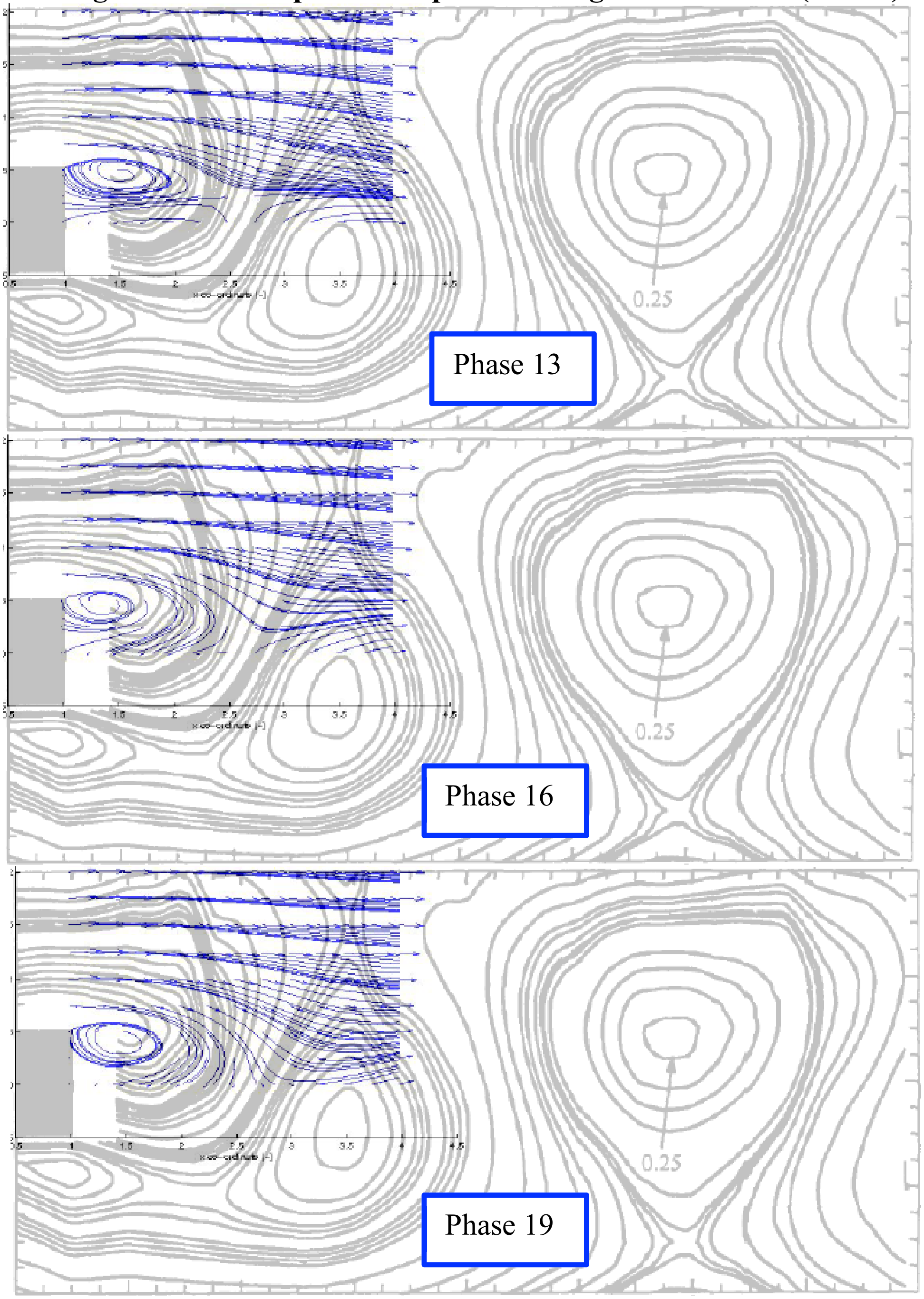

Figure 7.24 reveals that the periodic phase-averaged across wind normal stress component, $\tilde{v}\tilde{v}$, is also symmetric about the centerline, which is consistent with Lyn et al (1995) experimental results. Once more, although the distribution of the stresses is similar to the experimental data, the magnitude of $\tilde{u}\tilde{u}$ is significantly different that Lyn et al. measured. The peak values, which are shown along the centerline in Figure 7.25, differ by a factor of 50 as indicated in Table 6.7

Figure 7.22: Lyn et al. (1995) phase-averaged periodic along wind normal stress, $< \tilde{u}\tilde{u} >$, component

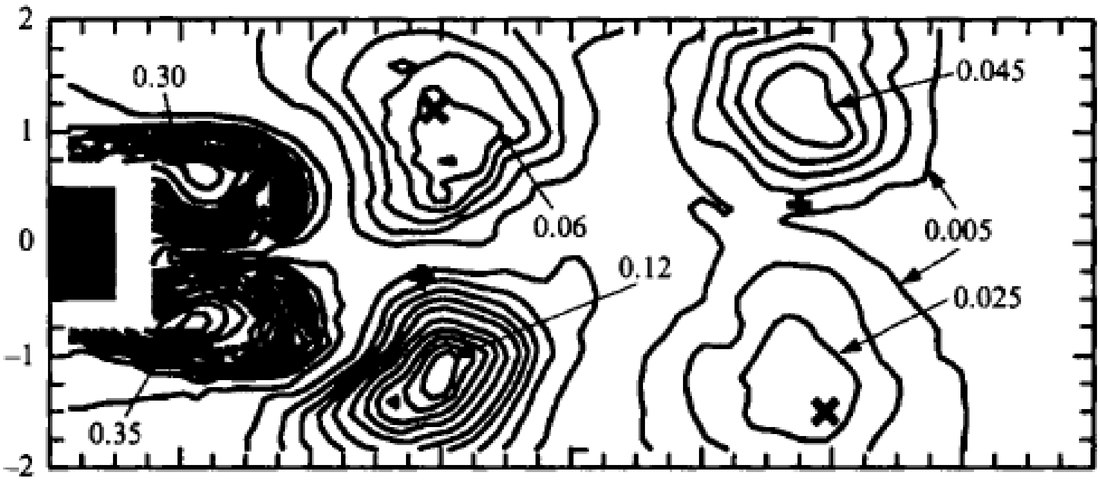

Figure 7.23: Comparison of phase-averaged periodic along wind normal stress, $< \tilde{u}\tilde{u} >$, component

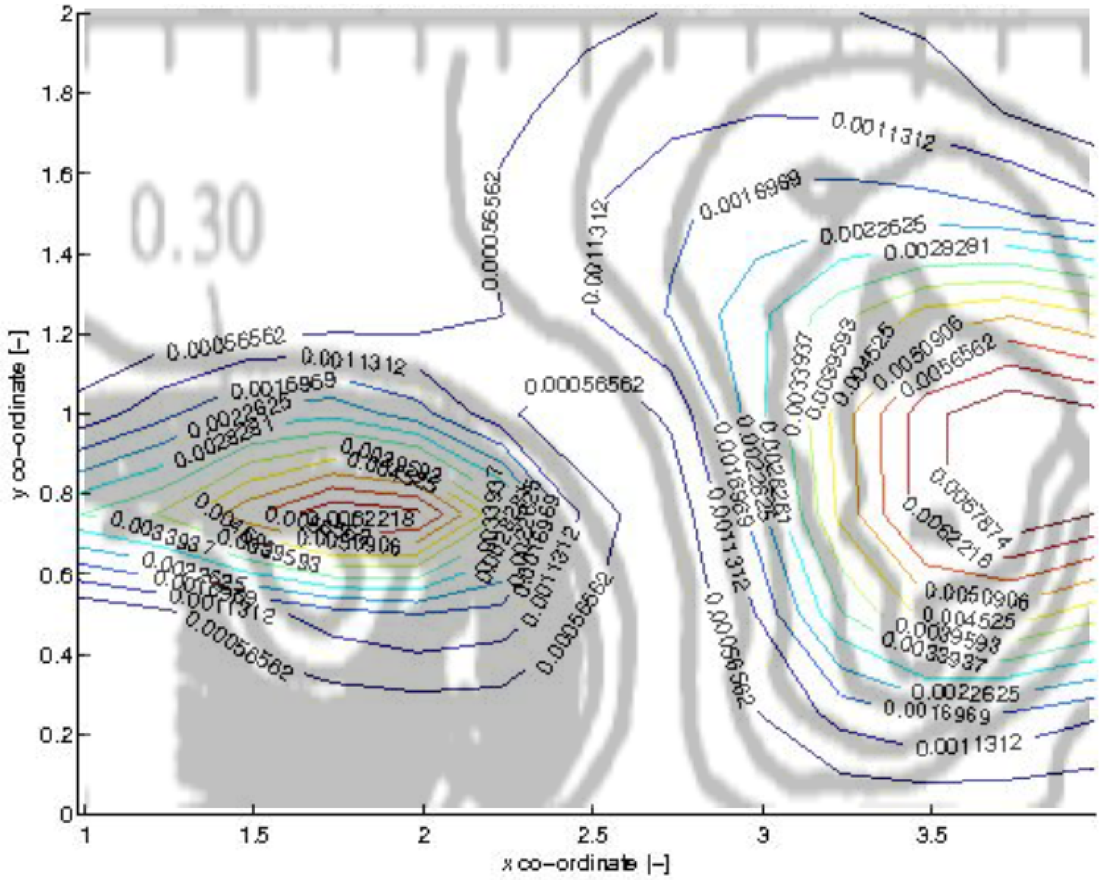

Figure 7.24: Lyn et al. (1995) phase-averaged periodic along wind normal stress, $< \tilde{v}\tilde{v} >$, component

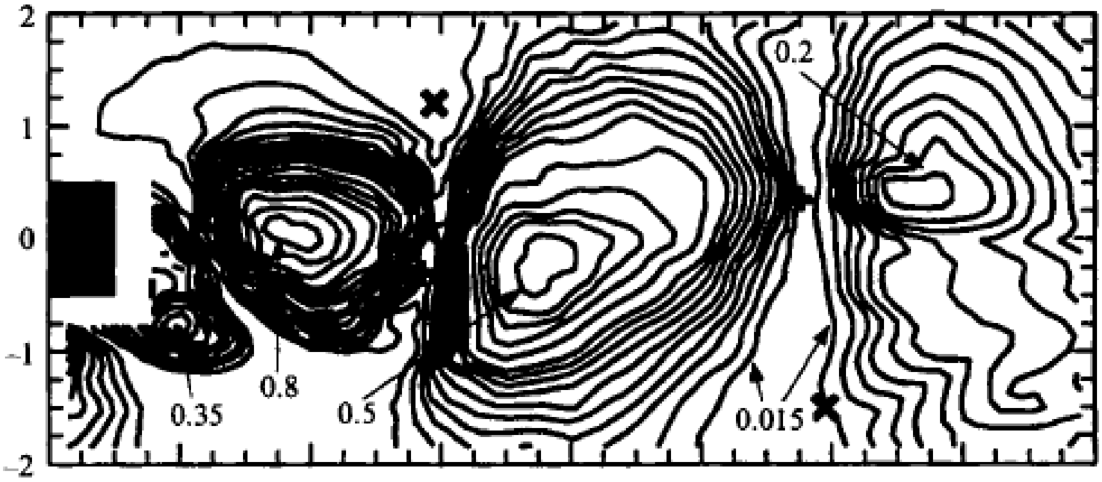

Figure 7.25: Comparison of phase-averaged periodic along wind normal stress, $< \tilde{v}\tilde{v} >$, component

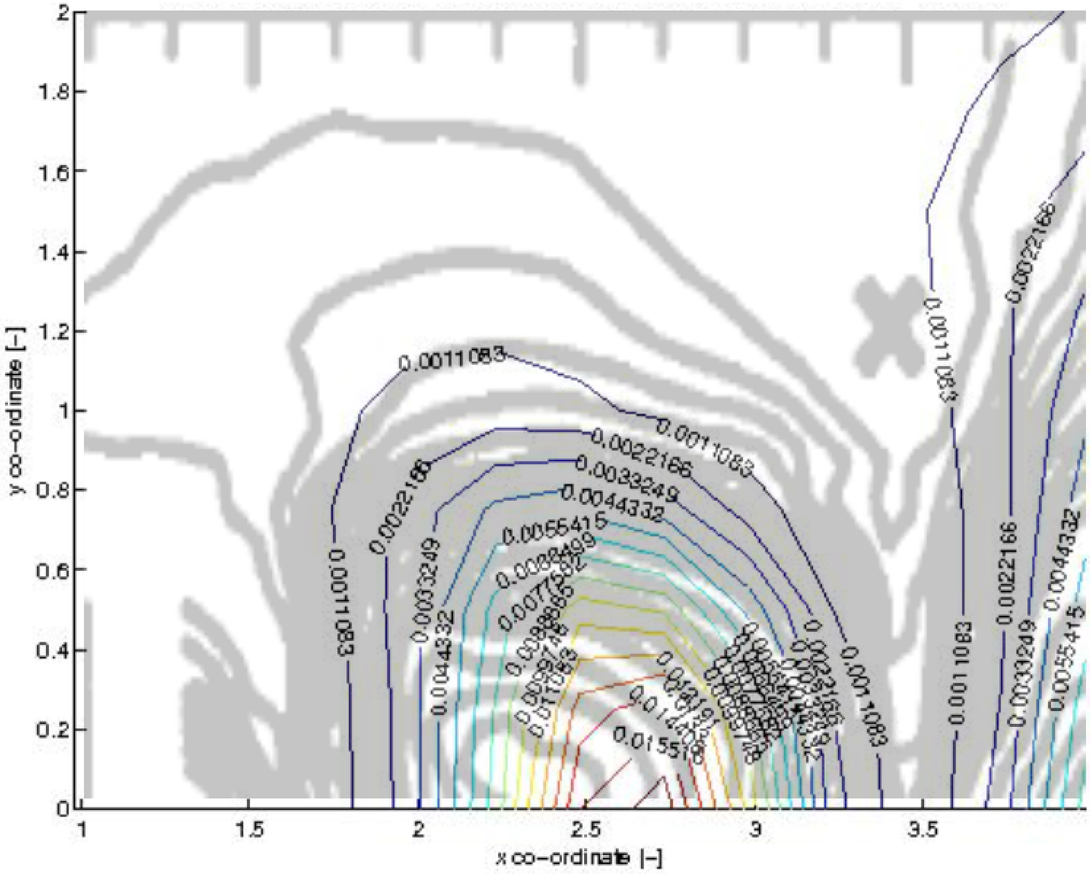

Figure 7.26: Lyn et al. (1995) phase-averaged periodic Reynolds stresses , $< -\tilde{u}\tilde{v} >$

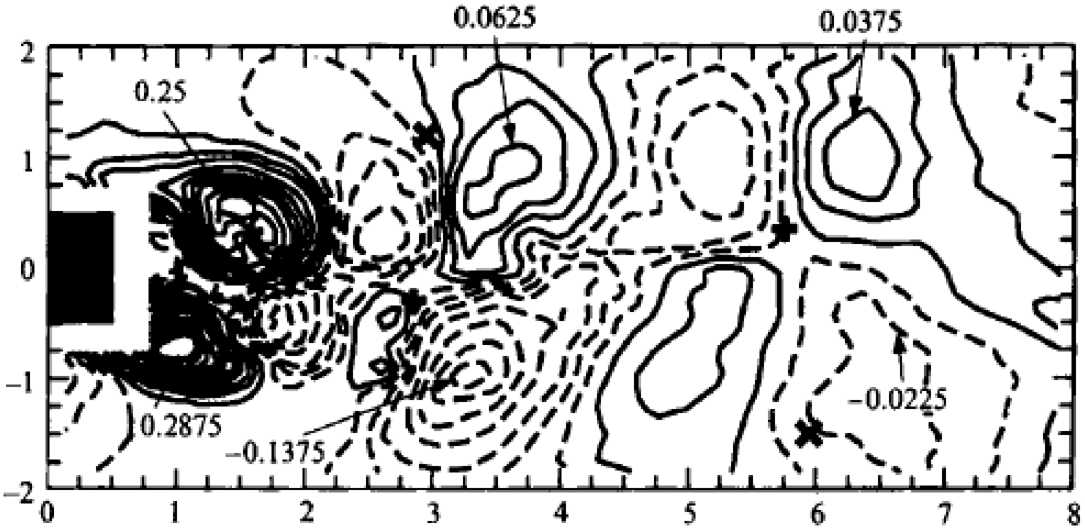

Figure 7.27: Comparison of phase-averaged periodic Reynolds stresses , $< -\tilde{u}\tilde{v} >$

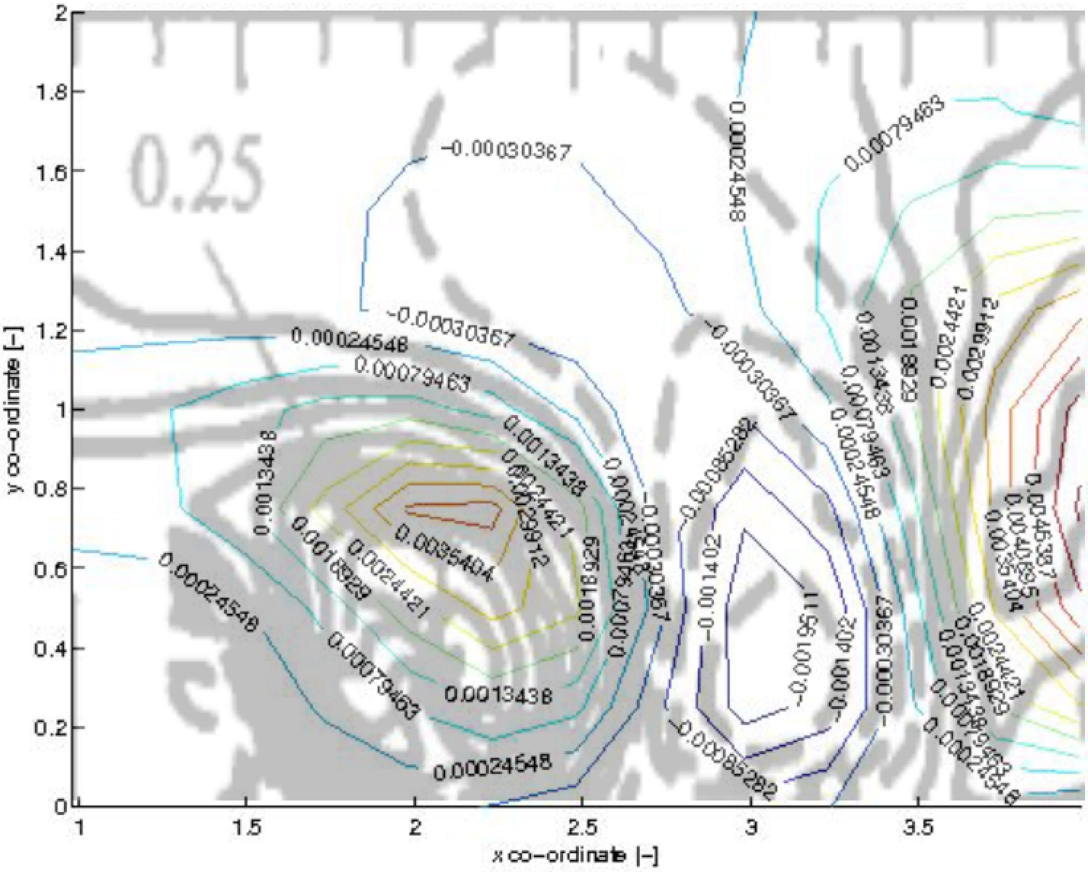

Comparison of Figures 7.26 and 7.27 reveal the phase-averaged periodic Reynolds stresses, $< -\tilde{u}\tilde{v} >$, have a similar pattern to those measured by Lyn et al. (1995). Even though the distribution of the stresses is similar, the magnitude of $< -\tilde{u}\tilde{v} >$ is significantly different that Lyn et al. measured. As indicated in Table 6.7, the results of the simulation compared with the experimental results vary by as much as 50 times.

7.4.4 Fluctuating Normal and Reynolds Stresses

The distribution of phase-averaged fluctuating along wind normal stress component, $< u'u' >$ is not particularly consistent with the field measured by Lyn et al. (1995), which is shown in Figure 7.28. Moreover, there is a significant difference in the magnitude of the normal stresses as shown in Figure 7.29.

There are some similarities between the measurements and the estimated phase-averaged fluctuating across wind normal stress, $< v'v' >$, distribution shown in Figures 7.30 and 7.31. Similarly, the phase-averaged fluctuating Reynolds stresses, $< -u'v' >$, which are predominantly influenced by the cross-stream fluctuations, shows similarities between the measured and simulated data as shown in Figures 7.32 and 7.33. In both cases, the magnitude of the stresses is not exact but is the correct order of magnitude.

Similarly, investigation of the kinetic energy of the turbulent fluctuations would suggest that the simulated kinetic energy flow field roughly approximates the measured filed, shown in Figure 7.34. It is apparent from Figure 7.35 that estimates of the turbulent kinetic energy, although not particularly accurate, are in the correct order of magnitude

Figure 7.28: Lyn et al. (1995) phase-averaged fluctuating along wind normal stress, $< \tilde{u}\tilde{u} >$, component

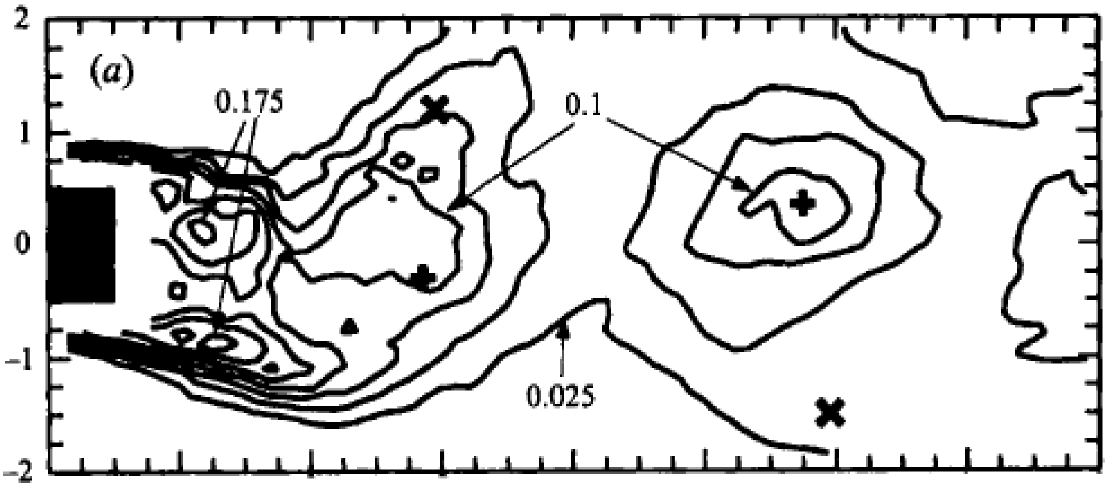

Figure 7.29: Comparison of phase-averaged fluctuating along wind normal stress, $< \tilde{u}\tilde{u} >$, component

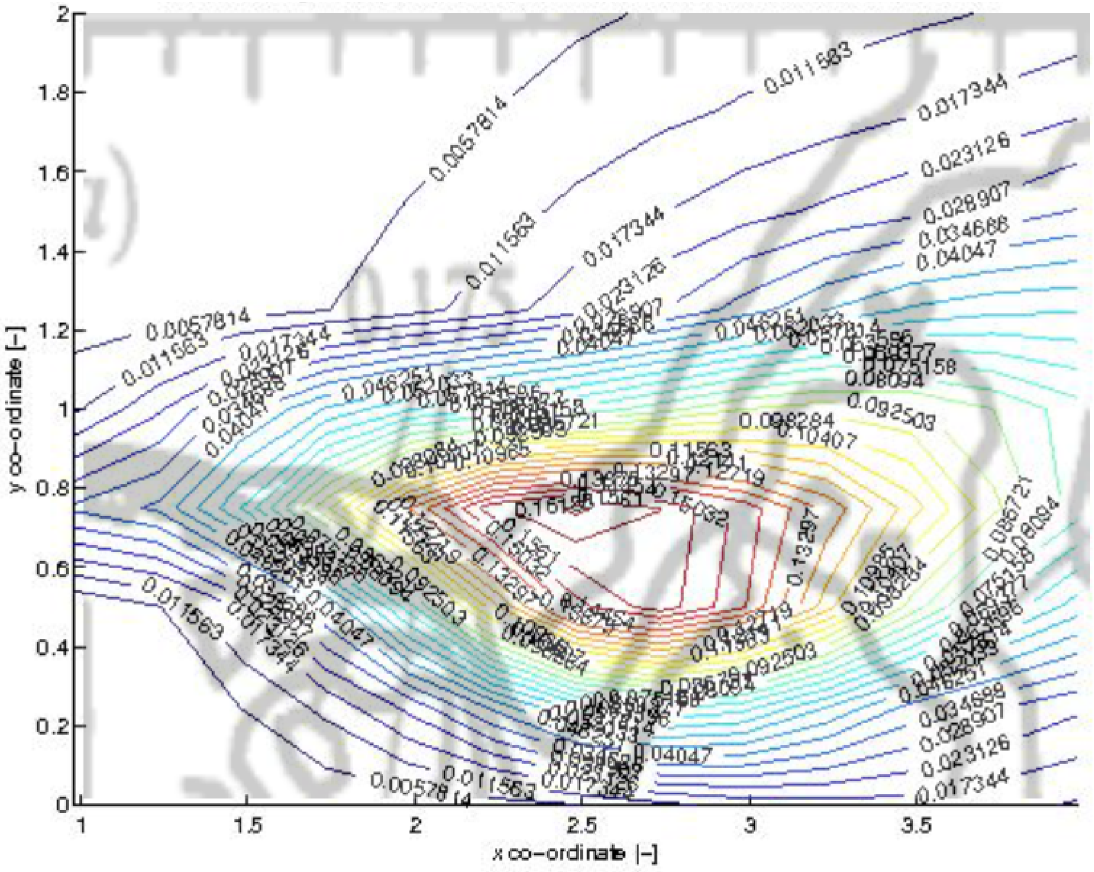

Figure 7.30: Lyn et al. (1995) phase-averaged fluctuating along wind normal stress, $< \tilde{v}\tilde{v} >$, component

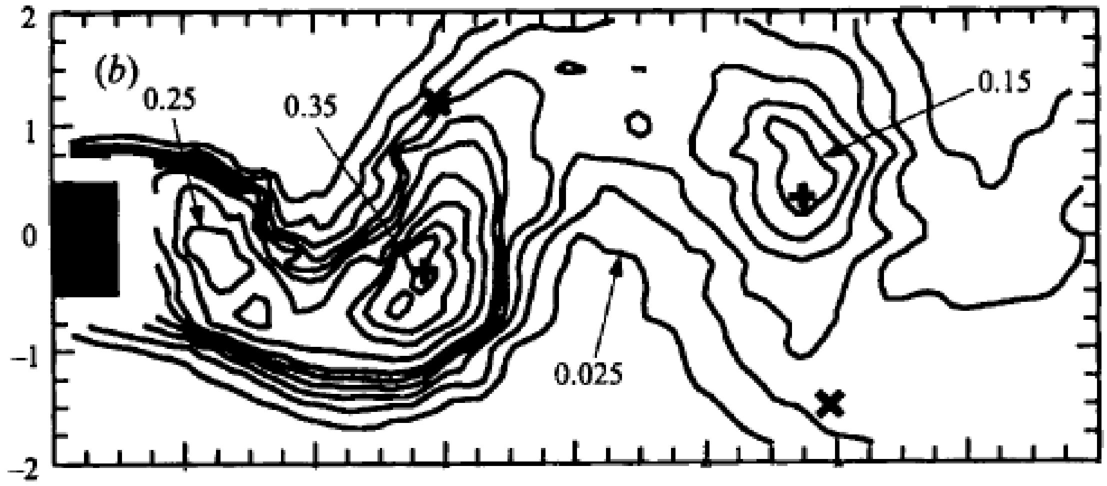

Figure 7.31: Comparison of phase-averaged fluctuating along wind normal stress, $< \tilde{v}\tilde{v} >$, component

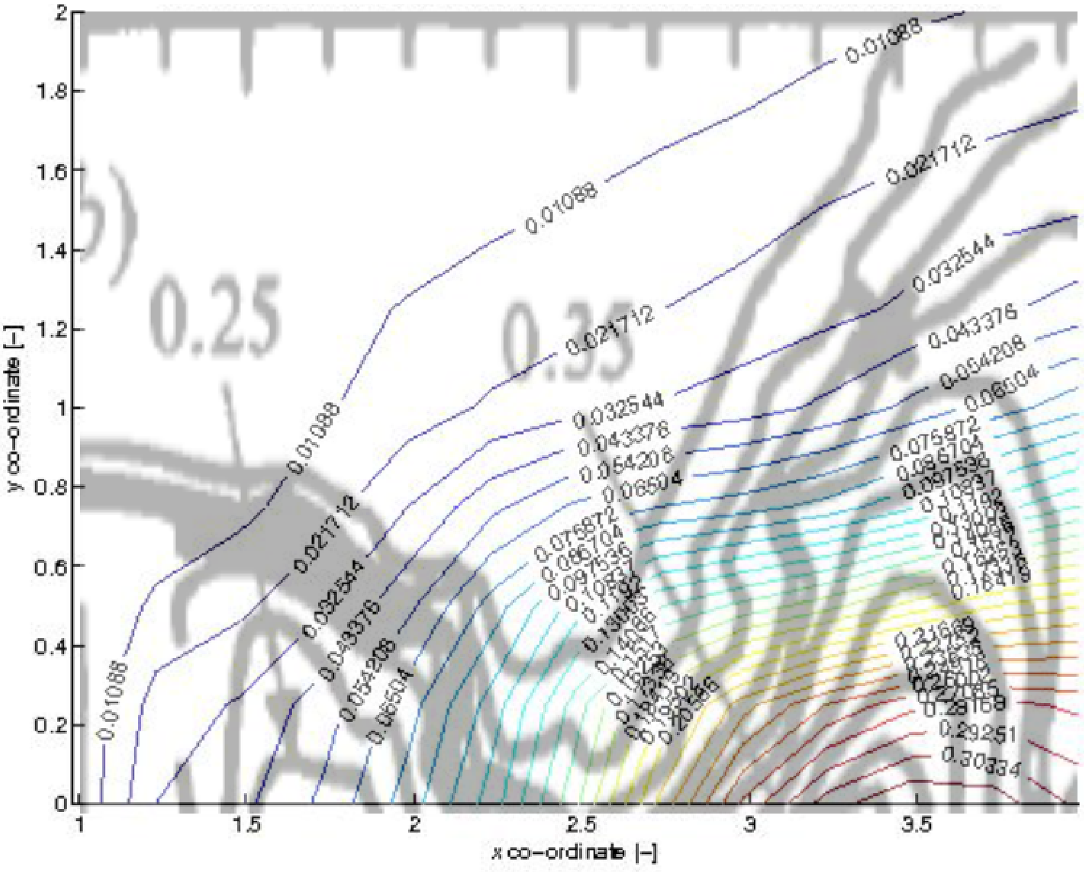

Figure 7.32: Lyn et al. (1995) phase-averaged fluctuating Reynolds stresses , $< -\tilde{u}\tilde{v} >$

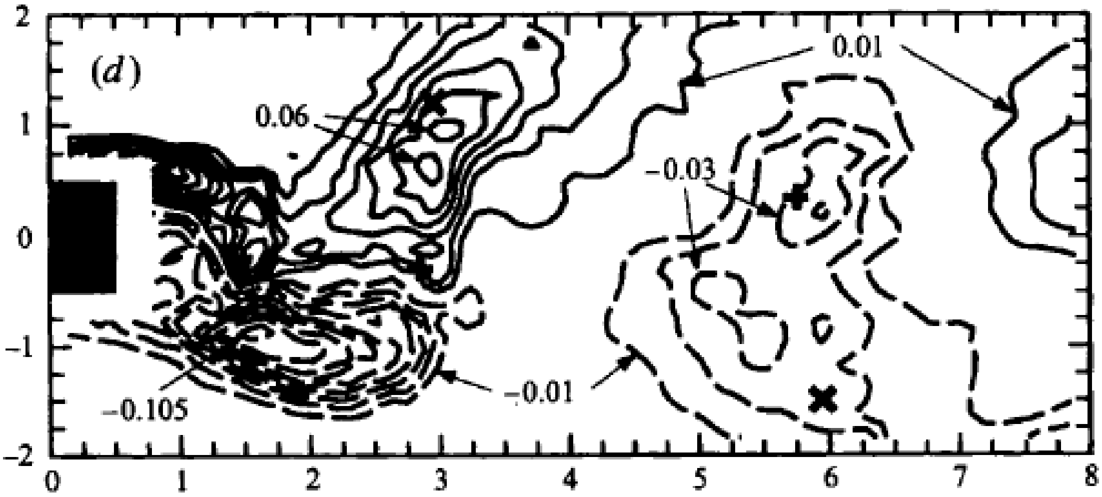

Figure 7.33: Comparison of phase-averaged fluctuating Reynolds stresses , $< -\tilde{u}\tilde{v} >$

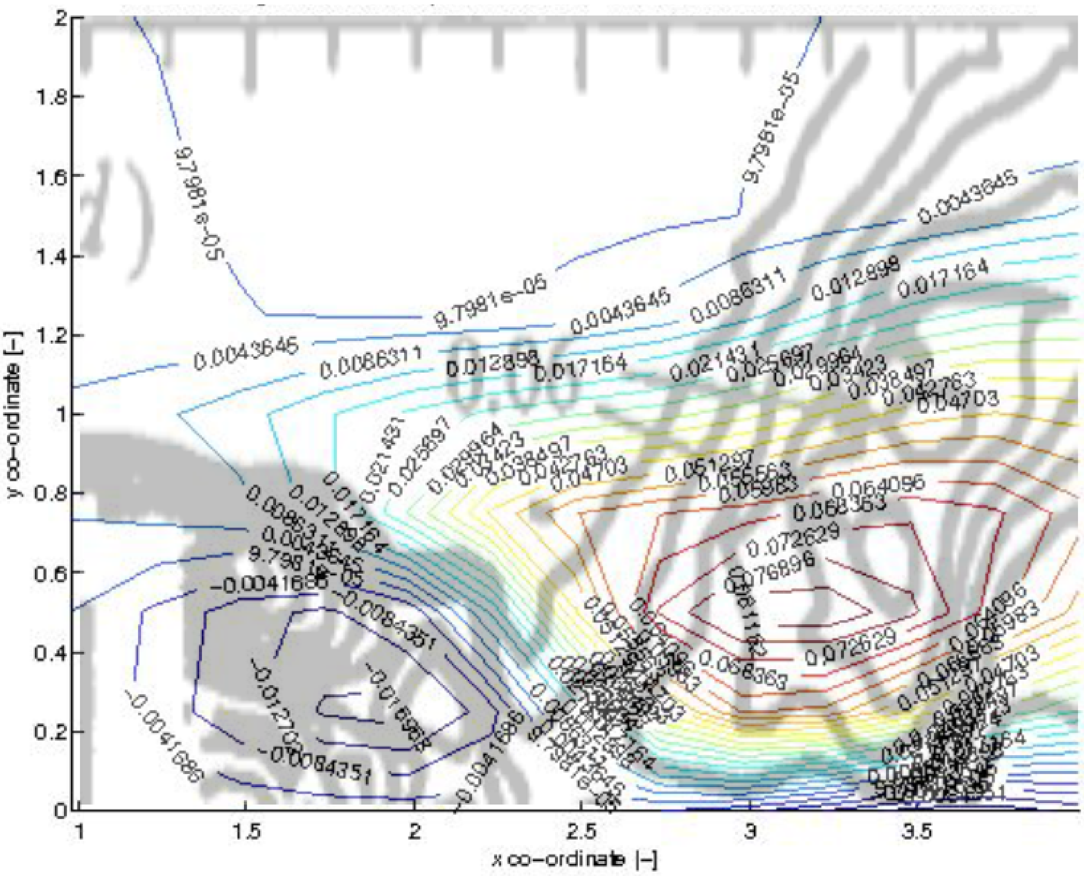

Figure 7.34: Lyn et al. (1995) phase-averaged kinetic energy of turbulent fluctuations, $< k >$

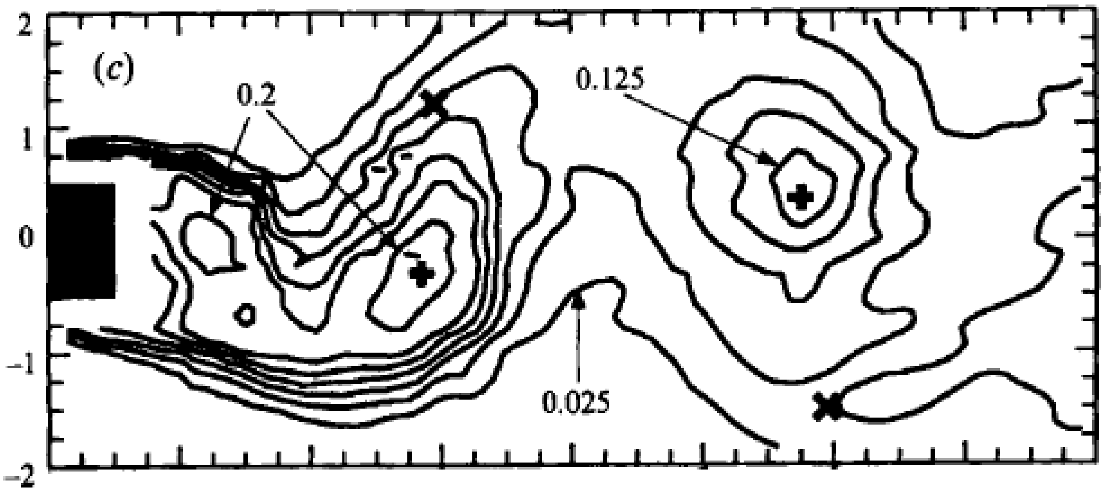

Figure 7.35: Comparison of phase-averaged kinetic energy of turbulent fluctuations, $< k >$

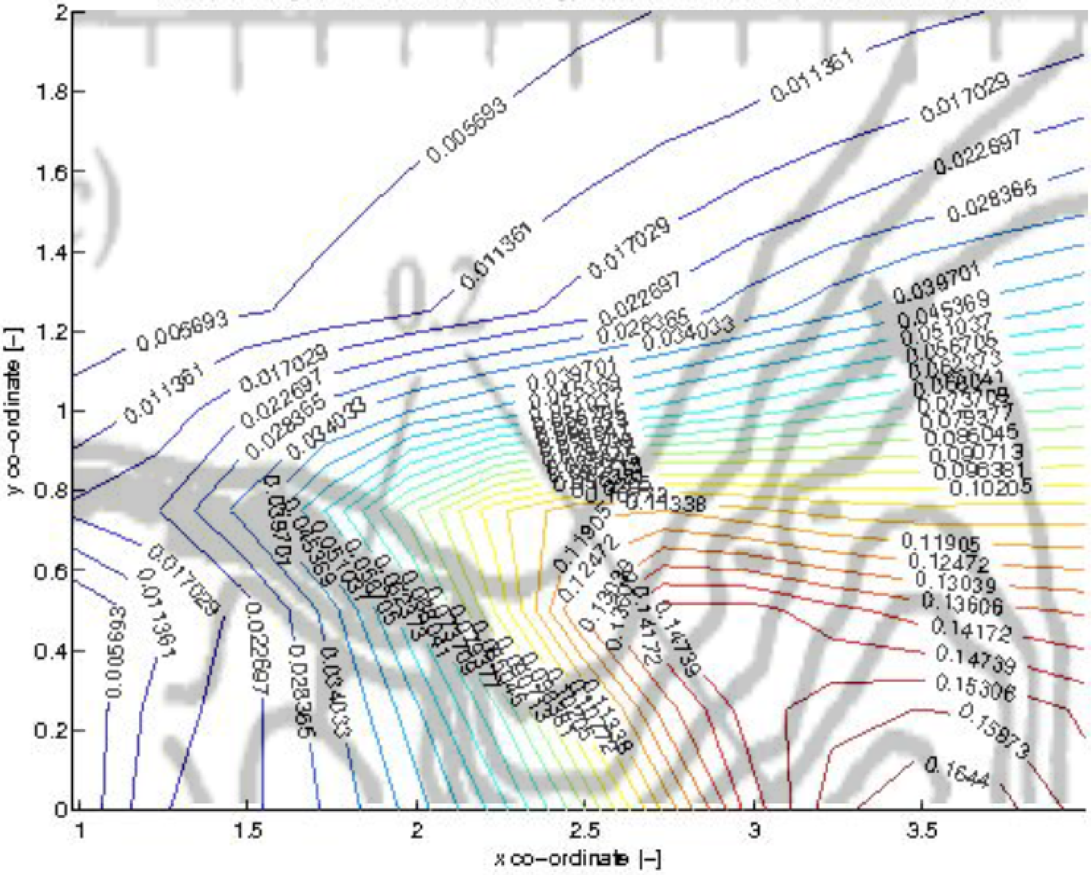

Figure 7.36: Lyn et al. (1995) phase-averaged vorticity, $< \omega >$

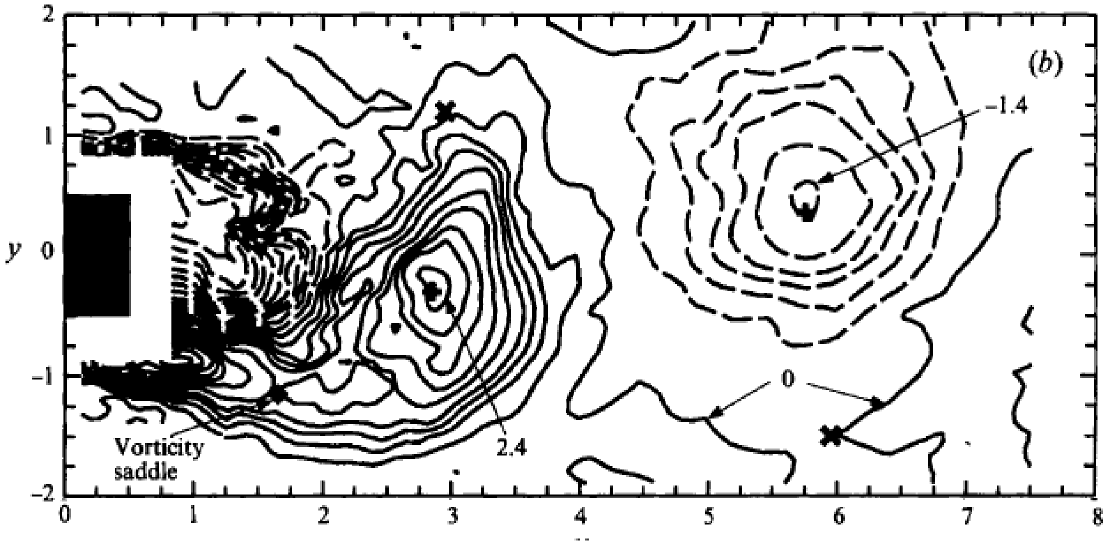

Figure 7.37: Comparison of phase-averaged vorticity, $< \omega >$

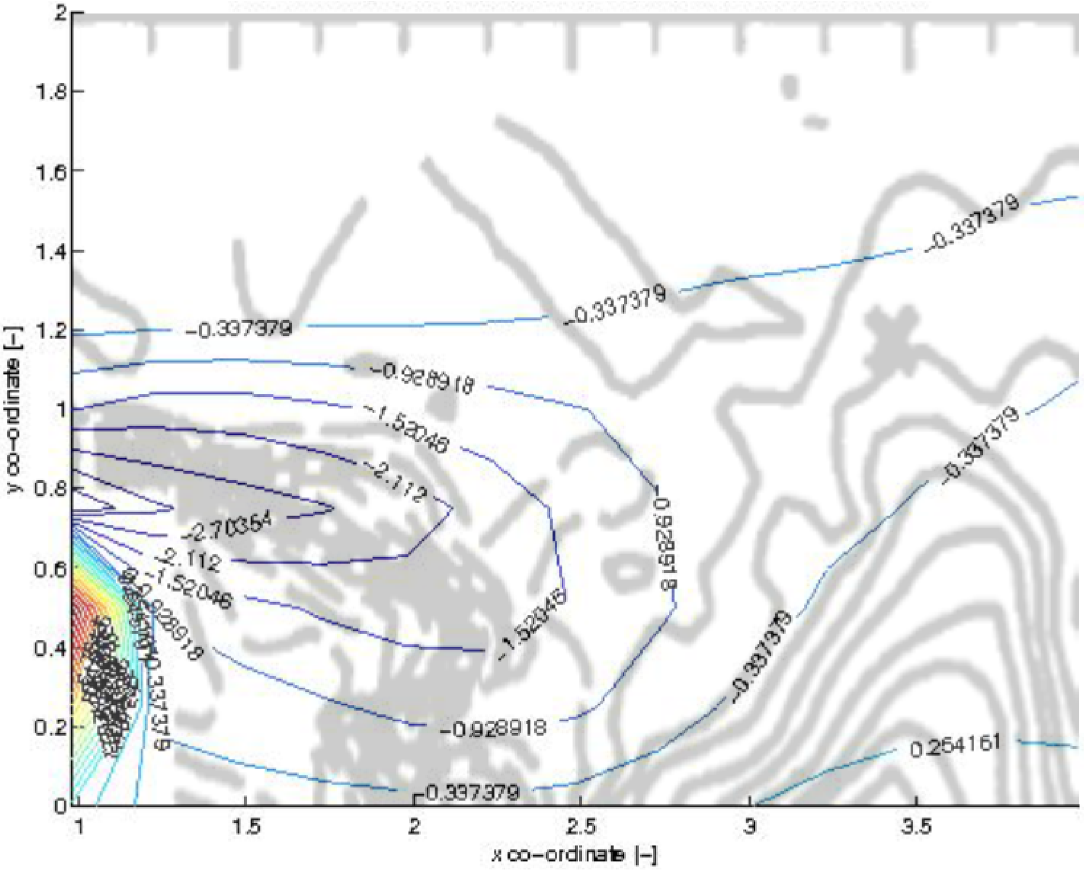

7.4.5 Vorticity

Due to the complexity of the phase-averaged vorticity distribution, it is difficult to determine how accurately the simulation data matches the experimental data. A qualitative interpretation of Figure 7.36 and 7.37 would suggest that although the overall distribution appears similar that there is an order of magnitude difference between the experimental and simulation results.

Table 7.6: Comparison of Phase-averaged Variables with Lyn et al. (1995)

Study			**Present**	**Lyn[1]**
			(-)	(1995)
Periodic	Normal stress along wind	$<\bar{u}\bar{u}>$	0.00622	0.300
	Normal stress cross wind	$<vv>$	0.01552	0.800
	Reynolds stress	$<-\bar{u}v>$	0.00464	0.250
Fluctuating	Normal stress along wind	$<u'u'>$	0.01156	0.175
	Normal stress cross wind	$<v'v'>$	0.30334	0.350
	Reynolds stress	$<-u'v'>$	0.07689	0.060
Turbulent Kinetic Energy		$<k>$	0.16440	0.200
Vorticity		$<w>$	0.25416	2.400

7.5 Discussion

Due to time constraints, the 3D simulation carried out for the validation had not transitioned from a steady state condition to a fully developed transient for the analysis of this simulation to be included in this study. The most refined case completed as part of the verification stage was considered for the purposes of validation instead.

The CWE model using RANS simulation with k-omega turbulence model and wall functions does not accurately predict flow around a square cylinder. The significant errors in the simulation are due in part to use of wall function near solid boundaries and in regions where flow separation occurs. It is necessary to reduce the mesh size near the solid boundaries as well as reduce the time-step proportionately to avoid using wall functions near the surface boundaries.

Previous studies predict a range of values for the Strouhal number, however, the mesh refinement and upstream length were found to have a moderate influence on the result in the verification stage. There must be another parameter not considered in this study that influences the value of the Strouhal number.

The phase-averaged variables may be useful in the validation of CWE simulations. While their distribution of phase-averaged variables might be similar to the experimental data, their values can be quite distinct.

7.5.1 Challenges

One major challenge faced while undertaking this research was to become accustomed with the intricacies of OpenFOAM. OpenFOAM is an open source computational fluid dynamics software package. Outside of the OpenFOAM training seminars held from time to time and the user fora that exist online, there is little or no technical support. Therefore, it can be quite challenging and time-consuming to resolve problems when they do arise.

Another challenge encountered while carrying out this study was using the computational cluster. Originally, OpenFOAM was not installed correctly on the cluster, therefore, the running of simulations was limited to serial running on a personal computer. Following the correct installation of OpenFOAM on the cluster, it was not possible to run OpenFOAM in parallel across multiple nodes for some unexplained reason. This issue was never resolved over the period that the research was conducted. Computations were limited to a single node, which contains 16 processors. This seriously restricted the rate that problems could be solved and the scale of the problems that could be investigated in this study.

Chapter 8

Conclusions & Recommendations

8.1 Conclusions

8.1.1 Verification

1. The analysis of the verification stage results suggests that different levels of refinement are required to produce an accurate pressure flow field than that are required to generate an accurate pressure flow fields.

2. The mesh refinement is the most significant simulation parameter. It influences most of the variables considered in this study and it is the most prominent variable in many cases. The CWE model is considered very sensitive to mesh refinement.

3. The wall function do not hold for flow near solid boundaries and for separated flows, in particular. Wall functions result in a poor approximation and a significant underestimation of the kinetic energy of the turbulent fluctuations.

3. The experimental design approach revealed that the upstream length is important in the determination of both velocity and pressure related variables. Over lengths considered in this study, it appears that the upstream length has a tendency to converge.

4. The downstream and cross-stream lengths do influence some of the simulated variables, however, their influence is minor and show no sign of convergence with refinement.

5. The time-step was not found to have a significant influence on simulation variables. It is believed that the transient PIMPLE solver, which relies

upon under-relaxation to maintain the stability of the algorithm, is responsible for removing the dependence of the CWE model on the time-step.

8.1.2 Validation

1. Due to time constraints, the 3D simulation carried out for the validation had not transitioned from a steady state condition to a fully developed transient for the analysis of this simulation to be included in this study. The most refined case completed as part of the verification stage was considered for the purposes of validation instead.

2. The CWE model using RANS simulation with k-omega turbulence model and wall functions does not accurately predict flow around a square cylinder.

3. The significant errors in the simulation are due in part to use of wall function near solid boundaries and in regions where flow separation occurs.

4. It is necessary to reduce the mesh size near the solid boundaries as well as reduce the time-step proportionately to avoid using wall functions near the surface boundaries.

5. Previous studies predict a range of values for the Strouhal number, however, the mesh refinement and upstream length were found to have a moderate influence on the result in the verification stage. There must be another parameter not considered in this study that influences the value of the Strouhal number.

6. The phase-averaged variables may be useful in the validation of CWE simulations. While their distribution of phase-averaged variables might be similar to the experimental data, their values can be quite distinct.

8.1.3 Overall

1. The verification and validation of CWE simulations to ensure that the results robust and reliable.

2. It is necessary to identify all significant sources of error for effective verification to be undertaken.

3. A sound verification of the CWE model is necessary before a conclusive validation can be conducted.

4. The study is unable to confirm the validity of factorial design approach for the verification and validation of CWE models.

5. The factorial design approach is a simple statistical approach that is easily applied to the evaluation of uncertainty.

6. It is not possible to validate model without proper verification of model first.

8.2 Recommendations for Further Study

1. Re-examine 3D flow around a square cylinder. However, refine the mesh and reduce to time-step to avoid using any wall functions. Undertake a similar study without wall function on the boundary surfaces.

2. Rather than using specifying the mesh refinement in the vicinity of the square cylinder, as a simulation parameter for the experimental design technique, define the mesh size on the boundary surface (y+ <=5) and use a mesh expansion factor as the simulation parameter.

3. Carry out a similar study that considers more complicated cross-sectional geometries such as geometries that are more representative of real structures.

4. Incorporate a dynamic mesh into the CWE model. Using this mesh, investigate free and forced vibration due to fluid structure interaction (FSI).

5. Consider of study that examines fluid structure interaction and in particular, phenomenon such as flow-induced motions (vortex induced motions) and aeroelastic effects (flutter).

6. Undertake a study to compare the response from simulations replicating scale model experiments in a wind tunnel and the full-scale structure in its natural environment.

References

Bearman, P. W., Trueman, D. M., (1972). An investigation of the flow around rectangular cylinders. *Aeronautical Quarterly, 23,* 229-237.

Bearman, P. W., Obasaju, E. D., (1982). An experimental study of pressure fluctuations on fixed and oscillating square-section cylinders. *Journal of Fluid Mechanics, 119,* 297-321.

Box, G. E. P., Hunter, W. G., Hunter, J. S., (1978). *Statistics for experimenters: an introduction to design, data analysis and model building.* New York, NY: John Wiley & Sons.

Dahl, S. M., (2014). Unsteady RANS simulation of flow around rectangular cylinders with different aspect ratios at high Reynolds number (Master Thesis). *Department of Marine Technology, Norwegian University of Science and Technology.*

Durao, D. F. G., Heitor, M. V., Pereira, J. C. F., (1988). Measurements of turbulent and periodic flows around a square cross-section cylinder. *Experiments in Fluids, 6,* 298-304.

Elger, D. F., Williams, B. C., Crowe, C. T., Roberson, J. A., (2013). *Engineering fluid mechanics* (10th ed.). Hoboken, NJ: John Wiley & Sons.

Franke, R., Rodi, W., and Schönung, B., (1990). Numerical calculation of laminar vortex-shedding flow past cylinders. *Journal of Wind Engineering and Industrial Aerodynamics, 35,* 237-257.

Ferziger, J. H., Peric, M., (2002). *Computational Methods for Fluid Dynamics* (3rd ed.). Berlin, Germany: Springer.

Hussain, A. K. M. F., (1983). Coherent structures – reality and myth. *Physics of Fluids, 26,* 2816-2850

Lee, B. E., (1974). The effect of turbulence on the surface pressure field of a square prism. *Journal of Fluid Mechanics, 69(2),* 263-282.

Lee, S., Bienkiewicz, B., (1998). Finite element implementation of large eddy simulation for separated flows. *Journal of Wind Engineering and Industrial Aerodynamics, 77&78,* 603-617.

Lyn, D. A., Rodi, W., (1993). The flapping shear layer formed by flow separation from the forward corner of a square cylinder. *Journal of Fluid Mechanics, 267,* 353-376.

Lyn, D. A., Einav, S., Rodi, W., Park, J. H., (1995). A laser-Doppler velocrimetry study of ensemble-averaged characteristics of the turbulent near wake of a square cylinder. *Journal of Fluid Mechanics, 304,* 285-319.

Oberkampf, W. L., Trucano, T. G., (2002). Verification and validation in computational fluid dynamics. *Progress in Aerospace Sciences, 38,* 209-272.

OpenFOAM guide/The PISO algorithm in OpenFOAM (Sept 7, 2013) Retrieved July 26, 2015 from Unofficial OpenFOAM wiki
Wiki: https://openfoamwiki.net/index.php/OpenFOAM_guide/The_PISO_algorithm_in_OpenFOAM

OpenFOAM guide/The SIMPLE algorithm in OpenFOAM (Nov 12, 2014) Retrieved July 26, 2015 from Unofficial OpenFOAM wiki
Wiki: https://openfoamwiki.net/index.php/OpenFOAM_guide/The_SIMPLE_algorithm_in_OpenFOAM

OpenFOAM guide/The PIMPLE algorithm in OpenFOAM (Nov 8, 2014) Retrieved July 9, 2015 from Unofficial OpenFOAM wiki
Wiki: https://openfoamwiki.net/index.php/OpenFOAM_guide/The_PIMPLE_algorithm_in_OpenFOAM

Roache, P. J., (2009). *Fundamentals of Verifications and Validation.* Socorro, NM: Hermosa Publishers.

Shimada, K., Isihara, T., (2002). Application of a modified k-ε model to the prediction of aerodynamic characteristics of rectangular cross-section cylinders. *Journal of Fluids and Structures, 16(4),* 465-485.

Simiu, E., Scanlan, R. H., (1996). *Wind effects on structures: fundamentals and applications to design* (3rd ed.). New York, NY: John Wiley & Sons, Inc.

Tamura, T. Yoshiyuki, O., (2003). LES analysis on aeroelastic instability of prisms in turbulent flow. *Journal of Wind Engineering and Industrial Aerodynamics, 91,* 1827-1846.

Tian, X., Ong, M. C., Yang, J., Myrhaug, D., (2012). Unsteady RANS simulations of flow around rectangular cylinders with different aspect ratios. *Ocean Engineering, 53,* 208-216.

Wilcox, D. C., (1998). *Turbulence modeling for CFD* (2nd ed.). La Canada, CA: DCW Industries, Inc.

Xu, Y. L., (2013). *Wind effects on cable-supported bridges*. Singapore: John Wiley & Sons.

Yeo, D., (2013). *Semi-annual technical report, estimating the sensitivity of computational fluid dynamics simulations to changes in simulation parameters: an experimental design technique.* Gaithersburg, MD: National Institute of Standards and Technology (NIST).

Curriculum Vitae

Surname: Mac Réamoinn **First Name:** Réamonn **Middle Name:** Pådhraic

Date of Birth: 22nd March 1983

Nationality: Irish

Education:

2013 – 2015	Masters Degree (M.S.E.) in Civil Engineering Johns Hopkins University, Baltimore, Maryland, U.S.A.
2001 – 2005	Bachelors Degree (B.A. B.A.I.) in Civil, Structural and Environmental Engineering University of Dublin, Trinity College, College Green, Dublin 2, Ireland.

Research:

Thesis	A validation and verification approach for computational wind engineering simulations using an experimental design technique